

Numerical simulation of collapse induced shock dynamics for the prediction of the geometry, pressure and temperature impact on the cavitation erosion in micro channels

Romuald Skoda*, Uwe Iben

Robert Bosch GmbH, Corporate Research and Advance Engineering - CR/ARH,
Postfach 106050, D-70049 Stuttgart, Germany

Alexander Morozov

AVL List GmbH, Hans-List Platz 1, A-8020 Graz, Austria

Michael Mihatsch, Steffen J. Schmidt, Nikolaus A. Adams

Institute of Aerodynamics and Fluid Mechanics, Technische Universität München,
Boltzmannstr. 15, D-85748 Garching, Germany

* Romuald.Skoda@de.Bosch.com

ABSTRACT

A compressible 2D Euler CFD code is utilised for the numerical simulation of compressible cavitating liquids with a density-based numerical scheme which has been proved to capture shock-induced dynamics that are the origin of erosion damages [22]. A barotropic cavitation model is applied on planar micro throttles where the qualitative impact of the following parameters on the location and strength of erosion is evaluated and compared to experimental data:

- Channel inlet geometry, round versus sharp inlet shape
- Channel inlet and outlet pressure
- Fluid inlet temperature

While the erosion strength and location in the experiment is evaluated by temporal sequences of the material erosion, an erosion probability based on pressure thresholds is extracted from the simulation results which quantifies the magnitude of the stress on the wall.

By comparing the wall stress magnitude (simulation) and the material erosion (experiment), the qualitative influence of the channel inlet geometry as well as the inlet and outlet pressure can be well captured. The temperature impact on erosion can not be predicted by the barotropic model.

NOMENCLATURE

SYMBOLS

c	= Speed of sound	[m·s ⁻¹]
L_{cell}	= Cell size	[m]
L_{wave}	= Wave length	[m]
L_{wake}	= Length of the outlet domain	[m]
N	= Number	[-]
p	= Pressure	[Pa]
p_{vap}	= Vapour pressure	[Pa]
P_P	= Erosion probability by pressure erosion indicator	[-]
P_F	= Erosion probability by force erosion indicator	[-]

s	= Entropy	[J·kg ⁻¹ ·K ⁻¹]
t	= Time	[s]
T	= Temperature	[°C], [K]
u	= Velocity	[m·s ⁻¹]
dt	= Time step	[s]
Δt	= Time interval	[s]
α	= Vapour volume fraction	[-]
ρ	= Density	[kg·m ⁻³]
τ	= Oscillation period	[s]

ABBREVIATIONS AND NAMES

<i>CATUM</i>	= Cavitation TU München
<i>CFD</i>	= Computational fluid dynamics
<i>CCL</i>	= time-averaged cavitation cloud collapse location
<i>CFL</i>	= Courant- Friedrichs-Lewy
<i>EOS</i>	= Equation of state
<i>EU</i>	= European union
<i>I</i>	= Sharp channel inlet geometry
<i>K</i>	= Round channel inlet geometry
<i>L</i>	= Left
<i>MINMOD</i>	= Limiter by Harten [5]
<i>NS2D</i>	= Two-dimensional Navier-Stokes solver
<i>OP</i>	= Operation point
<i>PREVERO</i>	= Experimental and CFD technology for preventive reduction of diesel engine emission caused by cavitation erosion
<i>R</i>	= Right
<i>SMART</i>	= Sharp and Monotonic Algorithm for Realistic Transport [7]
<i>THR</i>	= Threshold
<i>UDS</i>	= Upwind differencing scheme i.e. no reconstruction
<i>WSM</i>	= Wall stress magnitude; identical to P_P or P_F

SUBSCRIPTS

0	= Initial
end	= End of run time
$face$	= Cell face
in	= Inlet
$initial$	= Initial conditions
out	= Outlet
pix	= Image pixel
sim	= Simulation
t	= Total

1. INTRODUCTION

Cavitation erosion has a significant impact on the reliability and durability of injection system components. Due to increasing pressures and faster energizing times erosion frequently causes early fatigue of injector components as valves and injection nozzles. On the other hand, cavitation enhances the spray formation and is therefore a desired phenomenon.

This dualism between desired and threatening features of cavitation makes the design of injection systems increasingly complex. For a thorough understanding of the flow mechanisms an insight into the flow details is indispensable and can only be obtained by high-resolving CFD methods which are utilised for the injection system design in combination with the experimental methods.

The industrial standard CFD methods are based on a simplified Rayleigh equation that originates from the dynamics of a single vapour bubble [13]. Since technical flows are far more complex than single-bubble dynamics the resulting model can be considered as a source-/sink term in the vapour mass equation that has a couple of tuning parameters and relies on the time-averaged consideration of cavitation. Rayleigh models have widely been used mostly in combination with pressure-based and occasionally density-based codes with an implementation that is incompressible in the sense of wave dynamics [14]. A compressible¹ implementation is not available to the knowledge of the authors.

In spite of the physical shortcomings of the Rayleigh models they have been successfully applied to the prediction of integral flow features as the mass flow through simplified injection nozzles [26] or the performance curve decrease of pumps [2], [3], [4], after a careful and time-consuming parameter calibration. However, Rayleigh models are not suitable for the prediction² of cavitation erosion [6]. This is mainly due to the dominating role that compressibility plays in the physics of cavitation erosion. The natural choice is to capture compressible wave dynamics by density-based codes [1], [9]. The solver CATUM [22] has been applied for the representation of shock-induced dynamics on principle test cases, on simple flow obstacles and on a hydrofoil [17], [21]. In particular, the suitability of the code to capture the erosion-determining flow features has been demonstrated [19]. Also an injection nozzle model has been considered [15], [16] with regard to wave dynamics. However, a comparison of the nozzle results with reference data has not been possible due to the lack of detailed experimental data.

Our intention is to evaluate the performance of the CATUM numerics on test cases representative for injection system components by a thorough comparison with experimental data with the focus on cavitation erosion. While the present paper has an application character, there are two companion papers that focus rather on the simulation method basics [12], [20] and one on experiments [11].

¹ The term ‘compressible’ does not only mean a variable density but also a hyperbolic character of the governing equations which is the precondition to capture wave dynamic effects.

² We associate “prediction” with the omission of model tuning parameters

Firstly, we describe the physical models, i.e. the cavitation and fluid model. Afterwards, we give a brief overview over the CATUM numerics. Since injection systems are characterized by micro-scale geometries, micro channels with different inlet shape – a sharp versus a rounded inlet – serve as a simplified representation of injection geometry samples. The experimental reference data on these planar and optically assessable test micro channels are described together with the experimental procedure. Besides the inlet geometry the inlet and outlet pressure as well as the fluid temperature is varied in the experiments and accordingly in the simulations. The comparison of the experimental erosion results with the numerical simulation results is based on the wall stress magnitude (WSM) induced by vapour cloud collapses in the simulations. The WSM is equivalent to a probability of erosion P which is described in the simulation section of this paper. At the end, we draw our conclusions of our results and suggest the further procedure.

2. PHYSICAL MODEL

Since compressible wave dynamics causing erosion is inertia-driven we neglect viscous effects and consider the compressible Euler equations for mass and momentum. Despite the fact that cavitation is inherently three-dimensional we consider a two-dimensional flow for simplicity. A further simplification is the neglect of the energy equation which results in the assumption of isentropic flow, and we assume that no solved air is present in the fluid. As a consequence, we obtain an isentropic equilibrium model which is equivalent to the assumption that vaporization and condensation occur infinitely fast. The simplifications are justified since in the present investigation we are interested in the principle ability of our procedure to capture erosion and on the qualitative impact of test case parameters on the WSM.

We consider a homogenous model so that we describe the two-phase flow by a homogenous mixture of liquid and vapour within each computational cell.

For the experimental as well as numerical investigations we utilize a Diesel-like test fuel. The liquid properties as well as the vapour pressure have been determined by measured data and can not be published here for confidentiality reasons. Nevertheless, it is sufficient to describe the principle features of the property function here for the assessment of the numerical results.

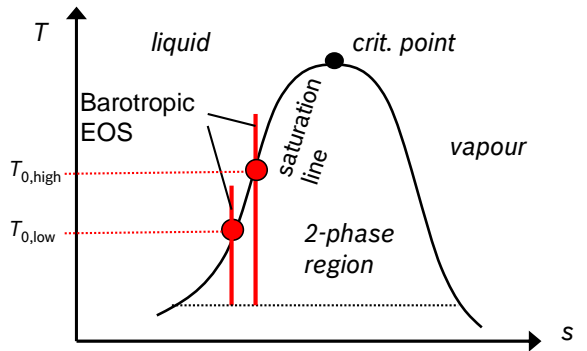


Fig. 1: Illustration of the barotropic EOS

The cavitation model enters the governing equations via the equation of state (EOS) which is constructed in the temperature-entropy diagram assuming thermodynamic equilibrium and an isentropic flow path commonly referred to as barotropic model [8]. The procedure is illustrated by a principle sketch of the temperature-entropy diagram in Fig. 1. By specifying the initial temperature T_0 we define the entropy for the barotropic law. In principle, by means of this procedure we can characterize fluids with different temperatures by their different entropies.

3. NUMERICAL METHOD

In order to prove a code-independent implementation of the numerical scheme we utilise the solver NS2D [2], [23], [24], [25] which has been developed at the Institute of Fluid Mechanics at Munich University of Technology as a code for turbomachinery applications. Originally the code contains a compressible pressure-based scheme with several turbulence models and a Rayleigh cavitation model. We have adopted the numerical scheme from the code CATUM whose numerical properties are described in detail in [18] and are briefly summarized here.

Within an explicit Runge-Kutta time integration and a finite volume discretisation the kernel of the scheme is a Low-Mach number consistent Godunov-type flux formulation which has been developed especially for cavitating flows.

$$\bar{F}_{num} = \rho_{L/R} \cdot u_{face} \cdot \begin{pmatrix} 1 \\ u_{L/R} \\ v_{L/R} \end{pmatrix} + \frac{1}{2} \cdot \begin{pmatrix} 0 \\ p_L + p_R \\ 0 \end{pmatrix} \quad (1)$$

$$u_{face} = \frac{1}{\rho_L + \rho_R} \cdot \left(\rho_L \cdot u_L + \rho_R \cdot u_R + \frac{p_L - p_R}{c_{face}} \right) \quad (2)$$

$$c_{face} = \max(c_L, c_R) \quad (3)$$

The left (L) or right (R) state are determined by the up-wind direction dependent on the sign of u_{face} . We reconstruct the L or R state of the velocity with the SMART scheme [5] and the state of the density with the MINMOD scheme [7]. Since the numerical pressure flux is approximated by a second order central-like interpolation no reconstruction is applied for the pressure. For all calculation results presented, we utilise a CFL number of one.

For the present numerical investigations, we use a reflecting static pressure Dirichlet condition at the outlet by specifying the static pressure by a constant value. Although we are aware of the undesired reflecting properties of this condition we retain it since we have found that it is difficult to maintain a prescribed pressure level by using a non-reflecting condition [21], and the exact outlet pressure level is extremely important in our present investigation. The boundary condition at the inlet corresponds to a transient calculation of the velocity from a prescribed constant total pressure and the static pressure from the inlet adjacent cell at the beginning of each time step.

The verification of the implementation of the flux functions in NS2D is documented in the appendix.

4. EXPERIMENTAL EROSION DATA

For the investigation of cavitation erosion planar throttle geometries (also referred to channel geometries) are utilised that are assessable by optical measurement techniques. In order to accelerate the material erosion, the planar channel samples are manufactured by aluminium.

Two different inlet geometries are used (Sharp inlet = channel I and Round inlet = channel K) and depicted in Fig. 2. This nomenclature stems from historical data processing reasons since the corresponding data processing busses have been called I and K.

The samples are fixed within two sapphire windows to enable optical measurements. The experimental set-up is illustrated in Fig. 3, and details are given in [10] as well as in the companion paper [11].

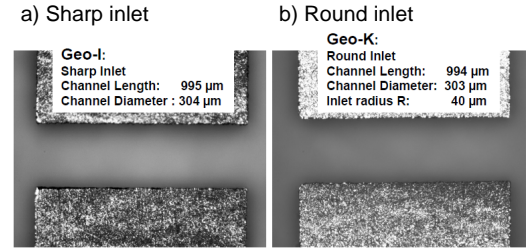


Fig. 2: Planar channel test plates. a) sharp and b) round inlet geometry.

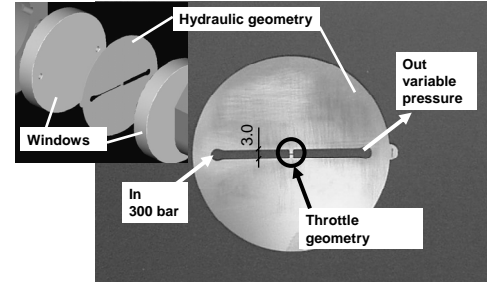


Fig. 3: Experimental set-up

Tab. 1: Operation conditions

OP	Origin	Geometry	p_{in} [bar]	p_{out} [bar]	T_{in} [°C]
1.	PREVERO-1	I (sharp)	301	126	53
2.	PREVERO-1	K (round)	300	117	55
3.	PREVERO-1	K (round)	300	53	53
4.	PREVERO-1	I (sharp)	303	121	29
5.	PREVERO-1	K (round)	301	116	30
6.	PREVERO-2	I (sharp)	200	75	60
7.	PREVERO-2	I (sharp)	300	125	60
8.	PREVERO-2	I (sharp)	400	175	60

We consider two measurement series that have been performed at different times on different test rigs: the first one has emerged from the PREVERO project that has been an EU-

funded research project in the time period of 2003 until 2005 with a strong focus on measurement techniques in micro geometries. Within this first data set called PREVERO-1, the inlet pressure has been kept fix and the outlet pressure is varied systematically. These operating conditions (OP) 1 – 5 are documented in Tab. 1.

The second measurement series called PREVERO-2 has emerged from recent measurements in the Bosch laboratory and is specified by the operation points 6 – 8 in Tab. 1. The inlet pressure has been varied with adjusted outlet pressure. The main difference to the PREVERO-1 series is the usage of a different test rig, a Diesel-like test fluid whose properties are specified in a more narrow way than standard Diesel and a slightly higher fluid temperature. Due to these differences we do not expect exactly the same results comparing OP 1 and 7.

One of the most illustrating results is the cavitation probability which has been evaluated by the average of about one hundred single-shot depth-integrated transmission light images, see Fig. 4. For the PREVERO-2 series and for all OPs but OP 3 of the PREVERO-1 series, the outlet pressure is chosen in a way that the time-averaged vapour cloud collapse location (CCL) indicated by a strong decrease of the cavitation probability is located at about 80 % of the channel length. For the OP 3 a rather low outlet pressure is used to provoke a collapse in the wake downstream of the channel and not within the channel.

In fact, inspecting the same OP 1 and 7 for the I channel for $p_{in} = 300$ bar, $p_{out} \approx 125$ bar and $T_{in} \approx 60^\circ\text{C}$ - compare Fig. 4 b and d - we observe significant differences: for the PREVERO-2 test series the CCL is located further downstream and the lateral vapour extend is more narrow than for PREVERO-1.

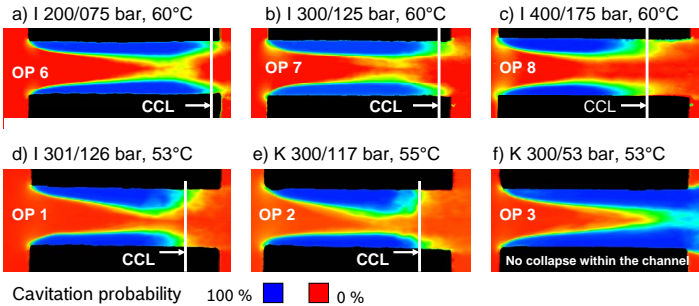


Fig. 4: Cavitation probability (depth-integrated) evaluated from transmission light measurement data of the (a-c) PREVERO-2 and the (d-f) PREVERO-1 test series, indicating the CCL.

Image sequences indicating the erosion progress have been recorded and are shown in Fig. 5 for the PREVERO-2 series and in Fig. 6 for the PREVERO-1 series. Studying the PREVERO-2 results, obviously, the starting erosion location in the channel is associated to the CCL. In particular, for the higher pressure OP 8 the first damage is observed further upstream than for the middle pressure level OP 7. This corresponds to the CCL (Fig. 4 b and c). For the low pressure OP 6, no damage is observed within the analysis time of 180 min.

An overall statement on the PREVERO-2 results is that the inlet and outlet pressure level is a measure for the erosion strength and the outlet pressure serves primarily for adjusting the CCL within the channel.

Regarding the high-temperature PREVERO-1 cases (OP 1–3, Fig. 6), for the low outlet pressure case OP 3 the material erosion is rather moderate and located at the very end of the channel, because no cloud-collapse occurs within the channel which makes cavitation less aggressive. For the higher outlet pressures OP 1 and 2, strong material erosion can be observed within the channel. The channel K shows a faster erosion progress than channel I once erosion has started.

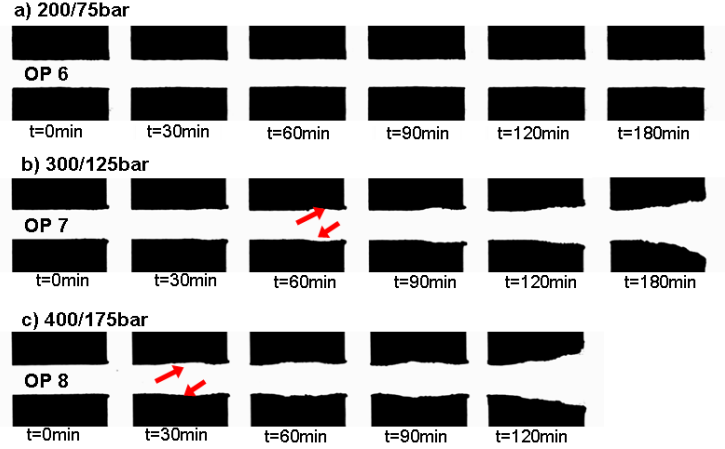


Fig. 5: Sequences of erosion images of the PREVERO-2 test series. The location where erosion is firstly detected by careful inspection of the images is marked by arrows.

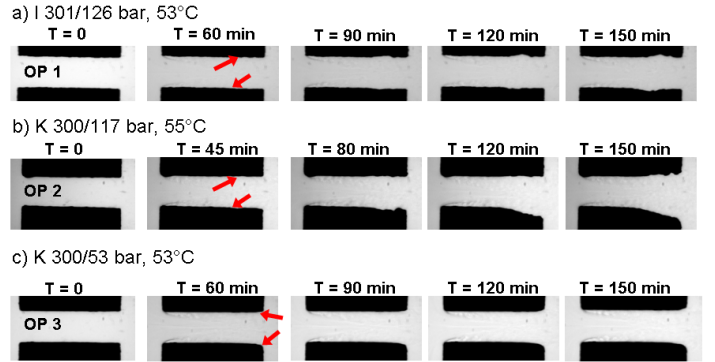


Fig. 6: Sequences of erosion images of the PREVERO-1 test series for cold conditions $T_{in} \approx 55^\circ\text{C}$. The location where erosion is firstly detected by careful inspection of the images is marked by arrows.

In order to quantify the erosion progress the image series of the PREVERO-1 cases have been processed by reference to the original geometry image by counting the pixels that have been removed by material erosion. As a result, the number of pixels N_{pix} corresponding to the erosion progress is shown in Fig. 7 as a function of time. For the cold fuel erosion processes much slower than for hot fuel. Regarding OP 1 and 2 (hot conditions and high outlet pressures), up to about 45 min no difference is discernible for channel I and K. For later instances we do not consider the difference between OP 1 and 2 because we have found that the faster erosion of the K geometry at later instances is dependent on the experimental conditions and cannot be reproduced.

For the PREVERO-1 measurement series also mass flow measurement data is available that is presented in the next section together with the simulation results.

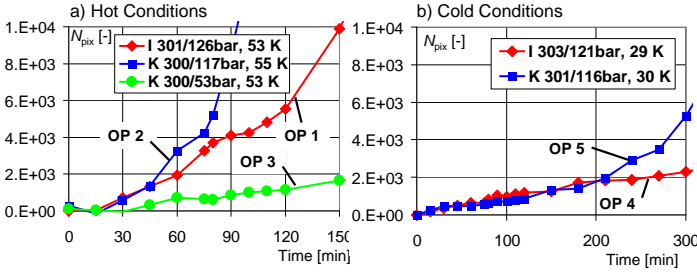


Fig. 7: Number of pixels N_{pix} indicating the erosion progress of the PREVERO-1 cases for a) hot and b) cold conditions

5. SIMULATION

Setup

A 2D setup is chosen to study the effect of the inlet geometry, the inlet and outlet pressure as well as the inlet fluid temperature on erosion, according to the OPs in Tab. 1. Only half the domain is considered by specifying a symmetry condition (which is identical to a slip wall) in the middle of the channel. The average size of the approximately quadratic cells within the channel is about $L_{\text{cell}} = 5 \mu\text{m}$. The computational boundary conditions correspond to the experimental setup of the cases documented in Tab. 1, i.e. for the simulations a total pressure condition $p_{\text{t,in}} = 200, 300$ or 400 bar is specified at the inlet which is very close to the static inlet pressure p_{in} due to the low inlet velocity. In Fig. 9, the computational domain and the grid are depicted for channel K.

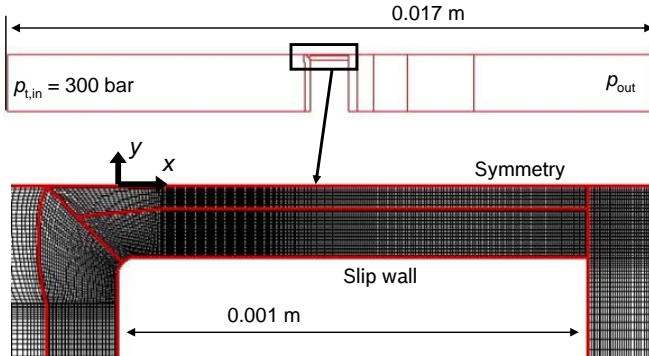


Fig. 8: Computational grid for channel K

We utilise barotropic tables to characterise the “cold” and “hot” experimental conditions by the corresponding entropy where we use $T_{\text{inlet,sim}} = 60^\circ\text{C}$ for all the hot and $T_{\text{inlet,sim}} = 30^\circ\text{C}$ for all the cold conditions. Each simulation was run from scratch with initial conditions:

$$u_{\text{initial}} = 0 \quad (4)$$

$$p_{\text{initial}} = p_{\text{out}} \quad (5)$$

and a total physical run time of $t_{\text{end}} = 2.6$ ms corresponding to about 3.8 Mio time steps with an average time step $dt_1 \approx 6.8\text{e-}10$

s for the I channel and corresponding to about 2.9 Mio time steps with an average time step $dt_K \approx 8.9\text{e-}10$ s for the K channel.

In the simulation, we do not evaluate the wall material erosion but consider the wall stress. For the evaluation of the wall stress we cut-off the pressure at the wall to tell apart the bulk pressure from the high pressure peaks. We assume that these pressure peaks determine the wall stress. For the cut-off a series of threshold values THR is utilised. At the end we obtain a pressure erosion probability P_P as a function of the wall coordinate that is evaluated by the ratio of pressure peaks exceeding the threshold and the total number of the prescribed analysis time steps. The same procedure is applied by another erosion indicator but the pressure, namely the force on a wall cell, i.e. pressure times the wall face area, defining the force erosion probability P_F . The force is less grid dependent than the pressure due to a partly compensation of the lower pressure by a higher wall face area if the grid is coarsened³. We assume that the location of highest P_P or P_F indicates the starting point of erosion and therefore we assume P to be an appropriate measure to be compared to the experimental erosion findings. The erosion analysis time is $\Delta t = 1.5 \dots 2.6$ ms (t_{end}).

In order to illustrate that the numerical method resolves the vapour cloud collapse, in Fig. 9 time sequences of the vapour volume fraction α and the pressure p are depicted. At the time t_0 a vapour cloud collapses and is almost vanished at time t_1 . At the same time t_1 , a pressure peak occurs that moves as a shock wave through the fluid, touches the wall at time t_2 and leaves the channel by its exit at time t_3 .

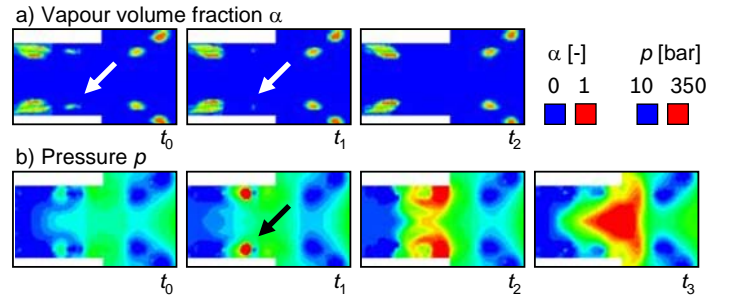


Fig. 9: Simulation time sequences of a) the vapour volume fraction and b) the pressure at the channel exit with a time interval $\Delta t = 6.8\text{e-}8$ s. The images are mirrored about the channel mid-axis.

In the experimental investigations, the operation points have been chosen in a way that the time-averaged cloud collapse location (CCL) defined by a rapid stream-wise cavitation probability decrease occurs at about 80 % channel length. In the simulation, we aim at having the same CCL. The cavitation probability in the simulation is defined in the following way which we assume to be most comparable to the experimental procedure. First, a threshold of the vapour volume fraction is

³ Albeit we have not studied the grid dependence of the erosion indicators rigorously we have evaluated the lower grid dependence of P_F in preliminary tests that are not documented here.

defined above which the liquid-vapour mixture in any cell is assumed to be impervious to light. We have found only a minor dependence of the results on thresholds ranging between 1 % and 30 % so that each following illustration has been generated by a threshold of 3 %. To evaluate the cavitation probability, a time average of 2000 instances with a time interval of $\Delta t \approx 8e-8$ s corresponding to 100 time steps has been performed. The result is depicted for the channel I in Fig. 10. The CCL in the simulation is determined rather arbitrarily at a cavitation probability of 20 %.

The outlet pressure has a significant impact on the location (CCL) and intensity of the highest wall stress magnitude WSM. This is illustrated in Fig. 10 and Fig. 11 where the CCL and P_F are depicted for the I channel and different outlet pressures. When p_{out} is increased, the CCL moves further upstream; the maximum of P_F moves upstream as well and is higher or lower than for the nominal $p_{out} = 125$ bar, subject to THR.

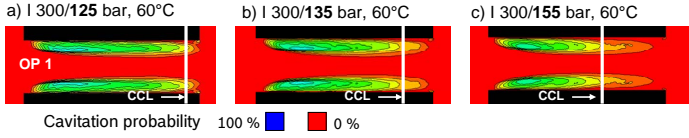


Fig. 10: Simulation: cavitation probability of the OP 1 (a) with a variation of the outlet pressure (b and c). The white vertical lines indicate the collapse CCL_{sim} within the channel defined by the 20 % iso-line. The image is mirrored about the channel mid-axis.

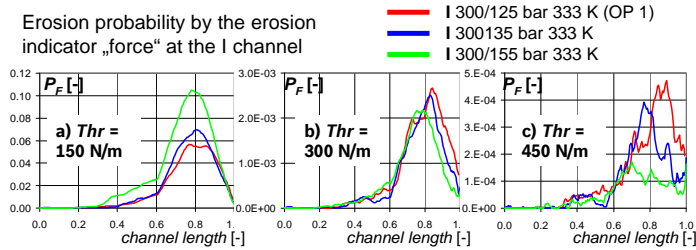


Fig. 11: Erosion probability P_F by the indicator “force” at the I channel with a variation of the outlet pressure p_{out} for the thresholds a) THR = 150 N/m, b) THR = 300 N/m and c) THR = 450 N/m

Since the CCL has such a strong influence on the erosion simulation results, a correction of the outlet pressure is done in a way that the measured CCL is matched. In the following, both, the nominal outlet pressure as well as the corrected outlet pressure results are discussed.

Influence of the pressure level

We start by assessing the capability of our computations to predict the pressure level influence on erosion considering the PREVERO-2 test cases.

Regarding the cavitation probability and the CCL, Fig. 12 shows the experimental and simulation results of OP 6 – 8. According to the experiment, the CCL is close to the channel exit for OP 6 and 7 and at about 70% channel length for OP 8. While the CCL of OP 6 and 7 is well captured by the simulation, for OP 8 it is located further downstream than the measured value. Consequently, the outlet boundary condition is corrected for the OP 8 by an outlet pressure increase to $p_{out} = 195$ bar.

Comparing Fig. 12 c, f and g, the corrected CCL matches the measured value much better.

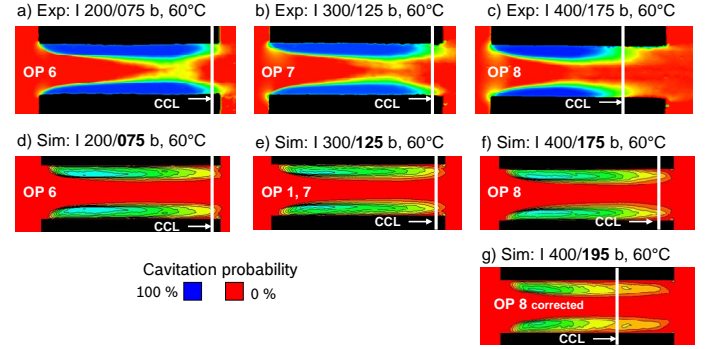


Fig. 12: Experimental (a-c) and simulation (d-g) cavitation probability of the PREVERO-2 cases OP 6 - 8. The white vertical lines indicate the CCL within the channel defined by the 20 % iso-line. For OP 8 the outlet pressure is increased in a way that the measured CCL is matched (g). For the simulation results, the image is mirrored about the channel mid-axis. Due to the depth-average, the experimental images can be compared to the simulation results only with regard to the CCL.

The corresponding results of P_P and P_F are documented in Fig. 13. Irrespective if the CCL is corrected to a more upstream position for OP 8, the tendency of the experiment – increasing erosion with increasing pressure level – is well captured by both, P_P and P_F and all considered threshold values THR.

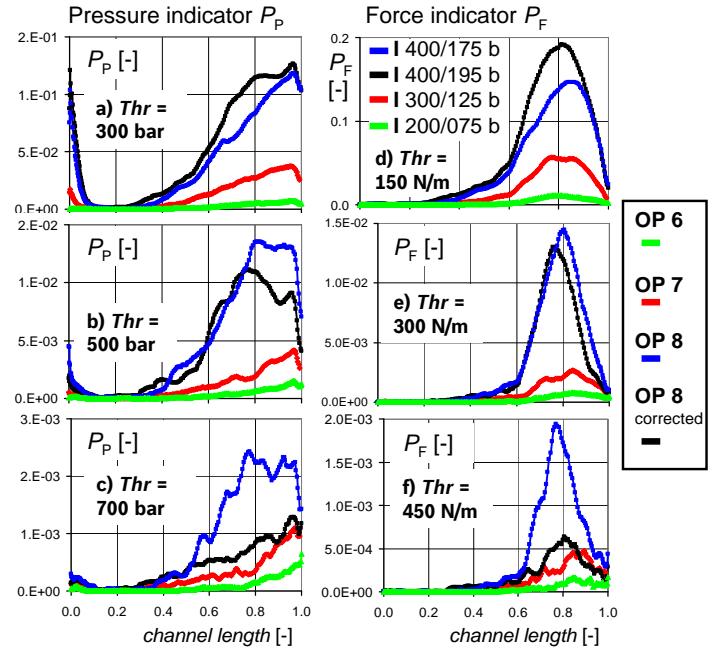


Fig. 13: Erosion probability by the pressure (a-c) and the force (d-f) indicator with different thresholds for the variation of the pressure level, OP 6-8. OP 8 with corrected outlet pressure is also shown.

Influence of the inlet radius and the outlet pressure

We consider the OP 1, 2 and 3 in Tab. 1. At first we consider the mass flow that we have found to be independent of the

temperature in the experiment as well as in the simulation. The simulation mass flow shows strong oscillations which are approximately 50 % higher at the outlet than at the inlet, Fig. 14 a. Note that the time averaged mass balanced is fulfilled due to the conservative properties of the numerical scheme. For a first order UDS (no reconstruction), the oscillations are much lower in particular for the higher outlet pressure at OP 1 and 2.

For the K channel with $p_{\text{out}} = 115$ bar and the UDS scheme the oscillation is nearly harmonic with an approximate oscillation period $\tau = 25\text{e-6 s}$. Assuming an average speed of sound $c \approx 1250 \text{ m}\cdot\text{s}^{-1}$ we obtain the corresponding wave propagation length $L_{\text{wave}} \approx 0.03 \text{ m}$ which is approximately twice as long as the distance between the channel and the calculation domain outlet $L_{\text{wake}} = 0.1 \text{ m}$. Therefore, it is obvious that the oscillations are enhanced by the wave reflection at the outlet boundary where we have implemented a reflecting Dirichlet pressure condition.

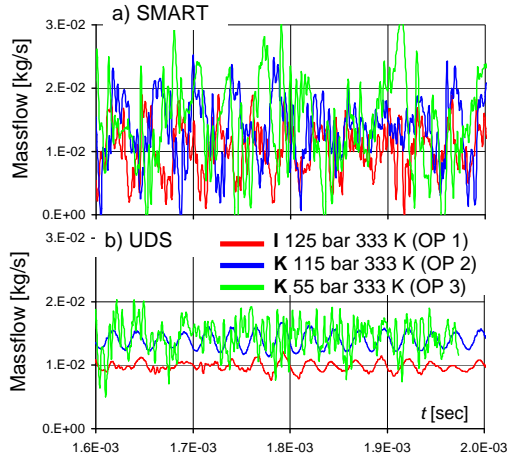


Fig. 14: Temporal evolution of the outlet mass flow within a time interval between $\Delta t = 1.6$ and 2.0 ms. Comparison of a) SMART scheme and b) UDS.

For both channel geometries we do a time average of the simulation mass flow in a time interval $\Delta t = 1.5 \dots 2.6 \text{ ms}$ (t_{end}) and compare the results to measurements, see Fig. 15. As a reference we have performed simulations with a steady incompressible pressure-based viscous solver with $k-\epsilon$ turbulence and without cavitation model where the constant solver density corresponds to the barotropic law density at $p = 125$ bar. For the I channel, the incompressible result shows a very good agreement with the measurement which is astonishing since we have neglected the side-wall friction in our 2D setup and expect therefore an over-estimation of the mass flow. In fact, this over-prediction is present for the K channel and we therefore assume that the experimental I channel mass flow may be too high due to a very small but higher-than-zero inlet radius in the order of a few μm . Although the plane channel samples have been inspected by a microscope we have to take into account a geometry measurement accuracy of not less than 5 % and a mass flow measurement accuracy of not less than 10 %. Therefore, the measured mass flow depicted in Fig. 15 is rather a hint than a real reference for the simulation results.

In order to demonstrate the grid sensitivity of the results we have performed simulations with a grid that is about four times as coarse in each direction corresponding to a cell size $L_{\text{cell}} = 20 \mu\text{m}$ within the channel. For the coarse grid, the time step is about three times as large due to the explicit time scheme. The time-averaged mass flow rate obtained by CATUM shows only a minor dependence on the spatial resolution and on the order of the spatial discretisation.

Summarizing, we assume that the mass flow rate in the density-based CATUM solver is dominated by dynamical effects (oscillations in Fig. 15) induced by the neglect of the third space dimension and the neglect of the viscous terms.

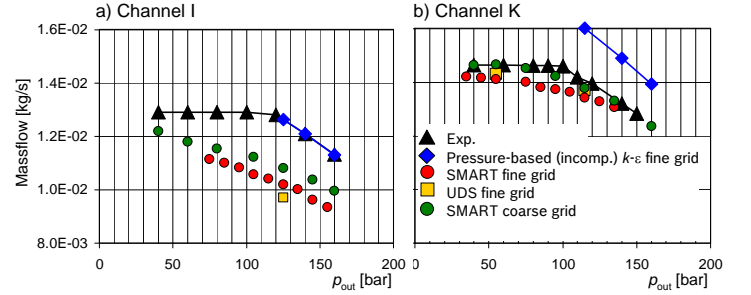


Fig. 15: Time averaged mass flow in dependence on the outlet pressure for a) the I channel and b) the K channel

Since the time-averaged mass flow on the coarse grid does not dramatically deviate from the one on the fine grid, we have had the hope that we do not need a too fine grid for the erosion analysis. Fig. 16 shows time plots of the maximum pressure in the entire domain for both grids. Obviously, the pressure maximum correlates with the spatial resolution. This is due to the different collapse strengths on both grids. As a consequence, the erosion indicators need to be chosen in dependence on the spatial resolution. For the further investigations we only utilise the fine grid with a spatial resolution of about $L_{\text{cell}} = 5 \mu\text{m}$.

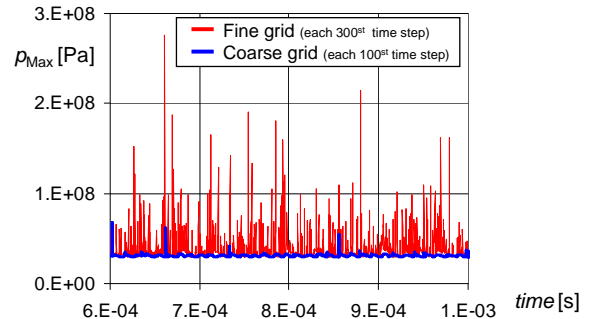


Fig. 16: Temporal evolution of the maximum pressure within the entire computational domain of channel I (OP 1) for the fine and the coarse grid. Fine grid: each 300th time step shown. Coarse grid: each 100th time step shown.

Let us explore the erosion results now. For all simulations the results obtained with nominal outlet pressure as well as with the outlet pressure adjusted to match the experimental CCL are discussed. Fig. 17 shows the cavitation probability without and with adjusted outlet pressure in comparison to the experimental data.

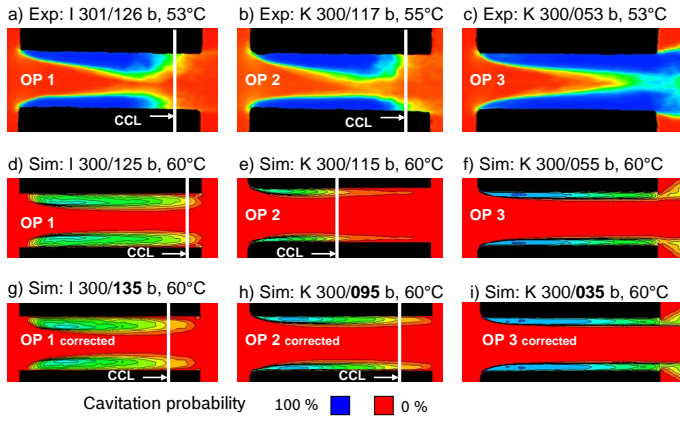


Fig. 17: Experimental (a-c) and simulation (d-i) cavitation probability of the PREVERO-1 cases, OP 1 - 3. The white vertical lines indicate the CCL within the channel defined by the 20 % iso-line. In the simulation, for both high outlet pressure cases (OP 1 and 2) the outlet pressure is increased in a way that the measured CCL is matched (g and h). For the low pressure case (OP 3) the outlet pressure is decreased to ensure that the CCL is certainly not located within the channel (i). For the simulation results, the image is mirrored about the channel mid-axis. Due to the depth-average, the experimental images can be compared to the simulation results only with regard to the CCL.

In Fig. 18, the erosion probability results are shown for the nominal outlet pressures, i.e. with an incorrect CCL in the simulation according to Fig. 17 d-f. For the lowest thresholds, the experimental results are well matched. For higher thresholds, however, in particular the difference between the K channel with different outlet pressures, OP 2 and 3, becomes indifferent. According to Fig. 19, this result changes significantly if the outlet pressure is adjusted according to Fig. 17 g-i: the equal WSM of both, K channel and I channel with high outlet pressure becomes obvious, in particular for the highest threshold for both, P_P and P_F . Also the lower load of OP 3 is more pronounced.

Influence of the fuel temperature

Despite the fact that we utilise a barotropic EOS and therefore do not consider energetic effects, different fluid temperatures are characterized by the different entropies according to Fig. 1. For channel K, we analyse if the much faster erosion of OP 2 (hot) compared to 5 (cold) is reflected in the simulation by the application of two different EOS corresponding to two entropies. For this temperature effect study, we have skipped the p_{out} (or rather CCL) correction since we have found that the CCL hardly depends on the entropy level of the EOS and we can do the temperature (or rather entropy) comparison at any CCL.

The results are shown in Fig. 20 for P_F . Since the WSMs of both temperatures do hardly deviate from each other, we can summarize that the barotropic EOS is not suitable to characterize the fluid temperature difference that leads to significantly higher erosion rates for hot conditions.

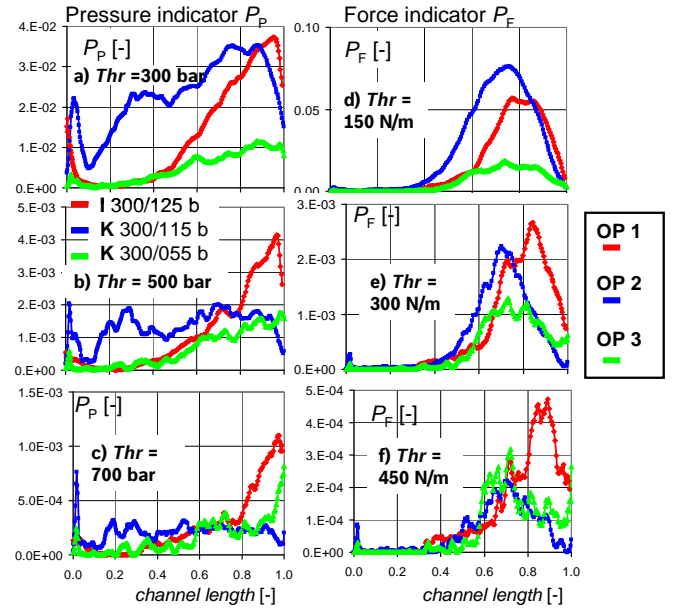


Fig. 18: Erosion probability by the pressure (a-c) and the force (d-f) indicator with different thresholds for the variation of the inlet geometry and the outlet pressure, OP 6-8. The nominal outlet pressure according to Fig. 17 d-f is used.

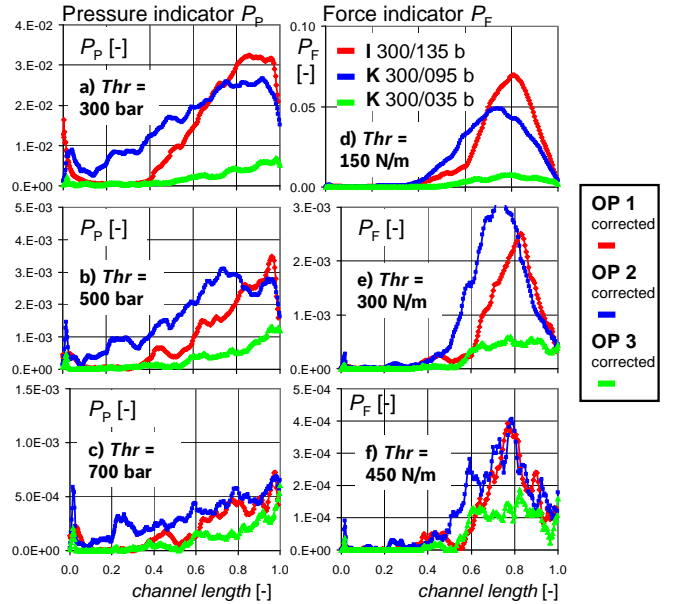


Fig. 19: Erosion probability by the pressure (a-c) and the force (d-f) indicator with different thresholds for the variation of the inlet geometry and the outlet pressure; OP 6-8. The outlet pressure has been adjusted according to Fig. 17 g-i.

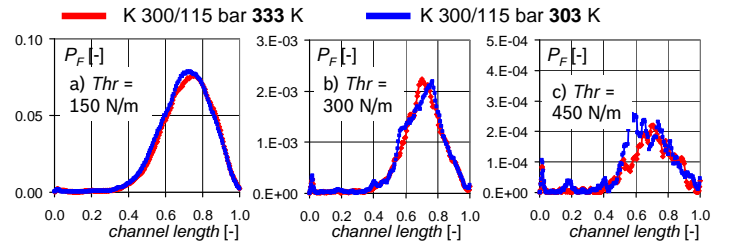


Fig. 20: Erosion probability for two temperatures for the K channel (OP 2 vs 5)

6. CONCLUSIONS

We have compared the material erosion in the experiment with the wall stress magnitude WSM (or cavitation probability P) in the simulation. This cavitation probability is a measure how often a prescribed threshold value of the pressure is exceeded. We are working on erosion models that directly yield the erosion rate but assume that the critical feature that has to be resolved correctly in the simulation is not so much the erosion itself but rather the flow that makes up the origin of the wall load and damage.

We have investigated the influence of the **pressure level** on the erosion process and have found that we can capture this effect very well irrespective of the threshold value.

In the experimental investigations, we do not observe significant differences in the erosion rate for various **inlet geometries**. Instead, the experimental investigations imply that the wall load leading to the erosion start is not a function of the inlet geometry but mainly a function of the pressure level. The geometry influence enters indirectly via the outlet pressure. At constant inlet pressure, the outlet pressure has to be lower for the round K channel than for the sharp I channel in order to obtain the same CCL within the channel. The simulation results reproduce the similar load of both inlet geometries if we set the CCL equal for both geometries by a careful outlet pressure adjustment.

Regarding the **outlet pressure** influence for the round K channel the experiments obviously tell us that the CCL should be within the channel in order to lead to erosion within the channel. As for the inlet geometry influence, this effect is captured by the simulation only if the outlet pressure level is adjusted in a way that the experimental CCL is matched. This outlet pressure adjustment plays essentially the role of an overall correction of simplifications as the neglect of the third dimension or the neglect of viscous effects.

Let us discuss the threshold influence. We assume two limiting cases of the wall load that leads to erosion: First, relatively low peaks that occur quite frequently may cause this load or secondly very high peaks that occur quite seldom may have the same damaging effect. The first case is captured by a relatively low threshold and the second case by a high threshold. We do not find a significant hint in our simulations which case is physically more correct and assume that the application of collapse indicators that are introduced in our companion paper [12] will give us a clarification.

Note that the absolute threshold level itself is not significant since we are aware of a strong grid dependence of the pressure peaks. What is significant is that the spatial resolution of both channel geometries is the same. Based on a given spatial resolution we have to find threshold values that cause a suitable range of P , say between a fraction of a per-mill and several percents.

Regarding **temperature** influences, we do not see any hint that the barotropic model can capture the effect of different fluid temperatures. We are aware of the fact that different fluid temperatures can have an immediate effect on cavitation by different collapse intensities or a mediate effect by different solved air contents in the fluid.

The predicted mass flow is to our surprise lower than the measured one although we neglect viscous effects as well as the side walls of the test geometry. This is certainly due to a strong oscillation of the fluid motion which is enhanced by wave reflection at the inlet and particularly outlet boundary. Furthermore, no physical damping means is present as a third dimension or viscous dissipation.

It is critical that the exact position of the CCL within the channel is captured in the simulation since it has a significant influence on the erosion result. We conclude that we have the following features to take into account in order to obtain a more reliable flow, i.e. CCL and mass flow prediction:

- Three-dimensional flow: not only the effect of side walls but also the inviscid flow instabilities themselves can lead to three-dimensional effects.
- Viscous effects: turbulence and friction are important mechanisms that particularly together with three-dimensional simulations must be taken into account.
- Boundary conditions: the strong reflection of pressure waves influence the flow in an unphysical way so that the time-average mass flow deteriorates to a lower value than the measured one.
- Cavitation modeling: the energy equation is necessary to omit the isentropic assumption and is indispensable to capture fluid temperature influences on the cavitation erosion in the context with air release modeling.

All four features are the subject of our further research on cavitation erosion predictions and will be addressed in subsequent publications of the author group. Besides the CFD-method improvements themselves we are working on improvements of our collapse detection and erosion indicator analyses.

We are convinced that we have introduced a break-through methodology that brings us on the way to erosion predictions.

ACKNOWLEDGMENTS

We like to thank Prof. Rudolf Schilling, director of the Institute of Fluid Mechanics, Munich University of Technology, for the kind provision of the flow solver NS2D.

REFERENCES

- [1] A. Berg, U. Iben, A. Meister, J. Schmidt, "Modeling and simulation of cavitation in hydraulic pipelines based on the thermodynamic and caloric properties of liquid and steam.", *Shock Waves*, Vol. 14, Issue 1-2, pp. 111-121, DOI 10.1007/s00193-005-0252-y, 2005
- [2] M. Bogner, B. Flurl, R. Schilling, "Simulation of cavitating flows in hydraulic turbomachinery.", *Conf. Modelling Fluid Flow*, 2009
- [3] M. Frobenius, R. Schilling, J. Friedrichs, G. Kosyna, "Numerical and experimental investigations of the cavitating flow in a centrifugal pump impeller.", *Proc. ASME Fluids Engineering Division summer meeting*, 31006, 2002

- [4] M. Frobenius, R. Schilling, R. Bachert, B. Stoffel, G. Ludwig, "Three-dimensional unsteady cavitation effects on a single hydrofoil and in a radial pump – measurements and numerical simulations.", 5. Int. Symp. Cavitation, 2003
- [5] P. H. Gaskell, A. K. C. Lau, "Curvature-compensated convective transport: SMART, a new boundedness-preserving transport algorithm.", Int. J. Num. Meth. Fluids, Vol. 8, pp. 617-641, 1989
- [6] D. Greif, D. M. Wang, "Aspects of modelling cavitation effects within injection equipment using advanced two-fluid techniques.", Turbulence, Heat and Mass Transfer, Vol. 5, 2007
- [7] A. Harten, "High-resolution schemes for hyperbolic conservation schemes.", Phys. Fluids, Vol. 49, No 3, pp. 357-393, 1983
- [8] U. Iben, "Modelling of cavitation.", System Analysis Modelling Simulation, Vol. 42, No. 9, pp. 1283-1308, 2002
- [9] U. Iben, F. Wrona, C.-D. Munz, M. Beck, "Cavitation in hydraulic tools based on thermodynamic properties of liquid and gas.", J. Fluids Engineering, Vol. 124, pp. 1011-1017, 2002
- [10] U. Iben, A. Morozov, F. Wolf, "Laser-pulsed interferometry applied to high-pressure fluid flow in micro-channels.", Exp. Fluids, Vol. 50, pp. 597-611, 2011
- [11] U. Iben, A. Morozov, E. Winklhofer, R. Skoda, "Optical investigations of cavitation flow phenomena in micro channel using a nano second resolution.", WIMRC 3, 2011
- [12] M. Mihatsch, S. J. Schmidt, M. Talhammer, N. A. Adams, R. Skoda, U. Iben, "Detection of Collapses in Compressible 3-D Cavitating Flows and Numerical Prediction of Erosion Sensitive Areas.", WIMRC 3, 2011
- [13] M. S. Plesset, A. Prosperetti, "Bubble dynamics and cavitation.", Annu. Rev. Fluid Mech., Vol. 9, 145, 1977
- [14] J. Sauer, "Instationär kavitierende Strömungen - Ein neues Model, basierend auf Front Capturing (VoF) und Blasendynamik.", Ph.D. thesis, Universität Karlsruhe, 2000
- [15] S. J. Schmidt, I. H. Sezal, G. H. Schnerr, "Compressible simulation of high-speed hydrodynamics with phase change.", ECCOMAS CFD, 2006
- [16] S. J. Schmidt, I. H. Sezal, G. H. Schnerr, M. Talhammer, M. Förster, "Compressible simulation of liquid/vapour two-phase flows with local phase transition.", 6. int. Conf. Multiphase Flow, 2007
- [17] S. J. Schmidt, I. H. Sezal, G. H. Schnerr, M. Talhammer, "Shock waves as driving mechanism for cavitation erosion.", Proc. 8. Int. Symp. Exp. Comp., ISAIF 8, 2007
- [18] S. J. Schmidt, I. H. Sezal, G. H. Schnerr, M. Talhammer, "Riemann techniques for the simulation of compressible liquid flows with phase-transition at all Mach number – shock and wave dynamics in cavitating 3-D micro and macro systems.", AIAA paper 2008-1238
- [19] S. J. Schmidt, I. H. Sezal, G. H. Schnerr, M. Talhammer, "Numerical analysis of shock dynamics for detection of erosion sensitive areas in complex 3D-flows.", WIMRC 2, 2008
- [20] S. J. Schmidt, M. Mihatsch, M. Talhammer, N. A. Adams, "Assessment of the prediction capability of a thermodynamical cavitation model for the collapse characteristics of a vapor-bubble cloud.", WIMRC 3, 2011
- [21] G. H. Schnerr, S. J. Schmidt, I. H. Sezal, M. Talhammer, "Shock and wave dynamics of compressible flows with special emphasis on unsteady load on hydrofoils and on cavitation in injection nozzles.", 6. Int. Conf. Multiphase Flow, 2007
- [22] G. H. Schnerr, I. H. Sezal, S. J. Schmidt, "Numerical investigation of three-dimensional cloud cavitation with special emphasis on collapse induced shock dynamics.", Phys. Fluids, 20, issue 4, 040703, 2008
- [23] R. Skoda, R. Schilling, J. Thurso, B. Stoffel, "Numerical simulation of unsteady and transitional flows pertaining to turbine cascades.", Eng. Turbulence Modelling Measurements 5, 2002
- [24] R. Skoda, R. Schilling, M. T. Schobeiri, "Numerical simulation of the transitional and unsteady flow through a low pressure turbine.", Int. J. Rotating Machinery, DOI 10.1155/2007/10940, 2007
- [25] H. Thermann, M. Müller, R. Niehuis, R. Skoda, R. Schilling, "Numerical simulation of the flow in an annular compressor cascade with different turbulence and transition models.", 5th Eur. Conf. Turbomachinery, 2003
- [26] W. Yuan, G. H. Schnerr, "Cavitation in injector nozzles, effect of injection pressure fluctuations.", Proc. 4. Int. Symp. Cavitation, 2001

APPENDIX – IMPLEMENTATION VERIFICATION

The correct implementation of the CATUM scheme in NS2D is verified by three Riemann problems:

1. Gaseous air ($p_L = 1$ bar, $T_L = 348.4$ K, $p_R = 0.1$ bar, $T_R = 278.8$ K)
2. Liquid water non-cavitating ($p_{\text{vap}} = 7326$ Pa, $p_L = 100$ bar, $\rho_L = 996.5$ kg·m⁻³, $p_R = 1$ bar, $\rho_R = 992.3$ kg·m⁻³)
3. Liquid water cavitating ($p_{\text{vap}} = 7326$ Pa, $p_L = 1$ bar, $\rho_L = 992.3$ kg·m⁻³, $p_R = 5000$ Pa, $\rho_R = 2.97$ kg·m⁻³)

The following figures show the temporal progress of the waves and give an impression of the correct functionality of NS2D.

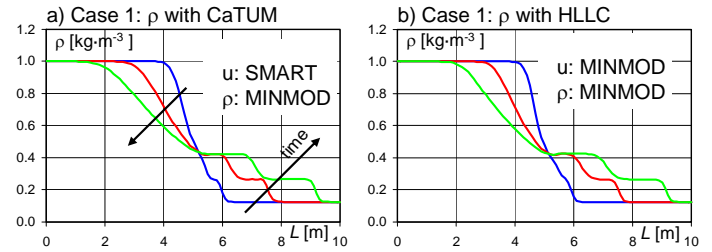


Fig. 21: Riemann problem 1: density for CATUM vs HLLC

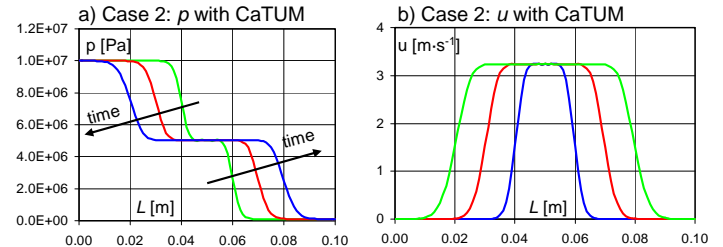


Fig. 22: Riemann problem 2: density and velocity with CATUM

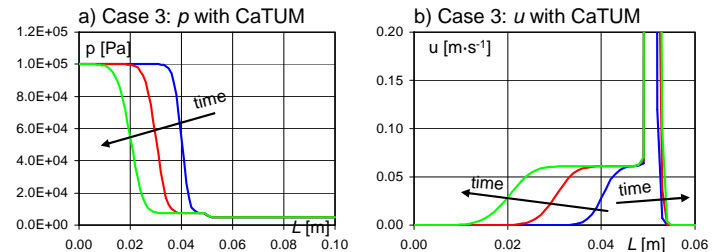


Fig. 23: Riemann problem 3: density and velocity with CATUM

Cavitating Flow Analysis for Flow past a Valve in an Artificial Heart or Ventricular Assist Device

C.K. Huang

Jiahn-Horng Chen*

Department of Systems Engineering and Naval Architecture
National Taiwan Ocean University, Keelung, Taiwan
*E-mail: b0105@mail.ntou.edu.tw

ABSTRACT

Cavitation was first related to valves of a mechanical heart in the 1980s after a series of valve fractures of a particular valve were observed. In the present study, the cavitating flow phenomena are computationally studied with the assumption that the valve motion is known. We focus on the effects of closing velocity of the valve on the flow development since it is known that cavitation often occurs at the moments when the valve is closing due to the fact that at these moments, the local flow often accelerates and results in a local high velocity distribution. A viscous flow model is incorporated with a dynamic mesh strategy to cope with the movement of the valve. Furthermore, the simulation of cavitation is modeled by the “full cavitation model,” which takes into considerations the first-order effect of the formation and transport of vapor bubbles, the turbulent fluctuations of pressure and velocity, and the magnitude of non-condensable gases. In addition, we also assume that the liquid phase is incompressible, but the gas phase is compressible, and all parameters and physical variables are independent of temperature.

INTRODUCTION

The heart is a vital organ of living creatures and provides the blood transportation in the human body. Heart failure results in serious inability of the heart to supply sufficient blood flow to meet the need of the body. Extracorporeal assistance is needed to provide cardiac support to those who suffer from the heart failure. Many techniques are available in the modern medicine. Some examples include the extracorporeal membrane (ECMO) and various kinds of ventricular assist devices. The latter can be divided into three categories in terms of the ways of pumping. They are the continuous axial-flow type, the continuous centrifugal-flow type, and pulsatile-flow type. In any type of these devices, the artificial heart valve is an important part to control the direction of blood flow.

In fact, the artificial heart valve is indispensable not only in assist devices, but also in human body when the natural valves fail or malfunction. However, several fatal issues have been identified for the artificial valves used in ventricular assist devices due to hemodynamic problems. In fact, the development of mechanical valve design has a long history since the first implantation of the device with the caged valve developed by Hufnagel [1] in 1952. Its durability and safety for long-term

operation have been in the list of key issues. Nevertheless, non-physiological factors which make blood flow chaotic have not been yet successfully and fully circumvented.

The mechanical heart valve is a moving part which controls the blood flow, maintains the correct pumping action, and prevents the blood flow from reversing direction. One of the major issues concerning its design is cavitation which may occur in its operation. Through extracorporeal detections, cavitation was first related to mechanical heart valves in 1980s after a series of valve failures. Since then, various studies on how to detect and prevent from valve cavitation have been conducted. Cavitation damages the valves and formed elements of blood, reduces the efficiency of blood flow pumping, and enhances the risk of thromboembolic complications. Therefore, the detection and prevention of cavitation are vital to clinical medicine.

Klepetko *et al.* [2] observed microscopic pitting on a bi-leaflet valve after 36 and 38 months of the Edwards-Duromedics valve implantation. The leaflet fracture on the valve was found. Technical evaluation also revealed crack growth due to fatigue fracture. In addition to damaging the valve, cavitation also results in damage of blood due to its unique physical phenomena. It is known that cavitation bubbles form when the local fluid pressure is reduced to the vapor pressure and collapse as the local pressure increases. The collapse of bubbles induces very strong micro-jets which significantly disturb the blood flow. Furthermore, the pressure fluctuation is one of the physiological factors to activate blood platelets and damage blood cells. The platelet results in thrombosis, and prevent blood clotting in medical process is use anti-coagulant.

The valve cavitation usually occurs at the instant when the valve is almost closed. This is due to the fact that the local velocity around the valve tip rises up by the enhancement of the valve closing velocity. The physical mechanisms which may be involved in its appearance include squeeze flow, water hammer effect, formation of strong vortices, and venturi effect [3]. The squeeze flow during the valve closure accelerates fluid particles passing across the valve tip. The water hammer effect due to valve closure results in a lower pressure.

Most of studies on cavitation of mechanical heart valves were conducted through extracorporeal investigation [4-5]. Lee *et al.* [6-7] used a high speed camera to investigate cavitation bubbles and quantify the intensity of cavitation on mechanical heart valves. They pointed out that the cavitation intensity was

related to the closing velocity of the valve and the pressure variation. They also studied the effect due to different heart beating frequencies and found that a higher frequency led to longer cavitation duration. Their conclusion confirms that a higher blood flow rate enhances a higher closing velocity which, in turn, brings about cavitation on the tip of the mechanical heart valve.

Recently, computational fluid dynamics has become an important branch in bio-fluid mechanics. Avrahanmi *et al.* [8] employed the approach of computational fluid dynamic to analyze the influence of cavitation on valves from the vorticity magnitude. Lai *et al.* [9] simulated by computations the two-dimensional valve closure dynamics of a bi-leaflet valve in a channel. They determined the occurrence of cavitation in an indirect way by observing the computed pressure variation in time rather than employing the cavitation model.

Since it is difficult to conduct a direct experimental observation of cavitating flows around a mechanical heart valve, computation becomes an important alternative to understand the mechanism of cavitation due to a particular valve. However, few computational studies of mechanical heart valve cavitation available in the literature employed proper cavitation models for detailed analyses. In the present study, we employed the full cavitation model to simulate the phenomena of cavitating flow. We focus on the valve closure dynamic in a 2D channel. The effect of the hinge point on cavitation duration and vortices around the tip of valve was also investigated.

MATHEMATICAL MODEL

Shown in Fig. 1, a two-dimensional channel flow driven by pressure passes a bi-leaflet rotating valve. To focus on the particular flow phenomena due to valve closure, we truncate the flow domain and focus on the flow development in the region near the valve. The length of the truncated flow region is L and with of the channel is $2w$. Point O represents the hinge point of the rotating valve. The lengths from point O to both ends are ℓ_1 and ℓ_2 , respectively.

The gauge pressures distributions at the inlet and outlet are $P_{\text{inlet}}(t)$ and $P_{\text{outlet}}(t)$, respectively. In the present study, $P_{\text{inlet}}(t)$ varies with time and $P_{\text{outlet}}(t)$ keeps constant. Of course, to drive the flow from the inlet to the outlet, we must have $P_{\text{inlet}}(t) \geq P_{\text{outlet}}(t)$. Furthermore, the valve is subject to motion due to the fluid motion and rotates around point O .

In this study, we assume that the mechanical heart valve rotates at a prescribed angular velocity $\omega(t)$ from the upright position at $t = 0$ till the valve closure. The angle of rotation from the upright position at time t is denoted as $\theta(t)$.

Since cavitation occurs in the flow domain at some time due to the valve closure, we need to incorporate a suitable the physical model of cavitation in the analysis. The flow is essentially multi-phase. Furthermore, the fluid may change its phase from liquid to gas and vise versa. For a multi-phase flow, the continuity equation may be written as follows,

$$\frac{\partial \rho_m}{\partial t} + \nabla \cdot (\rho_m \mathbf{u}_m) = \dot{m} \quad (1)$$

where the ρ_m is the density of mixture, defined as

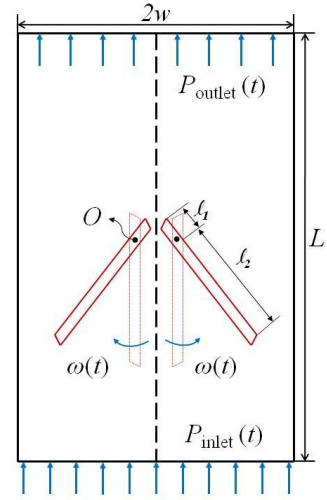


Fig. 1 A 2-D channel flow passes a rotating valve.

$$\rho_m = \sum_{k=1}^2 \alpha_k \rho_k \quad (2)$$

\mathbf{u}_m is the speed of mixture, defined as

$$\mathbf{u}_m = \frac{\sum_{k=1}^2 \alpha_k \rho_k \mathbf{u}_k}{\rho_k} \quad (3)$$

and \dot{m} is the changing rate of mass result from bubbles formation.

Moreover, the momentum equations can be expressed as

$$\rho_m \left[\frac{\partial \mathbf{u}_m}{\partial t} + \nabla \cdot \mathbf{u}_m \mathbf{u}_m \right] = -\nabla P + \nabla \cdot [\mu_m (\nabla \mathbf{u}_m + \nabla \mathbf{u}_m^T)] + \nabla \cdot \left[\sum_{k=1}^2 \alpha_k \rho_k \mathbf{u}_{\text{dr},k} \mathbf{u}_{\text{dr},k} \right] \quad (4)$$

where P represents the pressure, and μ_m is the viscosity, defined as

$$\mu_m = \sum_{k=1}^2 \alpha_k \mu_k \quad (5)$$

α_k is the volume fraction of phase k ($k = 1$ represent liquid, and $k = 2$ represent gas), and $\mathbf{u}_{\text{dr},k}$ is the drift velocity of phase k , defined as

$$\mathbf{u}_{\text{dr},k} = \mathbf{u}_k - \mathbf{u}_m \quad (6)$$

The turbulent model was incorporated in the computations. During the valve closure, the local velocity may become large. To cope with the local turbulence, the k - ω model was adopted in the present study. Take cavitating effects into consideration, we can express k and ω equations, respectively, as

$$\begin{aligned} \frac{\partial}{\partial t} (\rho_m k) + \nabla \cdot (\rho_m \mathbf{u}_m k) \\ = P - \beta^* \rho_m \omega k + \nabla \cdot \left[\left(\mu_m + \sigma_k \frac{\rho_m k}{\omega} \right) \nabla k \right] \end{aligned} \quad (7)$$

$$\begin{aligned} \frac{\partial}{\partial t}(\rho_m \omega) + \nabla \cdot (\rho_m u_m \omega) \\ = \frac{\gamma \omega}{k} P - \beta \rho_m \omega^2 + \nabla \cdot \left[\left(\mu_m + \sigma_\omega \frac{\rho_m k}{\omega} \right) \nabla \omega \right] \end{aligned} \quad (8)$$

To specify the boundary conditions, we first take advantage of symmetry of the bi-leaf valve setting and, therefore, solve the flow only on half of the flow domain. The condition of symmetry was applied along the centerline of the flow domain. Furthermore, no-slip boundary condition was specified on the wall. The fluid motion on the surface of the valve vanishes relative to the valve motion which was specified according to [9] in the present study. Moreover, the pressure distributions were specified at the inlet and outlet.

The “full cavitation model” proposed by Sinhal [10] was employed in computations. The effects which this model takes into considerations include the formation and transportation of cavitating bubbles, the turbulent fluctuations due to velocity and pressure fields, and incondensable gases. To employ this model, we also assumed for simplicity that the liquid and the gas are incompressible and that the phase changes are isothermal. Then the mass fraction of gas must satisfy the equilibrium equation,

$$\frac{\partial}{\partial t}(\rho_m f) + \nabla(\rho_m u_2 f) = \nabla(\gamma \nabla f) + R_e - R_c \quad (8)$$

where γ represents the effective factor of changing phases, and R_e and R_c respectively denote the phase change rate of gas and liquid, respectively. According to the Rayleigh-Plesset equation, we have

$$R_e = C_e \frac{V_{ch}}{\sigma} \rho_l \rho_v \sqrt{\frac{2(P_{sat} - P)}{3\rho_l}} (1 - f) \quad (8)$$

while $P > P_{sat}$ and

$$R_c = C_c \frac{V_{ch}}{\sigma} \rho_l \rho_v \sqrt{\frac{2(P - P_{sat})}{3\rho_l}} f \quad (9)$$

while $P_{sat} > P$. In the above equations, P_{sat} is the vapor pressure, the index l and v represent the liquid and vapor, respectively, V_{ch} is the characteristic velocity, σ is the surface tension, and C_e and C_c are the empirical constants. Considering the effect of turbulence which would enhance cavitation at a pressure higher than the saturation vapor pressure, we define the vapor pressure as

$$P_v = P_{sat} + \frac{P_{turb}}{2} \quad (10)$$

where

$$P_{turb} = 0.39 \rho_m k \quad (11)$$

NUMERICAL METHOD

The finite volume method was employed to discretize the governing equations. Then, the PISO (pressure implicit with splitting of operators) algorithm was used for nonlinear iterations. It is based on the SIMPLE method [11] and iterates pressure and velocity fields with high-order approximations. Compared to the classical SIMPLE and SIMPLEC algorithms, it leads to a better mass conservation and convergence. This is especially true in the computations of incompressible unsteady flows.

We employed the dynamic mesh methods to take account of the motion of the valve. In particular, the spring-based smoothing method was used for several time steps before the mesh around the moving boundary became severely distorted. The spring-based smoothing method updates the mesh without changing the mesh connectivity, and the edge between two grid nodes is an idealized interconnected spring. A displacement at the moving boundary node generates a “force” to move neighboring nodes along all “springs” connected to the node [12]. When the local mesh is severely distorted, the local remeshing technique was instead employed to regenerate a new mesh. The process was then repeated till the end of the computation.

RESULT AND DISCUSSION

In this study, the values of the parameters were set as follows: $L = 38.10\text{mm}$, $w = 12.21\text{mm}$, $\ell_1 = 1.79\text{mm}$ and $\ell_2 = 10.424\text{mm}$. Furthermore, the densities of fluid in liquid and gas phases are $\rho_1 = 1056 \text{ kg/m}^3$ and $\rho_2 = 0.5542 \text{ kg/m}^3$, respectively. The viscosities of fluid in liquid and gas phases are $\mu_1 = 0.0035 \text{ kg/m}\cdot\text{sec}$ and $\mu_2 = 1.34 \times 10^{-5} \text{ kg/m}\cdot\text{sec}$, respectively.

Shown in Fig. 2, the inlet and outlet pressure distributions follow the data available in [9]. In particular, at the inlet, the pressure increases at a rate of 2 mmHg/sec, and keeps constant as it reaches 120 mmHg. At the outlet, the pressure keeps constant. At time $t = 0$, the gauge pressures at the inlet and outlet are both zero.

As previously pointed out, the rotation motion was specified according to the experimental data in [9]. At time $t = 0$, the valve is upright positioned and perpendicular to the inlet as shown in Fig. 1. As the time lapses, its angular position follows the curve shown in Fig. 2. Since we did not have the raw data of the curve, we fitted it via three polynomials as shown in Fig. 3.

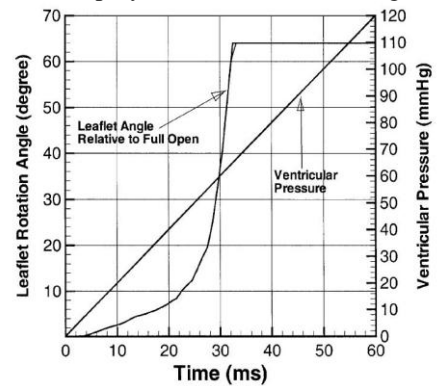


Fig. 2 Variation of $\theta(t)$ and $P_{inlet}(t)$ [9].

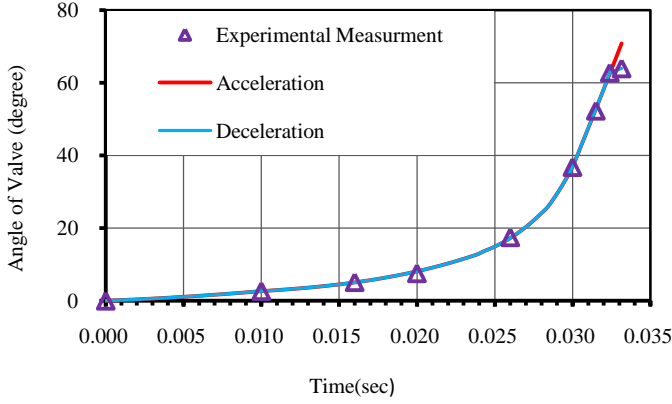


Fig. 3 The polynomial approximation to angular rotation of the valve.

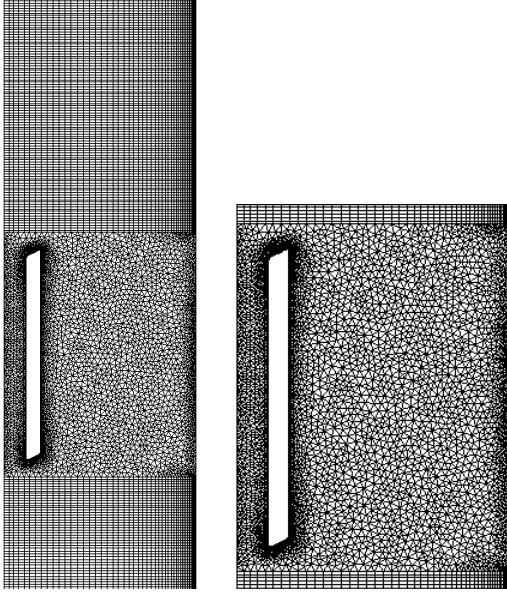


Fig. 4 The grid structure near the valve.

1. Grid Structure

To generate a suitable mesh for the present study, we divided the whole computational region into three parts. Shown in Fig. 4, the first part is around the valve and small in size. A structured orthogonal grid was generated which moves without distortion with the motion of the valve. The second part is the region far away from the rotating valve. Another structured orthogonal mesh was generated since the valve rotation has little influence on the mesh in this region. The third part lies between the first two parts. We employed a dynamic unstructured grid strategy in this part. The mesh nodes were updated in every time step.

2. Time Step Size

The cavitation during the valve closure usually takes place within hundreds of micro-seconds [13]. Since the duration is quite short, we have to be careful to choose proper time steps in computation if we want to accurately predict the cavitating flow. For comparison purposes, we first computed, with several different time steps, the laminar flow without cavitation and compared the results with those available in the literature.

Table 1 The maximum speed (in m/sec) obtained with different time step (laminar flow)

Δt (sec)	t				
	0.01	0.03	0.0315	0.0324	0.0325
2×10^{-5}	0.50	6.13	9.01	13.20	16.70
1×10^{-5}	0.52	6.23	8.94	13.36	16.54
5×10^{-6}	0.52	6.37	8.90	13.41	16.56
1×10^{-6}	0.53	6.27	8.93	13.51	16.56
Ref. [9]	0.52	5.96	8.86	13.28	N/A

Table 1 shows the maximum speeds at several different times. It is obvious that comparable results were obtained at a time step of $\Delta t = 2 \times 10^{-5}$ sec. The results obtained at a smaller time step do not vary significantly. In addition, it is interesting to find that the maximum local speed can reach a very large value due to the closure motion of the valve. It is evident that cavitation is very possible to take place at such a local high speed. Furthermore, the local flow can also be turbulent. Therefore, in the later computations, we incorporated with the cavitation model and turbulence model in order to predict the flow phenomena more accurately. In addition, we chose the time step to be 1×10^{-5} sec.

3. The Streamline of Flow Field

Fig. 5 shows the velocity field and the streamline at several different time before the cavitation takes place. First of all, it is interesting to find that results computed with the turbulence model are evidently different from those without the model. The maximum speeds at the time shown in the plots are usually much smaller than those obtained in the laminar flow computations. This seems to imply that in the simulation of the mechanical heart valve flow, it is vital to choose a proper model to predict the flow.

Observing the streamline patterns, we can easily find that the flow varies significantly at different stages of the valve closure. At the early stage of closure, the flow passing the valve very smoothly since the valve is almost upright and its blockading effect is not significant.

At $t = 0.03$ sec, a recirculating region forms on the back surface of the valve when two-thirds of the channel is blocked due to the rotation of the valve. Its appearance is expected because of the flow separation. This region grows as the valve keeps rotating to blockage the channel. A few moments later at $t = 0.0324$ sec, the recirculating region occupies about one-third of the back surface of the valve. It entraps fluid particles into a close area where there is no way for them to get out. As far as the blood flow is concerned, such a region should be avoided.

In addition, fluid particles passing around the ends of the valve accelerate. This phenomenon becomes more evident at the final stage when the channel is almost closed and the clearance between the valve tip and channel wall is small. In fact, between $t = 0.03$ sec and $t = 0.0324$ sec, the maximum speed increases drastically from 6.44m/sec to 10.44m/sec in the tip region of the long arm. Since the passage at these moments becomes very narrow, such a strong jet results in a high shear rate which damages blood cell and, in turn, enhances the risk of thrombosis.

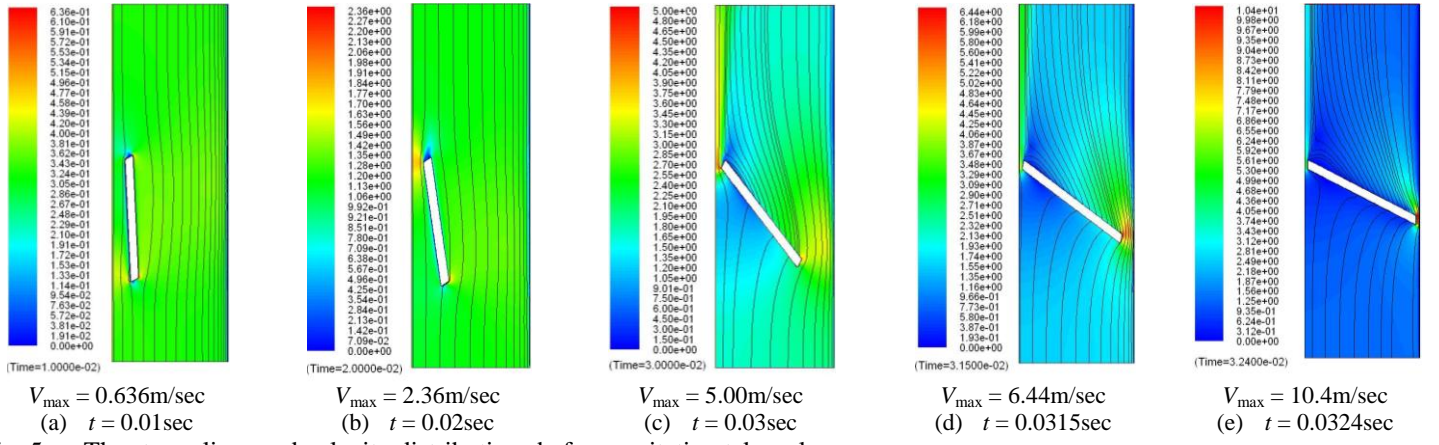


Fig. 5 The streamlines and velocity distributions before cavitation takes place.

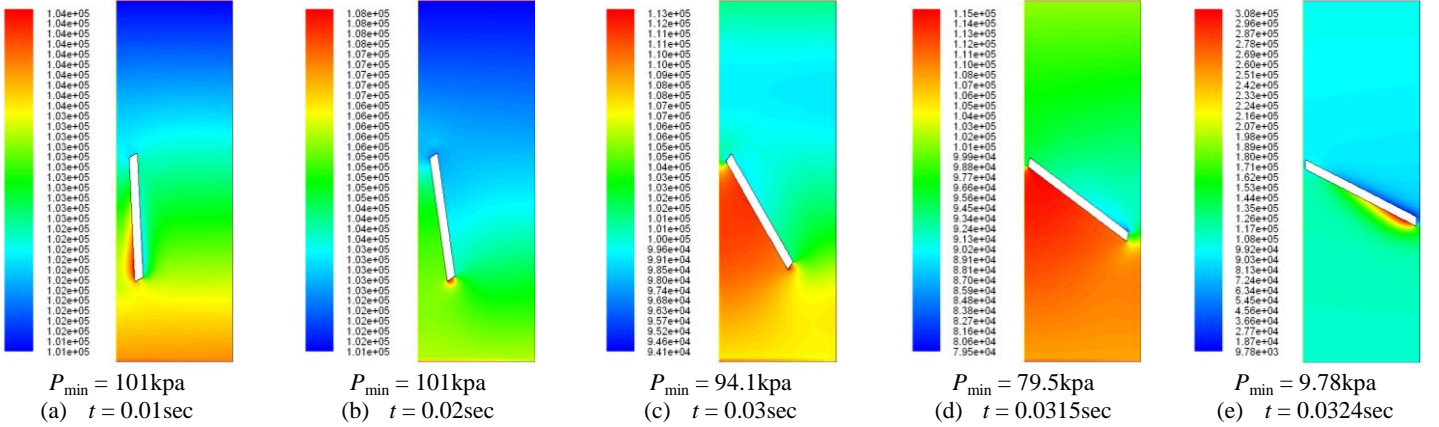


Fig. 6 The pressure distribution before cavitation takes place.

At the final stage, the velocity in most region of the channel decreases after $t = 0.03\text{sec}$. However, the local fluid speed around the tips of the valve is very high. With such a high velocity in the narrow clearance, a strong micro-jet is formed between $t = 0.03\text{sec}$ and $t = 0.0324\text{sec}$. Johnsen [14] pointed out that the micro-jet is the main factor to enhance cavitation on the valve closure.

4. Pressure Distribution

Fig. 6 shows the pressure distribution before cavitation. Since the pressure at the inlet keeps increasing linearly during the valve closure and the valve keeps rotating, the pressure distribution in the flow region varies significantly.

At earlier stage of valve closure, the passage is unblocked and the pressure variation from the inlet to the outlet is almost linear within the first 0.02sec, as shown in Fig. 6(a) and 6(b). Around $t = 0.03\text{sec}$, about two-thirds of the passage is blocked. Shown in Fig. 6(c), The pressure in the region which is upstream of the valve and blocked by the valve is very high. It is due to the almost stagnant flow in this region. For the unblock clearance, the variation of pressure has another story. Due to the fact that the pressure difference between the inlet and the outlet increases with time and the width of the unblocked clearance keeps decreasing, the flow velocity keeps increasing when the fluid particles pass the valve. The pressure varies smoothly and decreases very rapidly as shown in Fig. 6(c).

At the final stage of valve closure, the passage is almost fully blocked. Shown in Fig. 6(d), the pressure in the region upstream of the valve is high almost everywhere. In fact, the flow velocity is small in this region and the fluid particles suffer adverse pressure gradient. The pressure on the front side of the valve reaches its maximum value. This is somewhat like the water hammer effect. However, observing Fig. 6(e), we find that such an effect reduces its impact very rapidly. On the downstream side, the pressure is almost of the same value everywhere. The variation is insignificant. Nevertheless, the pressure on the tip of the long arm reaches its minimum. It is due to a high velocity. And such a phenomenon deteriorates rapidly which can be observed in Fig. 6(e). At $t = 0.0324\text{sec}$, the minimum pressure keeps decreasing due to micro-jets [15]. Moreover, the low pressure region on the back surface of the valve cover a wider area.

It is interesting to observe that the pressure variation between $t = 0$ and $t = 0.0315\text{sec}$ is much smaller than that between $t = 0.0315\text{sec}$ and $t = 0.0324\text{sec}$. The valve closure induces stronger and stronger effects on the flow development as the time moves on and the flow is more blockaded by the valve. Such a trend leads to serious consequences just a few moments before the channel is fully closed. At $t = 0.0324\text{sec}$, the minimum pressure is reduced to 9.78kpa, a margin value below which the flow cavitation begins to develop. After $t = 0.0324\text{sec}$, the pressure cannot further decrease because it reaches the vapor pressure and cavitation appears.

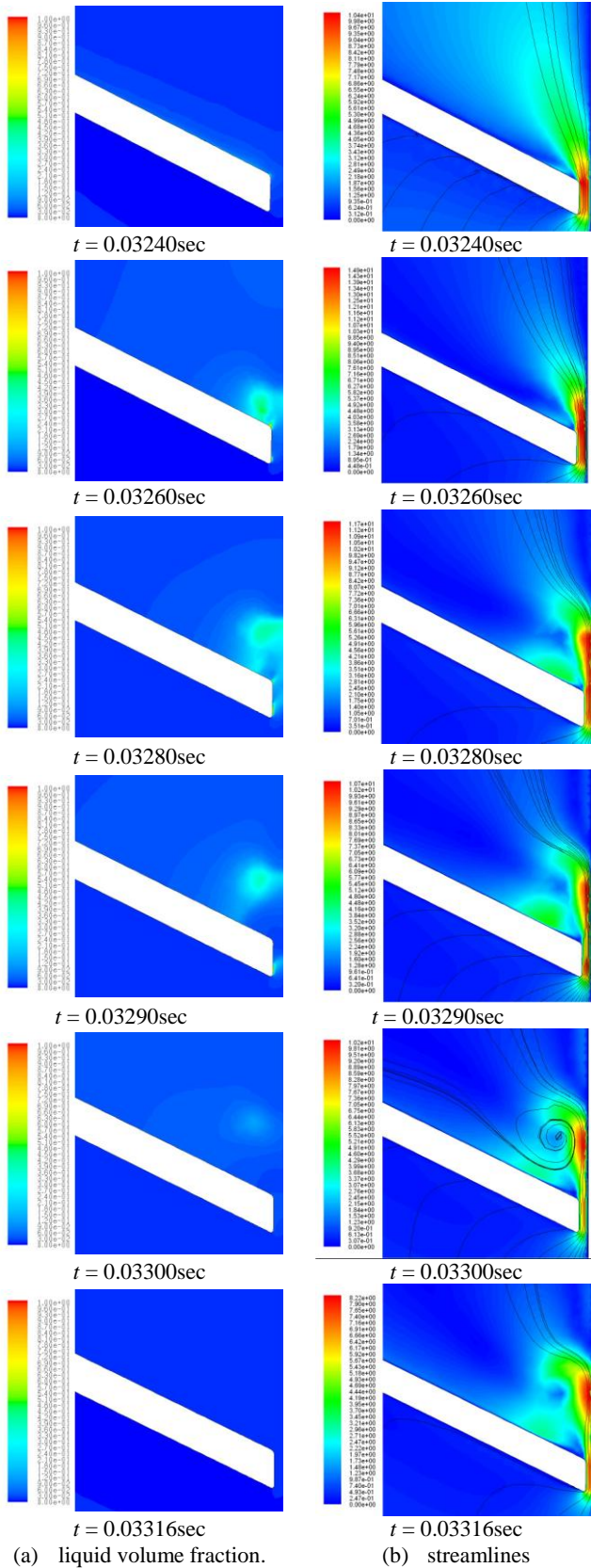


Fig. 7 Variation of the volume fraction of liquid phase and streamline when cavitation takes place.

5. Cavitation

In our study, a region is said to be cavitating when the volume fraction of liquid phase is smaller than 0.5 in that region. The present computational results show that the cavitation develops between $t = 0.03240\text{sec}$ and $t = 0.03300\text{sec}$. It lasts for about $600\mu\text{sec}$, which agrees quite well with the experimental data available in [13]. Unfortunately, the study in [13] did not have the information which described in details how the cavitation developed and decayed.

Fig. 7 shows a series of the variation histories of the volume fraction of liquid phase and streamlines in the region near the valve at several different times when cavitation occurs. In Fig. 7(a), a small cavitation bubble forms near the leading point of the valve tip at $t = 0.0324\text{sec}$. It grows very rapidly and soon becomes a much bigger bubble at $t = 0.0326\text{sec}$. The bubble tends to move into the downstream region. In the meantime, another cavitating bubble forms near the trailing point of the valve tip. At $t = 0.0328\text{sec}$, the cavitating bubble, previously attaching on the leading edge, moves into the downstream region and its size somewhat shrinks. Meanwhile, the development of the cavitating bubble near the trailing edge is not as significant as the one on the leading edge, partly because the clearance between the valve tip and the wall is too small. Soon at $t = 0.0329\text{sec}$ and 0.0330sec , we find that the cavitating bubbles keep decaying. The one in the flow field moves further downstream and its size keeps shrinking. Finally, at $t = 0.03316\text{sec}$, the cavitation can be no more observed in the whole flow field.

The flow is complicated during decay stage of the cavitating bubbles, as shown in Fig. 7(b). At the moment when the first cavitating bubble appears (i.e. at $t = 0.0324\text{sec}$), the vorticity distribution in the flow field is negligible and the streamlines extend straightforwardly from the upstream to the downstream sides. However, at $t = 0.033\text{sec}$ when the cavitating bubble in the downstream flow field probably collapses, a vortex appears. It makes the local flow highly rotational.

Meanwhile, at $t = 0.0324\text{sec}$, a micro-jet begins to appear due to a very high velocity distribution in the narrow clearance between the valve tip and the wall. The jet penetrates into the downstream flow field and induces a strong local shear flow with significant shear stress which could damage blood cells. However, the jet in the clearance decays very rapidly.

Fig. 8 shows the pressure distributions in the region around the valve when cavitation appears in the flow field. Due to the blocking effect, the valve divides the flow field into high- and low-pressure regions, with the high-pressure region being upstream of the valve. In the high pressure region, there appears a water hammer pressure wave which propagates in it with a fading strength. The valve surface suffers from a high pressure impact periodically. Of course, the minimum pressure appears around the tip of the valve when cavitation takes place.

To understand the effect of the pivot location on the development of cavitating flows, we also conducted a series of computations with the pivot located at different places. Table 2 shows the cases we studied. Case-R represents the one we have discussed in details above. In all cases, the total length of the valve keeps identical; however, the lengths of long and short arms of the valve are different. The length ratio of two arms varies from 0.04 to 1.00. Furthermore, the angular velocity also keeps identical for all cases.

Table 2 Seven study cases of valve arm lengths and ratios.

	ℓ_1 (mm)	ℓ_2 (mm)	Ratio
Case-R	1.471	11.445	0.10
Case-2	2.471	10.445	0.25
Case-3	3.471	9.445	0.40
Case-4	4.471	8.445	0.50
Case-5	5.471	7.445	0.75
Case-6	6.471	6.445	1.00

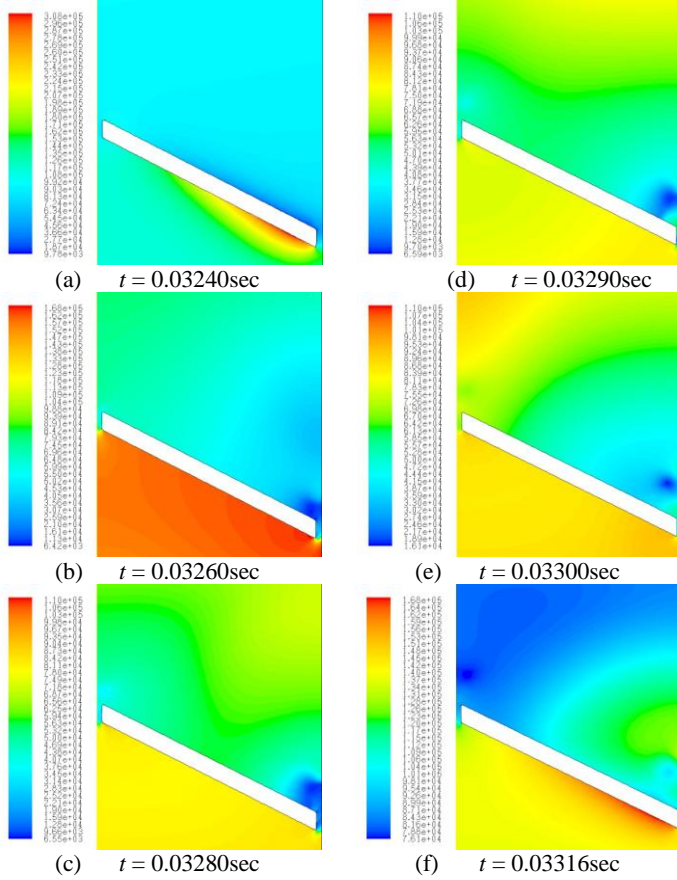


Fig. 8 The pressure distribution around the tip of the valve.

Fig. 9 shows the time variations of the maximum speed found in the flow field for different cases. It is evident that with the pivotal point moving towards the valve center, the maximum speed decreases significantly. This is expected because the tip rotation velocity becomes smaller and, consequently, the induced velocities of fluid particles around the tip smaller, too.

One may expect that cavitation is subsequently improved. Indeed, the minimum pressure distributions in the flow field shown in Fig. 10 exhibit such a trend. The time duration of cavitation drops from about 600 μ sec in Case-R to about 0 sec in Case 6. Nevertheless, it is very interesting to observe that a drop of the minimum pressure takes place almost at the same time for all cases. Since such a drop leads to the occurrence of cavitation, we may also say that cavitation takes place almost at the same time for all cases, regardless of the tip velocity. Furthermore, it is also worth noting that the pressures in Cases 2-5 recover very sharply from the saturated value at different

time. The physical implication of such an abrupt pressure recovery is that the cavitation would disappear suddenly.

Fig. 11 shows the time variation of the maximum volume fraction of gas phase in the flow field for different cases. As expected from the discussion of minimum pressure variation, cavitation occurs at $t = 0.0324$ sec for all cases, except for Case 6 for which cavitation does not take place.

CONCLUSIONS

In the present study, we have computationally investigated the cavitating flow of artificial heart valve during its closure. The $k-\omega$ model was employed for turbulence model. The cavitation physics was captured through the employment of the full cavitation model. We compared our results with those available in [9] and found that both agreed with each other quite well.

To accurately reveal the detailed flow physics, we found that the time step for computations must be as small as 1×10^{-5} sec. It is worth noting that the results of laminar flow computations differ quite significantly from those of turbulent flow computations. (e.g. the maximum speed at $t = 0.0324$ sec is 13.4m/sec for the laminar flow computation and 10.4m/sec for the turbulent flow computation).

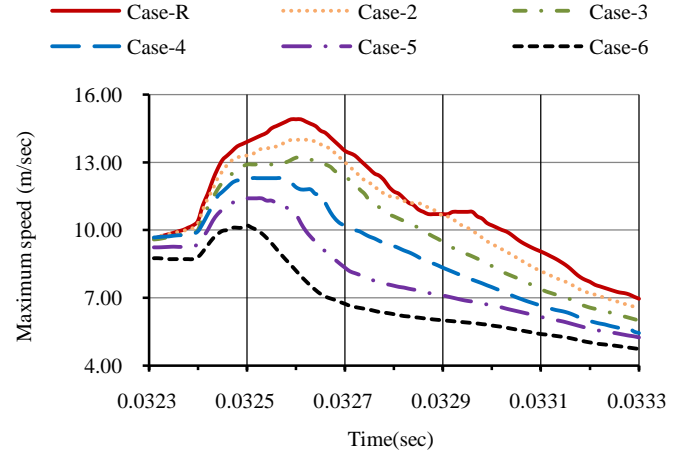


Fig. 9 The time variation of the maximum speed in the flow field for different cases.

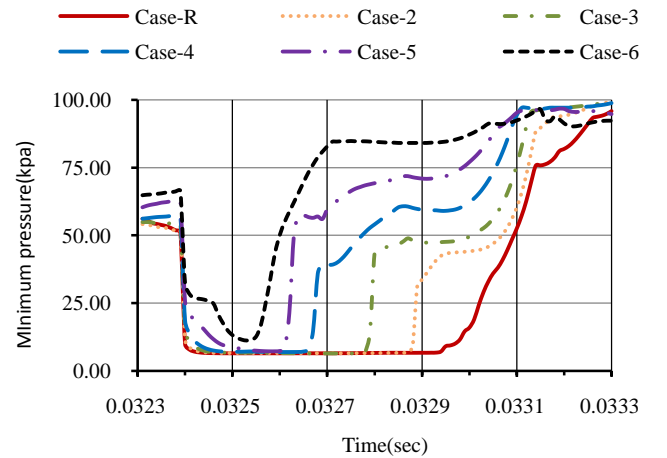


Fig. 10 The time variation of the minimum pressure in the flow field for different cases.

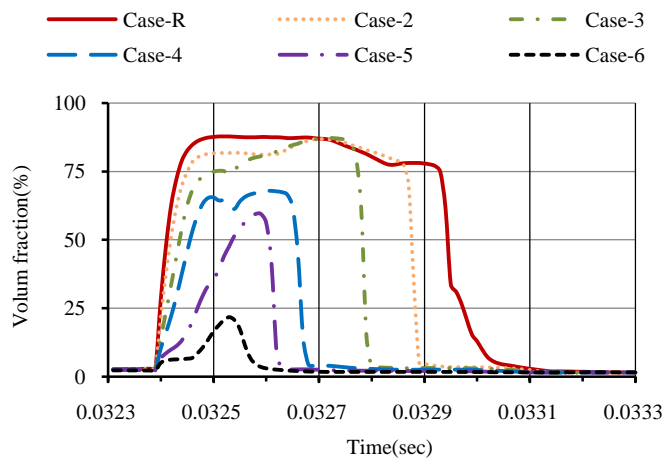


Fig. 11 The time variation of the maximum volume fraction of gas phase in the flow field for different cases.

During the valve closure, a recirculating flow region appears on the back side of the valve in the present study. Such a physical phenomenon results in entrapment of fluid particles in the small region. Fortunately, the time duration for its appearance is not too long.

A strong micro-jet occurs when the channel is almost blocked by the valve. It results in a high shear stress in the downstream flow field and the appearance of cavitation on the tip of the valve. Two cavitation bubbles are found in the present study. The one appearing on the leading edge grows rapidly and finally detaches from the valve. As it moves into the flow field, it decays in size and disappears about 600 μ sec after its appearance. However, its appearance induces vortices in the flow field. The other one appearing on the trailing edge does not grow and keep attached on the valve. This could induce erosion of valve as the cavitation bubble collapses.

Finally, we also carried out a series of computations to study the effect of pivotal position of the valve on the flow development. The position of the pivotal point does have significant influence on the maximum velocity induced in the flow field and the development of cavitation. As the pivotal point is moved to the valve center, the maximum velocity is reduced and cavitation alleviated. However, it is interesting to find that cavitation for all cases occurs at the same time.

REFERENCES

- [1] Hufnagel, C.A., Harvey W.P., The surgical correction of aortic regurgitation-Preliminary report, Bull Georgetown Uni-Med Center, Vol.6#, pp.60-61, 1953
- [2] Klepetko, W., Moritz, A., Mlczech, J., Schurawitzki, H., Domanig, E., and Wolner, E., Leaflet fracture in Edward-Duromedics bi-leaflet valves, Journal of Thorac Cardiovasc Surg, Vol.97#, pp.90-94, 1989.
- [3] Lo, C.-W. and Lu, P.-C., Causes of cavitation phenomena in mechanical heart valves, Department of Water Resources and Environmental Engineering, Tamkang University, 2008.
- [4] Shu, M.C., Leuer, L.H., Armitage, T.L., Schneider, T.E., and Christiansen, D.R., In vitro observations of mechanical

valve cavitation, J. Heart Valve Dis., Supplement 1, pp. 85-92, 1994.

- [5] Zapanta, C.M., Stinebring, D.R., Sneckenberger, D.S., Deutsch, S., Geselowitz, D.B., Tarbell, J.M., Synder, A.J., Rosenberg, G., Weiss, W.J., Pae, W.E., and Pierce, W.S., In vivo observation of cavitation on prosthetic heart valves, ASAIO J., Vol. 42, pp. 550-555, 1996.
- [6] Lee, H., Tatsumi, E., Homma, A., Tsukiya, T., and Taenaka, Y., Mechanism for cavitation of mono-leaflet and bi-leaflet valves in an artificial heart, J. Artificial Organs, Vol. 9, pp.154-160 2006.
- [7] Lee, H., Tsukiya, T., Homma, A., Kamimura, T., Takewa, Y., Tatsumi, E., Taenaka, Y., Takano, H., and Kitamura, S., Observation of cavitation bubbles in mono-leaflet mechanical heart valves, J. Artificial Organs, Vol. 7, pp.121-127 2004.
- [8] Avrahami, I., Rosenfeld, M., Einav, S., Eichler, M., and Reul, H., Can vortices in the flow across mechanical heart valves contribute to cavitation, Med. Biol. Eng. Comput., Vol. 38, pp. 93-97, 2000.
- [9] Lai, Y.G., Chandran, K.B., and Lemmon, J., A numerical simulation of mechanical heart valve closure fluid dynamics, J. Biomech., Vol. 35, pp. 881-892, 2002.
- [10] Singhal, A.K., Athavale, M.M. Li, H., and Jiang, Y., Mathematical basis and validation of the full cavitation model, Journal of Fluids Engineering, Vol. 124, pp.617-624, 2002.
- [11] Patankar, S.V., Numerical Heat Transfer and Fluid Flow, Hemisphere Publishing Corp., Washington, D.C., USA, 1980.
- [12] Fluent-Dynamic Mesh Manuel, Fluent Inc. 2001.
- [13] Lee, H., Akagawa, E., Tatsumi, E., and Taenaka, Y., Characteristics of cavitation intensity in a mechanical heart valve using a pulsatile device: synchronized analysis between visual images and pressure signals, Journal of Artificial Organs, Vol. 11, p.p. 60-66, 2008.
- [14] Johnsen, P., Mechanical heart valve cavitation, Expert Rev. Medical Devices, Vol. 1, pp. 95-104, 2004.
- [15] Lee, H., and Taenaka, Y., Characteristics of mechanical heart valve cavitation in a pneumatic ventricular assist device, Journal of Artificial Organs, Vol. 32, pp.453-460, 2008.

The interaction of ultrasonic bubbles with a tissue layer

D.M. Leppinen*, School of Mathematics,
University of Birmingham

G.A. Curtiss, Numerical Algorithms Group,
Oxford

Q. X. Wang, School of Mathematics,
University of Birmingham

J. R. Blake, School of Mathematics,
University of Birmingham

*D.M.Leppinen@bham.ac.uk

ABSTRACT

This paper examines the dynamics of an initially stable bubble due to ultrasonic forcing by an acoustic wave. A tissue layer is modelled as a density interface acted upon by surface tension to mimic membrane effects. The effect of a rigid backing to the thin tissue layer is investigated. We are interested in Ultrasonic Contrast Agent type bubbles which have immediate biomedical applications such as the delivery of drugs and the instigation of sonoporation. We use an axisymmetric boundary integral technique to model the interaction between a single bubble and the tissue layer. We have identified a new peeling mechanism whereby the re-expansion of a toroidal bubble can peel away tissue from a rigid backing. We explore the problem over a large range of parameters including tissue layer depth, interfacial tension and ultrasonic forcing.

NOMENCLATURE

F : density weighted potential
 f : ultrasound frequency
 G : free space Green's function
 H : vertical location of rigid backing
 h : standoff distance $h = z_c / R_{\max}$
 p : pressure field in liquid
 p_b : bubble pressure
 p_∞ : total pressure at infinity
 p_∞^* : mean far field pressure
 $p_{a\infty}$: amplitude of ultrasonic wave
 (r, z) : cylindrical coordinates
 R_{\max} : maximum possible bubble size
 t : time
 V : bubble volume
 z_c : bubble centroid at $t = 0$
 \mathbf{n} : normal vector
 \mathbf{u}_i : velocity field in layer i
 (\mathbf{b}, \mathbf{c}) : surface points on bubble in layer 1
 (\mathbf{p}, \mathbf{q}) : surface points on density interface

$(\mathbf{x}_0, \mathbf{x})$: surface points for Green's function

Δ_p : pressure scale with $\Delta_p = p_\infty - p_v$

γ : ratio of specific heats

ε : strength parameter with $\varepsilon = p_0 / \Delta_p$

ϕ_i : velocity potential in layer i

σ : surface tension

ρ_i : density in layer i

ρ : density ratio with $\rho = \rho_1 / \rho_2$

1. INTRODUCTION

Cavitation is a dominant feature in a wide range of industrial, environmental and biomedical applications. It can result when the pressure in a volume of liquid falls below its vapour pressure due to hydrodynamic forcing, due to detonation of explosive or the focusing of a laser beam in a liquid, as well as from the interaction of pre-existing bubble nuclei with sonic forcing. Extensive reviews on this subject have been written (see [1-4], amongst others).

This paper deals with sonically driven cavitation in the biomedical context. One such procedure is shockwave lithotripsy. In this a semi-ellipsoidal structure is placed adjacent to a patient, focusing shockwaves generated at the external focus to the focus located inside the body. Removal of kidney and bladder stones via this procedure benefits from the collapse phenomena, with the focusing of the shockwave creating tiny cavities close to the surface of the target object [5]. The side effects of this technique, potentially magnified by unwanted cavitation, can be problematic and can include major vein thrombosis and gastro-intestinal injuries such as colon perforation.

Other medical techniques have been developed using both low and high frequency ultrasound to acoustically activate cavitation during diagnostic procedures. The use of ultrasound contrast agents (UCA) to improve the echogenicity of biological fluids is one such technique. These are encapsulated micron scale gas bubbles with thin shells, which can be easily administered to a patient through injection or ingestion. Examples of such products include protein shelled encapsulated

air UCA's such as Albunex, and modern soft lipid shelled perfluorocarbon encapsulated UCA's such as SonoVue [6-7]. The acoustic signature produced by the compressible UCA's is significantly higher than that of the near incompressible tissues, and provides great improvement in visualisation, particularly in detecting focal liver lesions [8-9].

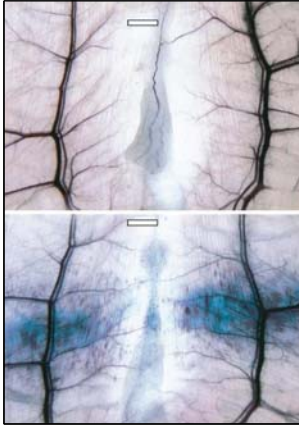


Figure 1. Abdominal mouse muscle and fat after ultrasound exposure using a 2.5MHz transducer at an amplitude of 2.6MPa. The contrast agent Optison was used in the specimen displayed in the lower image. Abundant petechial haemorrhages are visible in the lower sample as red dots and streaks. The white bar represents 1mm.

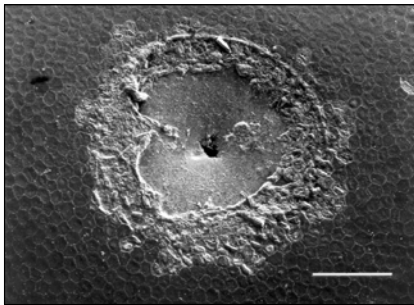


Figure 2. Cavitation damage to a cornea specimen. The white bar represents a distance of 100 micron, whilst the laser generated bubble was formed at a standoff distance of 0.45 maximum bubble radii.

At higher ultrasound amplitudes, UCA's will break down in the acoustic field. This structural failure allows for their potential use as locally targetable drug delivery vesicles [10-11]. Of particular note is the manner in which breakdown occurs, and the damage it can cause to surrounding tissue. An example of the damaging effect caused by such operations can be seen in figure 1, showing samples of mouse abdominal muscle after ultrasound exposure, using a 2.5MHz transducer at an amplitude of 2.6MPa with and without the contrast agent Optison. Petechial haemorrhages are visible in abundance as red dots and streaks in

the agent treated sample, yet there are few, if any, in the untreated case [12].

This seemingly unwanted side affect has recently been pioneered as a local delivery method for large molecules. In particular it can be used to deliver DNA, and hence is being actively researched as a non-viral method for gene transfection [9,13-14]. This process, termed sonoporation, involves the local induction of cavitation dynamics using ultrasound to permeate cell membranes, thereby allowing DNA introduced into the extracellular environment to enter the target cells [13]. The potential benefits of sonoporation over existing transfection techniques are considerable. Viral encapsulation delivery systems suffer from possible toxicological and mutagenic side effects, whilst other encapsulation techniques such as lipid coating, are not locally focusable [14]. Locally targeted non-encapsulation methods also exist, although these have difficulties with implementation. Electroporation for example requires electrodes to be inserted into the target area to induce cell membrane separation, and the direct injection of DNA into cells is naturally restricted to internal applications. Transfection through sonoporation in contrast is easily administered externally, and is readily locally focused. Excessive cavitation caused during the application can however cause significant damage and cell death [15], with the generation of sonopores on the size order of magnitude of a cell [16]. To minimise the amount of cell death, and to determine the mechanisms from which it arises, the fluid dynamics of both the intra and extracellular environments need to be examined. Similarly to help maximise the viable poration of cell membranes, the dynamics associated with the collapse of the UCA's is of critical importance.

The organic environments with which these cavities interact can not in general be viewed simply as rigid boundaries. Aside from the complex topology of the surroundings, the elasticity of the cell membranes and the fluid which they enclose must be taken into consideration. This is evident from recent experiments with initially flat elastic surfaces. These have shown that the elastic modulus of the substrate and the standoff distance of the interacting bubble have drastic effects on the bubble dynamics, both with regards to the translation of the bubble and the jet direction [17-18]. Indeed in some cases horizontal bubble splitting is observed, resulting in very slender high speed jets forming in opposing directions. This potentially has a significant impact on membrane permeation, and explains the significant maximum bubble radius to jet width ratio of 60:1 observed in the experiment shown in figure 2 from Vogel et al. [19] who investigated damage to the cornea due to laser-generated bubbles.

Recent numerical investigations using BIM techniques by Klaseboer and Khoo [20-21] accounting for these interfacial properties have shown qualitative agreement with such experiments. In their simulations, it was assumed that the jump in tangential velocities across the fluid-fluid interface was sufficiently small to be neglected from the dynamic boundary conditions, with marginal discrepancies observed in their test cases. The procedure employed depended upon a geometrical argument valid for a single bubble in an infinite fluid, utilising

the trivial density ratio of 1. This allowed for the interfacial potential in the cavitated fluid to be found independently of the normal velocity of the two fluid interface, by equating various aspects of the coefficient matrices. Elastic effects were also investigated by means of a modification to the pressure in the fluid not containing the cavitation, and hence a modification to the dynamic condition on the liquid-liquid boundary [21]. This showed marked differences to the case where no elasticity is present, allowing for the aforementioned bubble splitting to be observed. Further investigations using this implementation have researched acoustically driven bubble behaviour at sub-atmospheric pressure amplitudes near an interface given realistic biological parameters, demonstrating some of the shapes the bubbles may attain during pre-toroidal motions [22]. As in the experiments near elastic interfaces, these simulations have shown bubble motion and jet direction to both be affected by the properties of the material. Prior to the research contained herein however, toroidal effects have not been investigated in this context.

This paper examines the non-spherical behaviour of ultrasound activated micro bubbles, directly relevant to the new biomedical procedure sonoporation. The influence of a tension laden membrane boundary is investigated using practical density ratios, showing significant deviations in bubble shape from the spherical mode. Moreover the influence of a solid backing to a cell layer is investigated, and has demonstrated new phenomena. These include the peeling of the cell layer by the re-expanding toroidal bubble when the cell layer depth is sufficiently less than the maximum bubble radius, as well as the injection behaviour generated by smaller bubbles under high driving frequencies near thicker layers. It is clearly demonstrated that the jet may cause significant damage to the cell layer, implying that the targeting of cells for transfection using ultrasound activated contrast agents should include the expected non-spherical behaviour after jet impact has occurred. In Section 2 we introduce the mathematical model, with details of the numerical implementation given in Section 3. Our results are presented in Section 4 and overall conclusions are made in Section 5.

2. MATHEMATICAL MODEL

The problem we are considering is sketched in Figure 1 with a layer of fluid of density ρ_1 underlying a layer of fluid of density ρ_2 with $\rho_1 < \rho_2$. The fluid in layer 2 is bounded from above by a rigid boundary. In each layer the fluid is assumed to be inviscid, incompressible and irrotational so that the velocity field can be written as the gradient of a potential with

$$\mathbf{u}_i = \nabla \phi_i \quad (1)$$

for $i = 1, 2$ where

$$\nabla \cdot \mathbf{u}_i = \nabla^2 \phi_i = 0 \quad (2)$$

and

$$\nabla \times \mathbf{u}_i = \mathbf{0}. \quad (3)$$

We consider the case of one bubble located in the lower fluid layer (i.e. on the opposite side of the density interface to the rigid boundary). The bubble is initially spherical with a centroid at a distance z_c below the initially flat interface. Our objective is to examine the interaction of a micron sized bubble with the

density interface and hence gravitational effects can be ignored. We assume axisymmetric cylindrical coordinates (r, z) as indicated. The density interface is initially located at $z = 0$ and the rigid boundary at $z = H$.

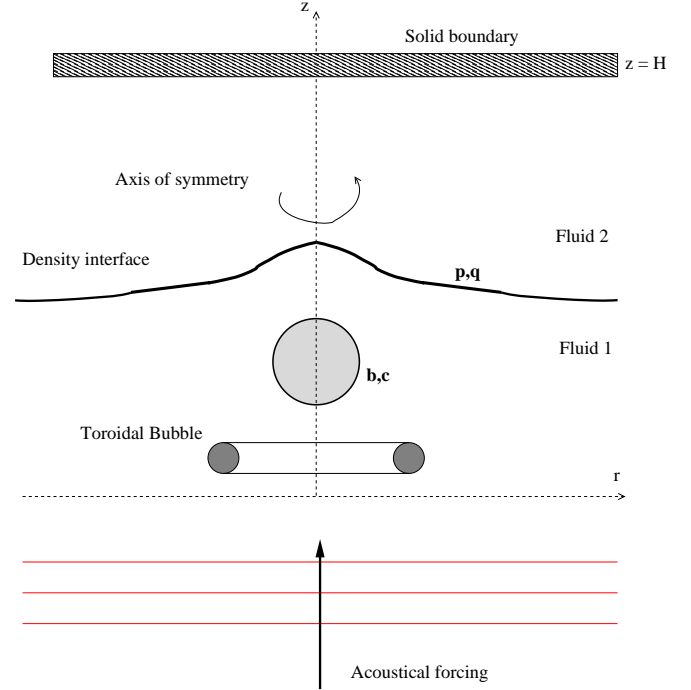


Figure 3. The axisymmetric geometry used to examine the interaction of a bubble with a density interface bounded by a solid boundary.

With the above assumptions Bernoulli's equation is valid everywhere in both exterior fluids which gives

$$\frac{\partial \phi_i}{\partial t} + \frac{|\mathbf{u}_i|^2}{2} + \frac{p}{\rho_i} = \frac{p_\infty}{\rho_i} \quad (4)$$

where t is time, p is pressure and p_∞ is the far field pressure. We assume that the far field pressure can be modeled as

$$p_\infty(z, t) = p_\infty^* + p_{a\infty} \sin(kz - \omega t) \quad (5)$$

Where p_∞^* is the background pressure at infinity, $p_{a\infty}$ is the maximum amplitude of the wave, $k = 2\pi f c^{-1}$ and $\omega = 2\pi f$ are the wave number and the radial frequency given the speed of sound in the liquid c and the frequency of the wave f .

The exterior fluid layers are taken as isothermal. Furthermore it is assumed that no mass or heat transfer will occur across the gas/liquid boundaries. Thus the bubble gases obey an adiabatic law. The pressure inside each bubble is given by

$$p_b = p_v + p_0 \left(\frac{V_0}{V} \right)^\gamma \quad (6)$$

where p_v represents the condensable gas vapour pressure, V, V_0 are the bubble volume and initial reference volume respectively, p_0 is the initial reference pressure for the bubble at reference

volume and γ is the ratio of specific heats of the incondensable gas (taken as 1.4 in this paper).

The pressure of the surrounding liquid at the bubble surface is given by the Young-Laplace condition as

$$p = p_b - \sigma_b \nabla \cdot \mathbf{n}_b \quad (7)$$

where σ_b is the surface tension of the bubble and \mathbf{n}_b is the outward pointing unit normal.

The pressure jump across the density interface is also calculated using the Young-Laplace condition as

$$p = p_b - \sigma_I \nabla \cdot \mathbf{n}_1 \quad (8)$$

where σ_I is the surface tension of the density interface and \mathbf{n}_1 is the unit normal pointing from fluid 1 into fluid 2.

We proceed by nondimensionalising our equations using the following scales: the density of the lower layer, ρ_1 , for density; the difference in the far field pressure and the condensable gas vapour pressure, $\Delta_p = p_\infty - p_v$ for pressure; the maximum radius a bubble would reach in an infinite fluid of density ρ_1 , R_{\max} for length; $R_{\max}(\rho_1 / \Delta_p)^{1/2}$ for time; $(\Delta_p / \rho_1)^{1/2} / R_{\max}$ for potential; $R_{\max} \Delta_p$ for surface tension. Thus along a bubble interface in fluid 1 the Bernoulli equation becomes

$$\frac{\partial \phi_1}{\partial t} + \frac{|\mathbf{u}_1|^2}{2} = 1 - \varepsilon \left(\frac{V_0}{V} \right)^\gamma + \sigma_b \nabla \cdot \mathbf{n}_b \quad (9)$$

where $\varepsilon = p_0 / \Delta_p$ is set equal to 1 for our sonically driven bubbles and all variables are now dimensionless.

Along the density interface we use equations (4) and (7) to obtain

$$\left(\frac{\partial \phi_1}{\partial t} + \frac{|\mathbf{u}_1|^2}{2} \right) - \rho \left(\frac{\partial \phi_2}{\partial t} + \frac{|\mathbf{u}_2|^2}{2} \right) = -\sigma_I \nabla \cdot \mathbf{n}_1. \quad (10)$$

3. NUMERICAL IMPLEMENTATION

Recall from figure 1 that (\mathbf{b}, \mathbf{c}) refer to points on a bubble surface in fluid 1 and (\mathbf{p}, \mathbf{q}) refer to points on the interface between fluids 1 and 2. Our objective is monitor the motion of these surfaces. The substantial derivatives on all surfaces are given by

$$\frac{D}{Dt} = \frac{\partial}{\partial t} + \mathbf{u} \cdot \nabla, \quad (11)$$

where $\mathbf{u} = \mathbf{u}_1$ on the bubble surface in fluid 1 and $\mathbf{u} = (\mathbf{u}_1 + \mathbf{u}_2) / 2$ on the two fluid interface. Particles on the bubble surfaces and the density interface are treated as material points and are advected according to

$$\frac{d\mathbf{b}}{dt} = \mathbf{u}_1, \quad \frac{d\mathbf{p}}{dt} = (\mathbf{u}_1 + \mathbf{u}_2) / 2. \quad (12)$$

For convenience we define

$$F = (\phi_1 + \phi_2)(1 - \rho) + (\phi_1 - \phi_2)(1 + \rho) \quad (13)$$

as the density-weighted potential along the density interface which satisfies the evolution equation

$$\frac{DF}{Dt} = (1 - \rho) \mathbf{u}_1 \cdot \mathbf{u}_2 + 2\sigma_I \nabla \cdot \mathbf{n} \quad (14)$$

Along the bubble interfaces in fluid 1 we have

$$\frac{D\phi_1}{Dt} = \frac{|\mathbf{u}_1|^2}{2} + 1 - \varepsilon \left(\frac{V_0}{V} \right)^\gamma + \sigma_b \nabla \cdot \mathbf{n}_b. \quad (15)$$

Our numerical procedure is as follows. We place a discrete series of nodal points (\mathbf{b}, \mathbf{p}) along the bubble surface in fluid 1 and along the density interface respectively. We then timestep (using a variable order Runge-Kutta scheme) equations (12) to update the surface locations and equations (14)-(15) to update the nodal potentials. The nodal velocities are calculated using $\mathbf{u}_i = \nabla \phi_i$ where we use the boundary integral technique to calculate the normal gradient of the velocity potentials and splining techniques to calculate the tangential derivatives.

In particular in fluid layer 1 we have $\nabla^2 \phi_1 = 0$ in the domain D_1 with boundary ∂D_1 then we can write

$$2\pi\phi_1(\mathbf{x}_0) = \int_{\partial D_1} \left(G(\mathbf{x}_0, \mathbf{x}) \frac{\partial \phi_1(\mathbf{x})}{\partial n} - \phi_1(\mathbf{x}) \frac{\partial G(\mathbf{x}_0, \mathbf{x})}{\partial n} \right) dS \quad (16)$$

where $G(\mathbf{x}_0, \mathbf{x}) = 1/|\mathbf{x}_0 - \mathbf{x}|$ is the free space Green's function and $\frac{\partial G(\mathbf{x}_0, \mathbf{x})}{\partial n}$ is the normal derivative of the Green's function with respect to the outward normal of the fluid domain and \mathbf{x}_0, \mathbf{x} are fixed and variable points on our boundary respectively. In fluid 1 the boundary is the union of the density interface and the bubble surface in fluid 1.

In fluid 2 we account for the presence of the rigid boundary by introducing an image point system with

$$G^2(\mathbf{x}_0, \mathbf{x}) = G(\mathbf{x}_0, \mathbf{x}) + G^{im}(\mathbf{x}_0, \mathbf{x}) \quad (17)$$

where

$$G^{im}(\mathbf{x}_0, \mathbf{x}) = \frac{1}{|\mathbf{x}_0 - (2H\mathbf{k} - \mathbf{x})|}. \quad (18)$$

Thus in fluid we can determine the potential along the fluid-fluid interface by solving

$$2\pi\phi_2(\mathbf{x}_0) = \int_{\partial D_2} \left(G^2(\mathbf{x}_0, \mathbf{x}) \frac{\partial \phi_2(\mathbf{x})}{\partial n} - \phi_2(\mathbf{x}) \frac{\partial G^2(\mathbf{x}_0, \mathbf{x})}{\partial n} \right) dS \quad (19)$$

where the above integral is only evaluated along the fluid-fluid interface.

Note that in both equations (17) and (19) the central portion of the density interface is represented using nodal points. The truncated interface is then extended to infinity using a least squares type approximation as detailed by Curtiss [23] with all integrals evaluated analytically along the infinite extension.

The procedure for discretising and solving the boundary integral equations (17) and (19) are well known and our particular implementation is discussed by Curtiss [23]. We note that we have used the vortex ring method of Lundgren and Mansour [24] to carry our integration into the toroidal bubble regime. Briefly, all quantities of interest along the central portion of the density interface and along the bubble surfaces are represented using quintic splines based upon an arclength formulation. The logarithmic singularities associated with the

boundary integral method are removed analytically and all of the resultant integral are approximated using high-order (typically 20) Gaussian quadrature. In summary, when equations (17) and (19) are discretised along their respective boundaries a system of the form $\mathbf{Ax}^* = \mathbf{b}^*$ is obtained where

$$\mathbf{A} = \begin{bmatrix} G_{bc} & -G_{bq} & \frac{\rho}{1+\rho} DG_{bq} \\ G_{pc} & G_{pq}^{im} & \frac{\rho-1}{\rho+1} DG_{pq} - 2\pi I_{pq} - DG_{pq}^{im} \frac{1}{\rho+1} \\ G_{pc} & -2G_{pq} - G_{pq}^{im} & DG_{pq} + 2\pi \frac{1-\rho}{1+\rho} I_{pq} + DG_{pq}^{im} \frac{1}{\rho+1} \end{bmatrix}$$

$$\mathbf{x}^* = \begin{bmatrix} \frac{\partial \phi_1(b)}{\partial n_1} \\ \frac{\partial \phi_2(p)}{\partial n_1} \\ (\phi_1 + \phi_2)(p) \end{bmatrix} \quad (20)$$

$$\mathbf{b}^* = \begin{bmatrix} 2\pi I_{bc} + DG_{bc} & \frac{-1}{2+2\rho} DG_{bq} & G_{bq} \\ DG_{pc} & \frac{-1}{\rho+1} DG_{pq} - \frac{1}{2+2\rho} DG_{pq}^{im} & G_{pq} \\ DG_{pc} & \frac{2\pi}{1+\rho} I_{pq} + \frac{1}{2+2\rho} DG_{pq}^{im} & G_{pq} \end{bmatrix} \begin{bmatrix} \phi_1(b) \\ \phi_2(p) \\ F(p) \end{bmatrix}$$

where G is used to indicate the discretised Green's function and DG the discretised normal derivative of the Green's function.

The block matrix structure is used to emphasise the bubble/interface and interface/interface contributions to the overall result with reference to the notation introduced in Figure 1. The \mathbf{b}^* is known at any time step and the resultant set of equations can be inverted to determine the normal

velocities $\frac{\partial \phi_1(b)}{\partial n}$, $\frac{\partial \phi_2(p)}{\partial n}$ and the sum $(\phi_1 + \phi_2)(p)$ and hence

to determine the velocity along all interfaces. Thus we can update the surface locations and potentials at each timestep.

4. RESULTS

A particularly interesting feature discovered in this research is the removal of the 'tissue', or 'cell', layer from the substrate through the toroidal action and re-expansion of the cavitation bubble or UCA. This behaviour is referred to here as membrane peeling.

To begin one examines the system governed by $\rho = 1$, under the influence of an acoustic wave with a frequency of 0.2MHz and a maximum amplitude of $p_{a\infty} = 1.4\text{MPa}$. The rigid boundary is located at a dimensional distance of $H = 25\mu\text{m}$ from the two-fluid interface, roughly corresponding to a non-dimensional distance of 0.34 maximum bubble radii. The tension on the interfaces is of low order, and so it will not significantly affect the simulation. The model therefore is very close to the collapse of a bubble in an infinite fluid near to a rigid boundary, albeit in the presence of a membrane with little tension. Figure 4 shows the associated bubble behaviour as the standoff distance is

varied through from $h = 0.5, 0.75, 1, 1.25$ during the later stages of collapse, and the complete simulation of the case $h = 0.75$ is shown in figure 5 for clarity. For the larger standoff distance, one observes the formation and expansion of the bubble toroid, resulting in the forward lobe. This is seen to close at the tip as the bubble continues to evolve. At the closer standoff distances, the toroidal bubble interacts with the wall, resulting in the forward lobes being forced outward radially. Consequently, the bubble jet will not pinch off as rapidly as the bubble re-expands. The fluid-fluid interface in these cases is initially compressed against the wall in the region directly below the mouth of the liquid jet. The re-expansion of the forward toroidal lobes then cuts underneath the interface, lifting the fluid in the second layer away from the substrate. It is this interaction that one describes as membrane peeling.

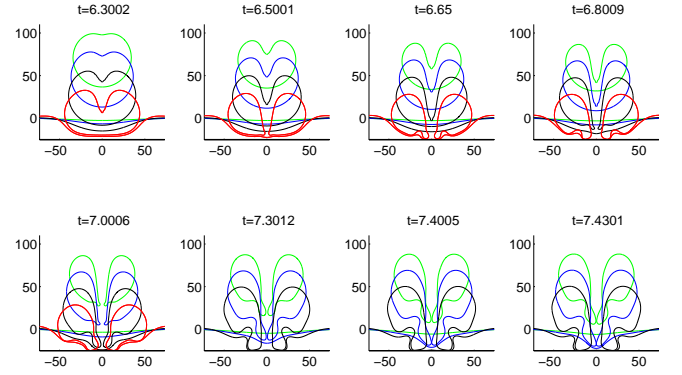


Figure 4. Toroidal bubble formation near a cell layer of depth 25 microns due an acoustic wave with frequency 0.2Mhz and amplitude 1.4Mpa at standoff distance $h=0.5$ (red); 0.75 (black); 1 (blue) 1.25) green.

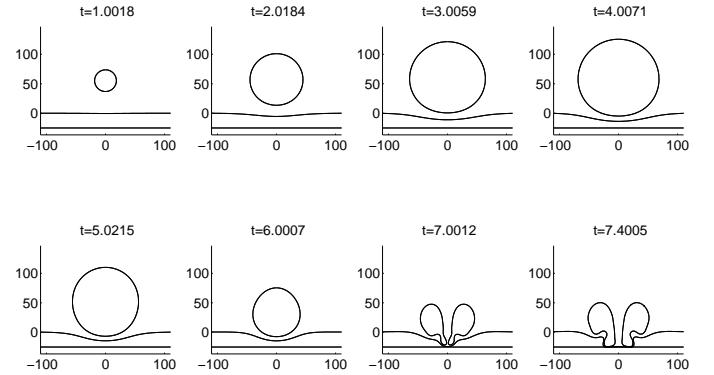


Figure 5. The lifetime of a bubble with $h=0.75$ for the same parameters as in figure 4.

This presents a significant new mechanism for tissue damage. Circumstantial evidence may be visible in the cornea specimen micro-graph in figure 2 created by Vogel [19] where a large area with a radius of approximately 100 microns surrounding the jet impact location has been scraped away.

Previous work has postulated that this is due to the shear stress caused by the high fluid velocity beneath the bubble. This membrane peeling may however provide an additional mechanism, associated with the re-expansion of the toroidal bubble.

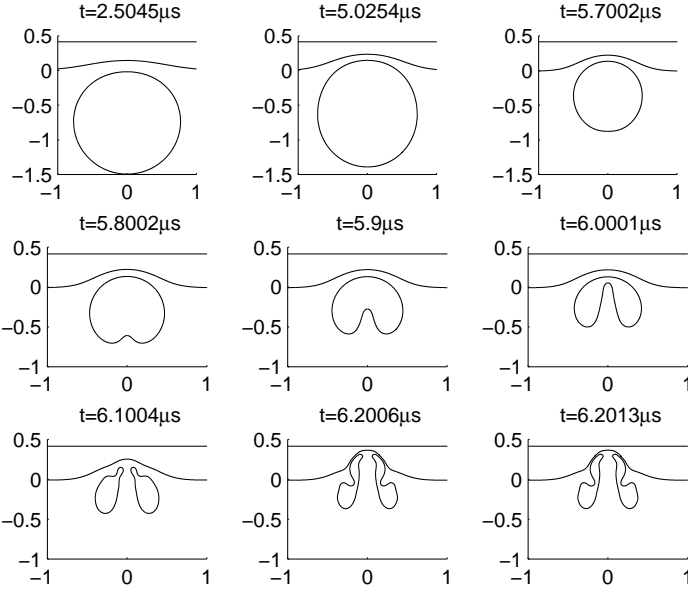


Figure 6. Shapes from the simulation of a bubble driven by an acoustic wave with frequency 0.2MHz and peak pressure 1MPa. The parameters of the flow field are $H=25$ microns, $h=60$ microns. The membrane has zero interfacial tension.

Varying the membrane tension may provide a better approximation to a biological tissue. Importantly, it will show whether the bulk fluid motion is a result of the inclusion of the rigid boundary, or the influence of the membrane. Figures 6 and 7 show simulations using a 0.2MHz acoustic wave with maximum amplitude $p_{a\infty}=1\text{MPa}$ at a standoff distance of 60 microns. The surface tension on the bubble surfaces is $\sigma_b = 0.00165$ to model the effect of a UCA and the membrane tensions are $\sigma_l = 0, 1$ respectively. The backing plate is again located at $H=25$ microns. The shapes in the zero tension case naturally agrees with a single layer of fluid with $h \approx 1.35$, as did the simulation shown in figure 5. The bubble toroid forms as normal, with the advancing jet and lobe forcing the interface against the backing plate.

The inclusion of unit membrane tension significantly inhibits this behaviour. The rebounded interface causes the near boundary side of the interface to flatten in comparison to the rounded shape observed in its absence. The bubble forms a jet directed toward the interface, in contrast to the behaviour of a bubble near a floating membrane with the same tension. As the toroid forms, the circular disturbance is initially forced outwards. The jet forms a wide pit in the tissue layer, and the advancing bubble then slides in along the sides of the pit.

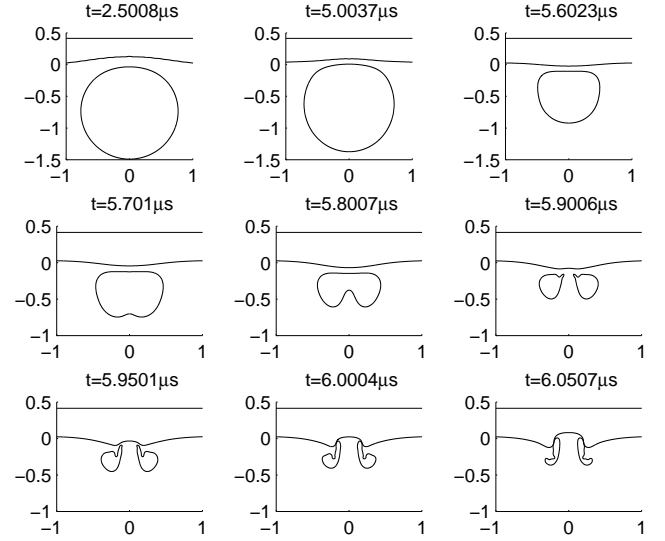


Figure 7. Shapes from the simulation of a bubble driven by an acoustic wave with frequency 0.2MHz and peak pressure 1MPa. The parameters of the flow field are $H=25$ microns, $h = 60$ microns. The membrane has surface tension $\sigma_l = 1$.

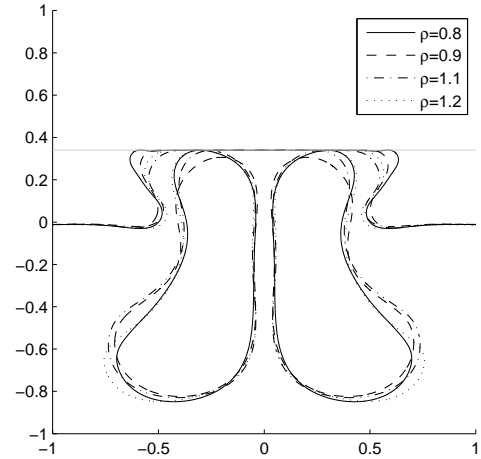


Figure 8. Comparison between bubble and interface shapes as the density ratio is varied near unity under identical acoustical forcing, surface tension and standoff distance.

The results in figures 4 to 7 have all been for $\rho = 1$ which is typically for biomedical applications. Slight variations to the density ratio are presented in figure 8. Here the bubbles were driven by a standing acoustic wave with peak pressure $p_{a\infty} = 1.4\text{MPa}$ and a frequency of 0.2MHz. The cell layer depth is $H = 25$ microns and the standoff distance is approximately 73 microns. The dimensionless bubble surface tension and interfacial tension are $\sigma_b = 0.01$ and $\sigma_l = 1$ respectively. The bubble surface tension acts to inhibit the leading edge of the toroid from rejoining, allowing the simulation to proceed further and hence to increase the calculated peeling effects. This is more representative of a UCA than the case with zero surface tension.

The extent of peeling for density ratios $\rho = 0.8, 0.9, 1.1, 1.2$ is shown in figure 8 for the same time frame. In all cases the under cutting of the cell layer is visible. The bubble shapes show some variation, although all form the same general 'C' shaped structure in the (r,z) plane, with the density ratios furthest from unity showing slightly more peeling. However, this does not appear significant, and so one may conclude that there is little variation in peeling for density ratios close to 1.

In the previous examples, the sub-megahertz frequency allowed the cavity to expand greatly, to a radius much larger than the typical dimensions of a cell. Indeed the peeling observed in figure 8 was over a region with radius approximately 40 microns, four time the size of a typical eukaryotic cell, and would have continued significantly further as the bubble re-expanded. At megahertz frequencies however, the bubble expansion is restricted, and as such it is unclear if the peeling behaviour is still observed, given that surface tension in particular will have a more significant effect. Additionally, with this restricted maximum bubble radius, it is now reasonable to investigate varying the depth of the cell layer, as the maximum radii is on the size order of a eukaryotic cell.

One simulates the dynamics of a UCA characterised by $R_{ref} = 2.5 \mu m$ with dimensional surface tension $\sigma_b = 51$ dyne/cm representative of a Sonovue UCA [7]. The bubble is driven by an ultrasonic wave with a frequency of 1MHz, and a peak pressure 1MPa. This results in a maximum bubble radius of $R_{max} = 13.18 \mu m$. A dimensional standoff distance of $h = 9.881$ microns is chosen, corresponding to the non-dimensional standoff distance $h=0.75$. As was seen previously, the density of the cell layer does not have a significant effect in this phenomena, and as such the density ratio is set to unity. The membrane is loaded with a tension of 0.5dyne/cm.

The first simulation in this regime is shown in figures 9 and 10, illustrating the pre and post toroidal phases of the collapse respectively. The pressure fields in both graphs do not include the pressure wave, and as such show the pressure exerted by the collapsing bubble only. The first frame in the pre-toroidal figure is taken near the maximum radius of the bubble, at the start of the first collapse. Interestingly a stagnation point is clearly visible along the wall in the second fluid layer, as fluid is still being forced outwards by the advancing bubble front, whilst the fluid in the far field is being sucked back in toward the centre. Minimum pressures are around 1MPa, and so the total pressure will be near equilibrium about the bubble, and between the bubble and the wall. As the collapse continues one observes the removal of the stagnation point, as the bubble contracts sucking water inward. The inevitable high pressure region begins to form behind the bubble and will drive the subsequent jet toward the cell layer. The interface itself remains similarly disturbed about the axis, whilst it has recovered toward the initial position elsewhere. As jetting begins, the bubble is rapidly moving toward the wall, and as expected liquid is being forced into the jet at high velocity. Jet tip speeds for this case were of the order of 10 non-dimensional units, corresponding to about 100m/s and thereby subsonic.

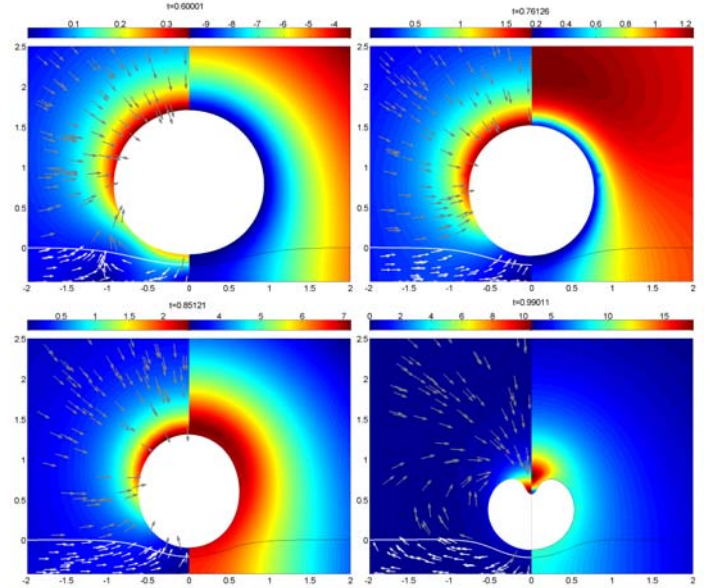


Figure 9 Speed and velocity (left) and pressure (right) during the pre-toroidal stage of a UCA bubble undergoing acoustical forcing.

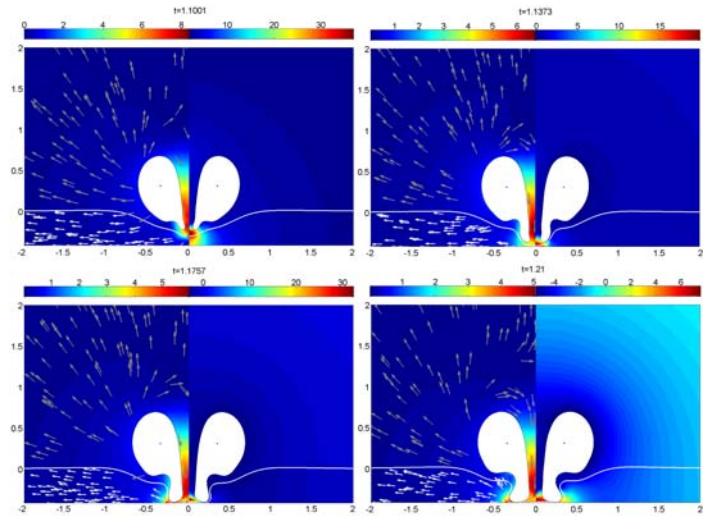


Figure 10. Speed and velocity (left) and pressure (right) during the post-toroidal stage of a UCA bubble undergoing acoustical forcing.

At impact, a peak pressure of approximately 40 atmospheres is exerted in the near vicinity. This acts to accelerate the fluid below the bubble away, and causes a distinct deformation of the interface. The bubble then begins to expand, and a stagnation point forms behind the bubble jet. The jet velocity itself is slowed to around 6 non-dimensional units at the fastest point. The high pressure decreases and becomes more focused at the axis near the wall, forcing fluid sideways. The forward lobe of the toroidal bubble expands downward, until the wall prohibits any further advancement. This acts to prohibit fluid escaping the base of the jet, which re-increases the pressure at the jet tip to approximately 40 atmospheres. The bubble lobes are forced outward along the wall, and begin to undercut the

separated layer. As the process continues, the membrane becomes entrained into the fluid pocket between the two bubble lobes. The pressure drops near the wall as the jet base expands, and a region of higher pressure is observed to form on the other side of the toroidal bubble in the cell layer. Hence the peeling motion is again observed in this parameter regime, albeit at a smaller length scale than above.

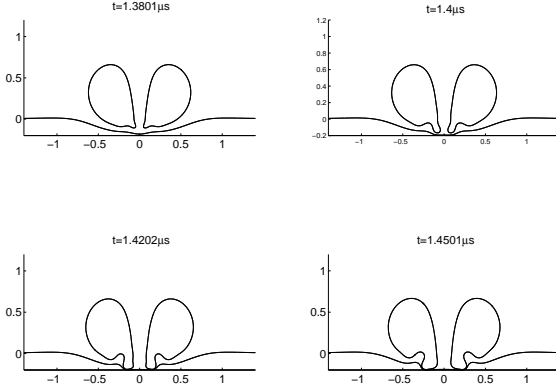


Figure 11. Bubble shapes during the toroidal phase of a UCA bubble collapse near a thin backed liquid layer. The non-dimensional standoff distance from the interface is $h=0.75$, with the depth of the second layer $H=0.2$.

Decreasing the layer depth creates some distinct differences in the peeling behaviour. Figures 11 and 12 contain bubble shapes and pressure and velocity fields for the case $H=0.2$ with time frames beginning just after jet impact and continuing through the development of the forward bubble lobe. Impact occurs at a distance of approximately 0.1 maximum bubble radii from the wall and at half the initial depth of the second layer. Significantly high pressures are observed about the impact site, on the order of 100 atmospheres, and well above the driving pressure. Jet velocities are in excess of 12 non-dimensional units about this region, and are rapidly slowed to below 6 by the near stationary fluid in front of the jet. From the velocity directional arrows, it can be seen that at this point the bubble is already expanding, with fluid being forced outward along the lower layer, with the fluid in the primary layer being driven around the toroid. A stagnation point has formed at approximately 1.2 maximum bubble radii away from the initial level of the interface, although this appears to have little effect on the quantity of liquid entering the bubble jet. As time advances 0.2 non-dimensional units, the pressure about the impact point lessens significantly toward a maximum of 55 atmospheres at the end of the jet next to the rigid boundary. By this time the interface has been forced flat against the wall over a radius of 0.1 maximum bubble radii. The velocity of the jet has decreased somewhat, with the rest of the field still exhibiting the same flow properties. Advancing time by a further 0.1 non-dimensional units presents the beginning of the peeling motion. The advanced ring of the toroidal bubble has been arrested by the presence of the wall and the outer ring jet has begun to form, forcing fluid upward and toward the central jet. The pressure has again dropped, with the maximum pressure occurring inside

the fluid pocket generated by the advancing bubble lobe and the wall.

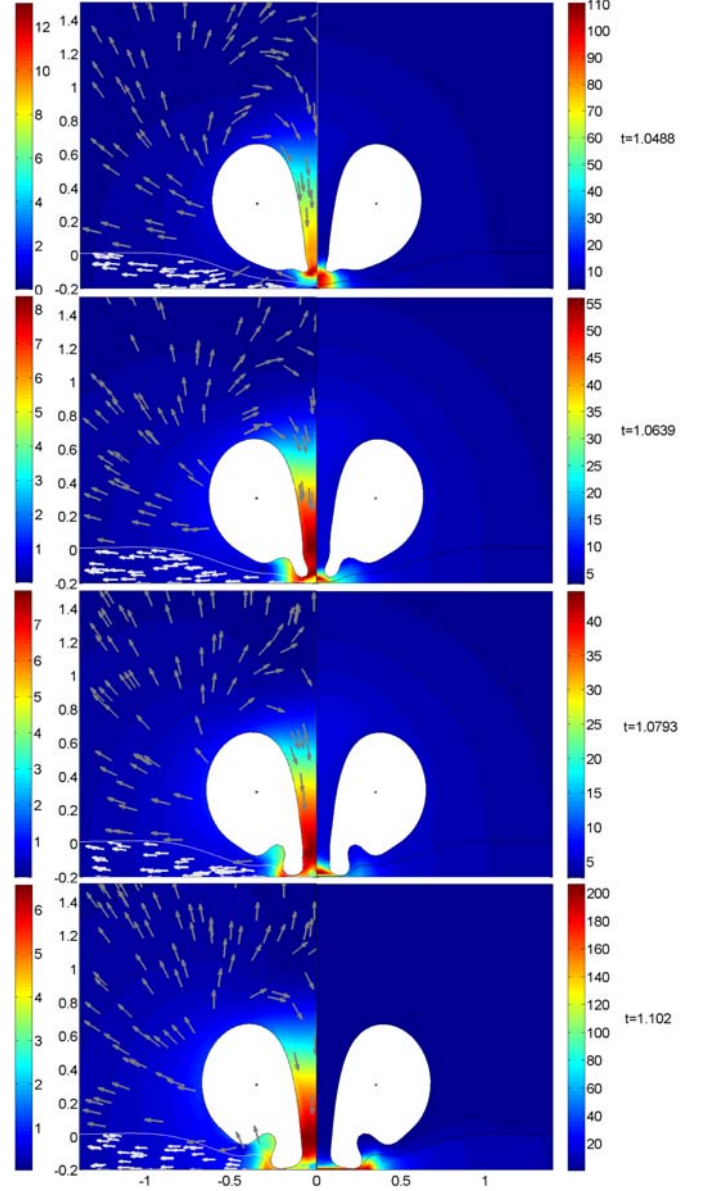


Figure 12. Velocity (left) and pressure field for a post-toroidal UCA bubble near a thin backed layer.

Maximum pressure is now approximately 40 atmospheres, still greatly in excess of the driving amplitude. A region of pressure at about 20 atmospheres has also formed directly below the secondary jet ring. At the end of the simulation, the peeling effect can clearly be seen. The forward lobe has forced the second layer to a near vertical position as the bubble has further re-expanded. The pressure now observed has massively increased toward 160 atmospheres on the outside of the bubble in the lower layer, demonstrating that damage may continue to be caused well after jet impact. The velocity field also illustrates the rolling motion of the secondary ring jet about the toroid, with fluid moving upward toward the bubble centre at a significant velocity. Additionally the stagnation point has also

translated downward to 1 bubble radii above the initial interface position, while the maximum jet velocity has decreased to 6 non-dimensional units. It would be reasonable to assume that significant damage would be caused to a tissue layer in this configuration through inertia alone.

Increasing the cell layer depth generates drastically different behaviour. This is first demonstrated in figures 13 and 14, containing the pre and post jet impact fluid motion and pressure fields for $H=1.6$. At maximum bubble radius the bubble and flow field exhibit the usual characteristics. The shape is roughly spherical, with the near pressure increasing in a uniform radial manner. Toward the wall fluid is naturally advected away from the axis, although the fluid velocity is near zero. As the bubble collapses, the classical higher pressure region above the bubble may be seen, with the fluid moving slightly faster in this region. As the jet forms, one observes the liquid in the primary layer being driven about the bubble and into the jet, with the formation of a stagnation point above the bubble at approximately 2.25 the maximum bubble radius. By this point the bubble centroid has migrated approximately 0.25 maximum bubble radii toward the interface and the wall, whilst the interface has returned toward being flat.

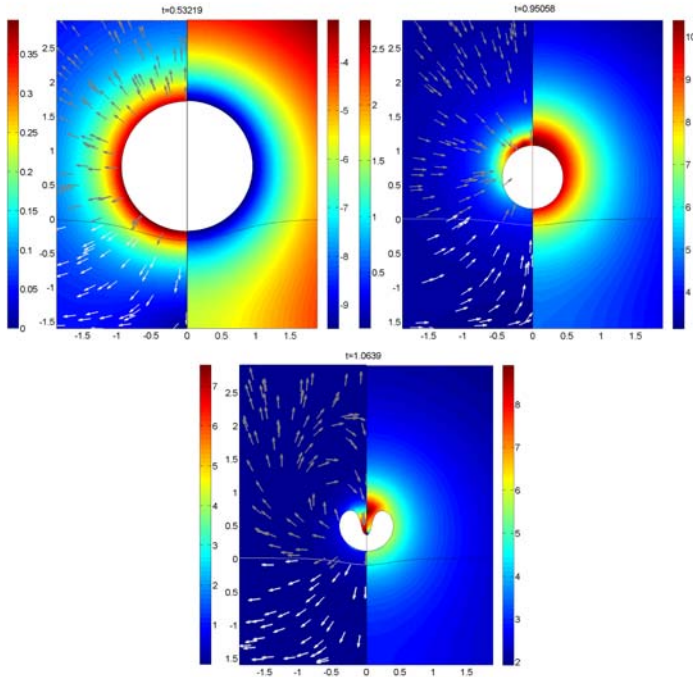


Figure13. Pre-toroidal velocity (left) and pressure fields (right) for a UCA bubble near a thick-backed layer.

The most significant differences occur during the toroidal phase. Firstly, the pressures around the jet impact site are significantly lower. This is due to the presence of a much thinner jet, caused in part by the rapid migration of the over bubble stagnation point to a position of 1, restricting fluid flow into the jet. The increased depth also allows for the pressure to dissipate more before the wall. As this phase continues, the advance of the forward lobe is not arrested by the rigid boundary, and continues to drive the interface downwards as the bubble begins to collapse. The stagnation point also disappears,

allowing more liquid to flow through the toroid. The advance of the bubble is slowed by the fluid flowing upward in the lower layer due to the bubble volume compression, and which is itself deflected around the forward bubble ring. The higher pressure region about the impact site dissipates greatly, almost to equilibrium with the surrounding pressures. As the simulation continues, one observes the fluid in the lower layer flowing around the tip and back in toward the axis, causing the bubble to pinch and the interface to create an overhang. At the rear of the bubble a high pressure ring forms, creating a secondary jetting motion about a torus. Velocities about this jet are comparably high to the initial jet, being of magnitude approximately 8. It is reasonable to expect that this ring jet will cause less damage to the tissue layer than the first, as it is effectively from a smaller bubble. The tissue layer itself has returned to its initial position over $r > 0.6R_{\max}$, a significantly larger area than achieved in the closer collapses. This type of behaviour may be more beneficial for drug injection, as less damage to the cell layer appears to have occurred. Additionally, the forward bubble lobe may break off, with the interface potentially reforming above it, literally injecting a section of the bubble into the tissue. This is very different from the thin layer cases, where the section of bubble connecting the two lobes remained reasonably broad.

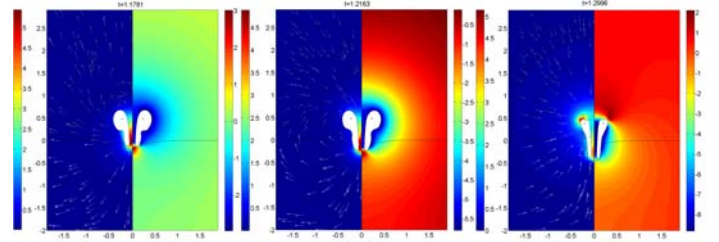


Figure 14. Post-toroidal velocity (left) and pressure fields (right) for a UCA bubble near a thick-backed layer.

5. CONCLUSIONS

This paper has investigated various aspects of acoustically driven bubble behaviour relevant to biomedical applications. It has shown that the tension of a separating membrane can have a profound effect on the bubble dynamics, particularly when the bubble is oscillating at a close standoff distance. Furthermore, it has clearly shown that a rigid backing of the second liquid layer will cause significant differences to the fluid dynamics. This has lead to the discovery of the phenomenon of membrane peeling, a mechanism that depends on the re-expansion of a toroidal bubble to lift the second layer away from the backing plate. The simulations performed here have shown that the use of this as a sonoporation mechanism may be restricted to relatively deep cell layers, and to high frequency, high amplitude ultrasonic agitation.

Support for the peeling mechanism we have identified comes from the experimental results of Tomita et al. [25]. In these experiments, a backed layer of oil based ink with a near uniform depth of 3 microns was submerged in water tank and insonated at 28Khz. Photographic evidence showed that after treatment in this way, the grouping of cavitation filaments

produced sufficiently large bubble clusters to remove the ink from the surface. The authors postulate this was due to both jet impact and a shear flow of water against the solid nickel surface. A photograph taken of the substrate and oil coating after the experiment is shown in figure 15. The results presented here illustrate that a different physical mechanism may be appropriate. As such more detailed experiments should be performed to help identify the dominant phenomenon.

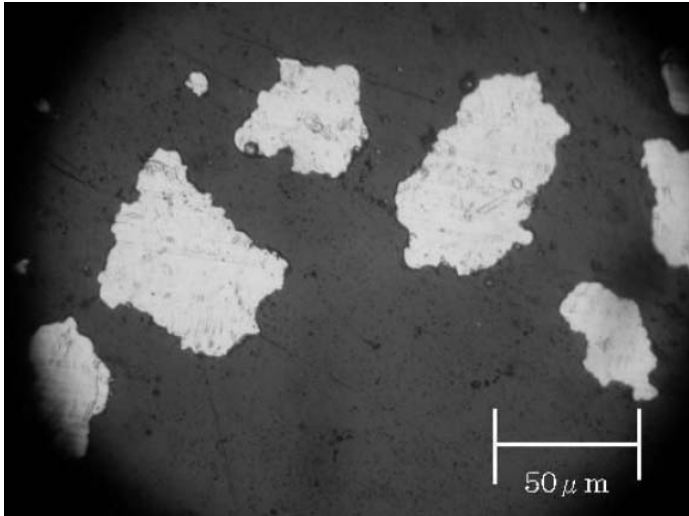


Figure 15. Experimental evidence of the peeling of an inky layer by cavitation bubbles.

ACKNOWLEDGMENTS

Geoffrey Curtiss kindly acknowledges the financial support of EPSRC, The Numerical Algorithms Group and the Smith Institute throughout his PhD Studies.

REFERENCES

- 1 Coussios, C.S. & Roy, A.A. (2008) 'Applications of acoustics and cavitation to noninvasive therapy and drug delivery', *Ann. Rev. Fluid Mech.*, **40**, 395-420.
- 2 Ferrara, K., Pollard, R. & Borben, M. (2007) 'Ultrasound microbubble contrast agents: Fundamentals and application to gene and drug delivery', *Ann. Rev. BioMed. Engng.*, **9**, 415-447.
- 3 Blake, J.R. & Gibson, D.C. (1987) 'Cavitation near boundaries', *Ann. Rev. Fluid Mech.*, **19**, 99-123.
- 4 Arndt, R.E.A. (1981), 'Cavitation in fluid machinery and hydraulic structures', *Ann. Rev. Fluid Mech.*, **13**, 273-326.
- 5 Skolarikos, A., Alivizatos, G. & Rosette, J. (2006) 'Extracorporeal shock wave lithotripsy 25 years later: complications and their prevention', *European Urology*, **50**, 981-990.
- 6 Cosgrove, D.O. (2006) 'Ultrasound contrast agents: An overview', *European Journal of Radiology*, **60**, 324-330.
- 7 Marmottant, S., van der Meer, S., Emmer, W., Versluis, M., de Jong, N., Hilgenfeldt, S. & Lohse, D. (2005) 'A model for large amplitude oscillations of coated bubbles accounting for buckling and rupture', *J. Acoustical Soc. Amer.*, **118**, 3499-3505.
- 8 Church, C. C. (1995) 'The effects of an elastic solid surface layer on the radial pulsations of gas bubbles', *J. Acoustical Soc. Amer.*, **97**, 1510-1521.
- 9 Blomley, M.J.K, Cooke, J.C., Unger, E.C., Monaghan, M.J. & Cosgrove, D.O. (2001) 'Microbubble contrast agents, a new era in ultrasound', *Brit. Med. J.*, **322**, 1222-1225.
- 10 Rapoport, N., Pitt, W.G., Sun, H. & Nelson, J.L. (2003) 'Drug delivery in polymeric micelles: from in vitro to in vivo', *J. Controlled Release*, **91**, 85-95.
- 11 Seemann, S., Hauff, P., Shultz-Mosgau, M., Lehmann, C. & Reska, R. (2002), *Pharm. Res.*, **19**, 250-257.
- 12 Miller, D. & Qudus, J. (2000) 'Diagnostic ultrasound activation of contrast agent gas bodies induces capillary rupture in mice', *Proc. Nat. Acad. Sci U.S.A.*, **97**, 10179-10184.
- 13 Miller, D.L., Bao, S. & Thrall, B. D. (1997) 'Transfection of a reporter plasmid into cultured cells in vitro', *Ultrasound in Med. Biol.*, **23**, 953-959.
- 14 Miller, D. L., Pislaru, S.V. & Greenleaf, J. F. (2002) 'Sonoporation: Mechanical DNA delivery by ultrasonic cavitation', *Somatic Cell and Molecule Genetics*, **27**, 115-134.
- 15 Koike, H. et al. (2005) 'An efficient gene transfer method mediated by ultrasound and microbubbles into the kidney', *J. Gene Med.*, **7**, 106-116.
- 16 Prentice, P. et al. (2005) 'Membrane disruption by optically controlled microbubble cavitation', *Nat. Phys.*, **1**, 107-110.
- 17 Brujan, E. A., Nahen, K.P. & Vogel, A. (2001) 'Dynamics of laser-induced cavitation bubbles near elastic boundaries: Influence of the elastic modulus', *J. Fluid Mech.*, **433**, 283-314.
- 18 Calvisi, M.L., Illoreta, J.I. & Szeri, A.J., (2008) 'Dynamics of bubbles near a rigid surface subjected to a lithotripter shock wave. Part 2. Reflected shock wave intensifies non-spherical cavitation collapse', *J. Fluid Mech.*, **616**, 63-97.
- 19 Vogel, A., et al. (1990) 'Intraocular Nd:YAG laser surgery: Light tissue interaction, damage range and reduction of collateral effects', *J. Quant. Elec.*, **26**, 2240-2260.
- 20 Klaseboer, E. & Khoo, B. C. (2004). 'Boundary integral equations as applied to an oscillating bubble near a fluid-fluid interface', *Comp. Mech.*, **33**, 129-138.
- 21 Klaseboer, E. & Khoo, B. C. (2004). 'An oscillating bubble near an elastic material', *J. Appl. Phys.*, *Comp. Mech.*, **96**, 5808-5818.
- 22 Fong, S. W., et al. (2006) 'Numerical analysis of a gas bubble near biomaterials in an ultrasound field', *Ultrasound Med. Bio.*, **32**, 925-942,
- 23 Curtiss, G. A. (2009) Non-linear, non-spherical bubble dynamics near a two fluid interface. PhD Thesis, University of Birmingham.
- 24 Lundren, T.S. & Mansour, N.N. (1979), 'Vortex ring bubbles', *J. Fluid Mech.*, **224**, 177-195.
- 25 Tomita, Y., Inaba, T., Uchikoshi, R. & Kodam, T. (2008) 'Peeling off effect and damage pit formation by ultrasonic cavitation', *Sci. Bull. Poli*

Numerical Modelling of Ultrasound Contrast Agent Microbubbles Using BE and FE Methods

Michael L. Calvisi*

Department of Mechanical and Aerospace
Engineering, University of Colorado,
Colorado Springs, Colorado, USA

Qianxi Wang

School of Mathematics,
University of Birmingham, Birmingham, UK

Sergey Martynov

Department of Chemical Engineering,
University College London, London, UK

Eleanor Stride

Department of Mechanical Engineering,
University College London, London, UK

*Author to whom correspondence should be addressed. E-mail: mcalvisi@eas.uccs.edu

ABSTRACT

Ultrasound contrast agents – microbubbles stabilized with a shell typically of surfactant or polymer – are emerging as powerful tools for noninvasive therapeutic treatments ranging from drug delivery to tumour destruction. While various models have been developed to describe spherical oscillations of contrast agents, the treatment of nonspherical behaviour has received less attention. However, the nonspherical dynamics of contrast agents – including jet development – are an important mechanism for enhancing, e.g., the uptake of therapeutic material across cell membranes and tissue interfaces and causing tissue ablation. In this paper, the development of two nonspherical models of ultrasound contrast agents based on the well-known Boundary Element and Finite Element methods are described. The methodology used to model the influence of the shell on the contrast agent dynamics is presented along with the results of various simulations. Furthermore, the advantages and disadvantages of each model are discussed.

d_s	Shell thickness
G_s	Shell shear modulus
μ_s	Shell viscosity
σ	Surface tension of liquid
R	Bubble radius (spherical case)
R_0	Initial bubble radius
R_1	Inner bubble radius (for shell of finite thickness)
R_2	Outer bubble radius (for shell of finite thickness)
ϕ	Fluid potential
κ	Mean curvature of bubble surface
κ'	Curvature in axisymmetry plane of bubble
r	Radial coordinate
n_r	Radial component of unit normal vector at bubble surface
ρ	Liquid density
μ_l	Liquid viscosity

NOMENCLATURE

Symbol	Parameter
p_g	Gas pressure
p_{g0}	Initial gas pressure
V	Bubble volume
V_0	Initial bubble volume
α	Polytropic exponent
p_∞	Far-field pressure in the liquid
p_0	Hydrostatic pressure
p_a	Dimensionless acoustic pressure
k	Wave number of acoustic wave
z	Coordinate along wave propagation direction
ω	Angular frequency of acoustic wave
f	Frequency of acoustic wave (Hz)
t	Time
ΔT	Radial pressure difference exerted by shell

1. INTRODUCTION

The primary component of ultrasound contrast agents (UCAs) is encapsulated gas-filled bubbles that are a few micrometres in diameter [1]. When injected into the bloodstream, the high compressibility of these microbubbles, relative to the surrounding blood and other tissue, leads to strong scattering of the incident ultrasound, thereby enhancing blood-tissue contrast in the resulting image. While UCAs have been commercially available since 1991 [2], they have more recently generated interest for use in therapeutic applications, for example, as vehicles for drug delivery and tissue ablation [3]. Several researchers are also investigating the use of UCAs in high-intensity focussed ultrasound (HIFU) [4-5].

In order to effectively utilize UCAs in biomedical applications, it is necessary to understand the interplay between the incident ultrasound and the dynamics of the encapsulated microbubbles. While several theoretical models have been proposed to model UCAs, they have mainly been restricted to

the case of spherical oscillations [6-8]. However, nonspherical oscillations can clearly arise, particularly at large ultrasound amplitudes – due to instability of the spherical mode – and also in the proximity of surfaces, e.g., surrounding tissues [2, 9-13]. The manifestation of nonspherical oscillations has several implications in the context of utilizing UCAs for biomedical applications. First, nonspherical surface modes give rise to frequency components – subharmonics, harmonics and ultraharmonics – that are not at the incident ultrasound frequency. These additional frequency components may contribute to the signal scattered by UCA, which are important for distinguishing the microbubble from the surrounding tissue and thus enhancing contrast.

Second, the oscillation of bubbles near a surface can give rise to high-speed jets [14-15]. In the case of a rigid or semi-rigid surface, these jets form on the distal side of the bubble and are directed toward the surface. If sufficiently violent, such jets can cause localized damage, as evidenced in ship propellers affected by cavitation nucleation on the low pressure side and in silicon wafers subject to ultrasonic cleaning. For the case of a UCA, such a jet may potentially enhance tissue poration or cause mechanical destruction of cells. Such a mechanism may be desired in the case of tumour destruction, for instance, but may be undesirable in cases where tissue integrity must be maintained. In any case, an understanding of the relationship between the incident ultrasound, the mechanical properties of the material encapsulating the UCA, and the ensuing microbubble dynamics are critical to properly utilizing UCAs in any clinical setting.

The complex nature of nonspherical bubble oscillations makes them less amenable to analytical models and invites the application of numerical methods to understanding their dynamics. The purpose of this work is to present two numerical methods that have been developed for modelling the nonspherical dynamics of UCAs. These methods are based on the established Boundary Element Method (BEM) and the Finite Element Method (FEM). Each method offers a particular set of advantages and challenges, and one of the goals of this research is to explore these in the particular context of modelling nonspherical UCAs.

The organization of the paper is described briefly as follows. Section 2 presents the theoretical background underpinning both the BEM and FEM models and the numerical techniques developed for modelling the effect of the shell on the bubble dynamics. In Section 3, the primary results of this work are presented, including various validation cases comparing the BEM results to that of the FEM, along with simulations of encapsulated microbubbles. Also, in Section 3 the challenges and limitations of each model are discussed. Finally, Section 4 summarizes the main conclusions and developments of the paper.

2. MODEL DEVELOPMENT

In this section, we describe the development of the BEM and FEM models for modelling nonspherical UCAs. Due to space limitations, many of the details will be withheld and deferred to articles either currently in print or to be submitted for publication in the future. Here we highlight the key technical

developments that were required to model the nonspherical behaviour of UCAs.

The BEM and FEM are both very well-established numerical methods. While the former method has been used extensively for modelling nonspherical bubbles due to its efficacy in tracking moving interfaces, this is less true for the latter method. However, some of the salient physics of UCA applications – principally the relatively higher viscosity of blood compared to water, and the finite shell thickness – warrant consideration of the use of the FEM. The relative merits of these two methods in modelling UCAs will be discussed later in this section. It is noted that Hsiao et al. [16] have developed a model for thick-shelled UCAs based on coupling a finite volume Navier-Stokes solver to a BEM flow solver; however, the BEM model in this work is restricted solely to modelling UCAs with thin shells.

In both the BEM and the FEM models, it is assumed the bubble wall velocities are much less than the speed of sound and, hence, the surrounding liquid can be regarded as incompressible. The FEM model accounts for the fluid viscosity, whereas the BEM model does not. While both the BEM and the FEM model the UCA shell in different ways, both methods model the interior identically. In each model, the UCA is assumed to be filled with a noncondensable filling gas and diffusion across the UCA surface is regarded as slow relative to the bubble dynamics and, thus, may be neglected. From the ideal gas law, we can assume that the gas pressure inside the UCA obeys a polytropic law, according to

$$p_g = p_{g0} \left(\frac{V_0}{V} \right)^\alpha,$$

where p_g and p_{g0} are the instantaneous and initial gas pressure inside the UCA, respectively, V and V_0 are the instantaneous and initial bubble volumes, respectively, and α is the polytropic coefficient. For isothermal behaviour, $\alpha = 1$, and for adiabatic behaviour, $\alpha = \gamma$, where γ is the ratio of specific heats of the interior gas. Unless otherwise noted, we set $\alpha = 1.67$ for the simulations presented here.

Aside from the differences noted above, there is an important distinction between the two models presented here. The BEM model can simulate fully three-dimensional, asymmetric bubbles and also the interaction of two bubbles, whereas the FEM model is restricted to a single, axisymmetric bubble.

A. BEM Model

The BEM model used for this study is based upon the three-dimensional BEM model developed by Wang [17-18] who extended many of the techniques of Blake et al. [14-15] to fully three-dimensional bubbles, including the case of multiple bubbles interacting obliquely near either a free or a rigid surface. This 3D code has been extensively validated against both existing axisymmetric codes and experiments.

Utilization of the BEM relies on the assumption of potential flow in the fluid surrounding the bubble, which in turn requires that the flow be both incompressible and irrotational. These two

assumptions are reasonably satisfied if the bubble wall velocity does not approach the speed of sound in the liquid and the fluid viscosity is relatively low (i.e., the Reynolds number is much larger than unity). The assumption of potential flow reduces the fluid dynamics problem to the solution of an integral form of the Laplace equation, as discussed in numerous articles on the BEM (see [14-15] and [17-18], for example). Solution of the Laplace equation is required only on the boundaries of the system thereby effectively reducing the dimensionality of the system by one (i.e., a three-dimensional flow field requires solution only on two-dimensional boundaries such as the bubble surface).

To adapt Wang's 3D code to model UCAs, two principal enhancements were incorporated: 1) the simulation of the ultrasound field, and 2) the influence of the encapsulating shell. To simulate the acoustic forcing, the far-field pressure p_∞ was modified to include a sinusoidal term

$$p_\infty(z, t) = p_0 [1 + p_a \sin(kz - \omega t)], \quad (1)$$

where p_0 is the hydrostatic pressure, z is the a coordinate along the propagation direction of the sound wave, t is time, and k and ω are the wave number and angular frequency, respectively, of the acoustic wave. The dimensionless parameter p_a is the ratio of the amplitude of the applied acoustic field to the hydrostatic pressure. For $p_a \leq 1$, the fluid pressure does not experience negative pressures due to the applied acoustic field, whereas for $p_a > 1$ it does. The far-field pressure term shown in equation (1) is then incorporated into the dynamic boundary condition similarly as done by Calvisi et al. [19] for an axisymmetric BEM model.

Modelling the influence of the encapsulating shell is more challenging. First, we follow Hoff's [8] model for a spherical bubble and assume the shell is much thinner than the bubble radius and is comprised of a linear, viscoelastic, incompressible solid that imparts a radial pressure difference ΔT across the surface according to

$$\Delta T = 12 \frac{d_s}{R_0^2} \left(\frac{R_0}{R} \right)^4 [G_s (R - R_0) + \mu_s \dot{R}], \quad (2)$$

where R and R_0 are the instantaneous and initial bubble radii, respectively, d_s is the shell thickness, and G_s and μ_s are the shear modulus and shear viscosity of the shell, respectively. The overdot denotes differentiation with respect to time. In deriving the above expression for ΔT , it is assumed that the shell thickness is much less than the bubble radius ($d_s \ll R$) and is thus neglected.

To adapt the Hoff model to nonspherical bubbles, we treat ΔT as a local quantity that varies along the bubble surface and replace the radius R with the inverse of the local mean curvature, κ , i.e., we assume $R = 1/\kappa$. The viscous shell term is not considered in the BEM model at present, but will be incorporated into the model in future studies. To incorporate the influence of ΔT on the bubble dynamics, we include it in the dynamic boundary condition, along with the far-field pressure term in (1), which yields

$$\frac{D\phi}{Dt} = \frac{1}{2} |\nabla \phi|^2 - \frac{p_g}{p_0} + \frac{p_\infty(t)}{p_0} + \frac{\Delta T}{p_0}, \quad (3)$$

where ϕ is the dimensionless fluid potential and t here is the dimensionless time. Equation (3) incorporates the essential physics of the problem. At a given time step, after numerical solution of ϕ at each node on the bubble surface (see [17-18] for details), the remaining quantities on the right-hand side of (3) are evaluated and ϕ is updated using a finite difference approximation of $D\phi/Dt$ for a time step Δt . Note that (3) is a local equation and, in general, varies at every node along the bubble surface.

In order to evaluate ΔT per (2), it is necessary to calculate the local mean curvature κ at each node of a two-dimensional, asymmetric bubble surface. The technique used here to calculate κ is similar to that of Zinchenko et al. [20] who applied this method to deformable drops. We assume the surface in the immediate neighbourhood of an individual node is smooth and locally parabolic. A normal vector is estimated for the node of interest by averaging the normal vectors of the nearest surrounding faces. A quadratic function is then used to describe the position of the neighbouring nodes relative to a Cartesian coordinate system with origin at the node of interest. The coefficients of the quadratic function are determined by a least-squares fit (as the system is generally overdetermined depending on the number of surrounding nodes), and these coefficients are then used to recompute the local normal. The procedure is then repeated until the normal vector converges, and the final coefficient values of the quadratic function are then used to compute the mean curvature at the particular node of interest. This method is very robust and convergence typically happens within only a few iterations.

B. FEM Model

For numerical solution of the set of equations governing the viscous liquid motion surrounding the bubble and deformations of the bubble encapsulating shell, a Finite Element Method (FEM) is applied using COMSOL Multiphysics 3.5 (COMSOL AB, Palo Alto, CA, USA). For this purpose, the solution domain is covered by a triangular non-uniform mesh with higher resolution applied in the domain covering the bubble encapsulating shell and in the liquid regions near the structural interfaces. Deformations of the bubble shell are described using a moving mesh Arbitrary Lagrangian-Eulerian (ALE) algorithm. The ALE method smoothly deforms the mesh in the liquid domain by solving the Laplace equation for the mesh displacements. In order to suppress the non-physical pressure oscillations in the solution of the Navier-Stokes equations, second-order elements for the velocity components and linear elements for the pressure are used. When taking into account the surface tension effect at the bubble surface, the local mean curvature of the surface κ was defined as:

$$\kappa = \frac{1}{2} \left(\kappa' + \frac{n_r}{r} \right)$$

where n_r is the radial component of the unit normal vector at the bubble surface, r is the local radial coordinate of the bubble surface, and κ' is the local curvature in the r - z plane defined as:

$$\kappa' = \frac{d^2 r}{dz^2} / \left[1 + \left(\frac{dr}{dz} \right)^2 \right]^{3/2}$$

The curvature κ' was calculated numerically using the finite-difference approximations for dr/dz and $d^2 r/dz^2$ obtained on 120 points located on the bubble interface. It was found that doubling the number of discretisation points did not noticeably alter the calculated shape and the mean radius of the bubble. In the liquid domain, the maximum mesh size was set [~ 0.25 of the shell thickness; ~ 0.05 of the bubble diameter] to minimise the effect of the grid size on the numerical solution. For the time integration, an implicit backward-differencing second-order method was used. The time step integration was completed when the desired level of accuracy (0.1%) was achieved for the flow variables. The numerical model developed has previously been validated as described in the authors' previous work [13].

C. Surface Tension

Per Hoff [7], it is assumed here that with an encapsulating shell, surface tension is negligible. However, the influence of surface tension, either with or without a shell, can be easily incorporated into either the BEM or the FEM model by utilizing the mean surface curvature algorithms and computing the pressure difference across the bubble surface induced by surface tension according to

$$\Delta p = 2\sigma\kappa,$$

where σ is the surface tension of the liquid.

D. Modified Rayleigh-Plesset Equation

To validate the numerical results generated by the BEM and FEM models for the restricted case of spherical oscillations, the results were compared to a modified Rayleigh-Plesset equation used by Hoff [7] that accounts for the elastic and viscous effects of the shell. Using the present notation, this equation is given by

$$\begin{aligned} \rho \left(R_2 \ddot{R}_2 + \frac{3}{2} \dot{R}_2^2 \right) = & p_{g0} \left(\frac{R_{10}}{R} \right)^{3\gamma} - p_\infty(t) - 4\mu_l \frac{\dot{R}_2}{R_2} \\ & - 12\mu_s \frac{d_s R_{10}^2}{R_2^3} \frac{\dot{R}_1}{R_1} - 12G_s \frac{d_s R_{10}^2}{R_2^3} \left(1 - \frac{R_{10}}{R_1} \right), \end{aligned}$$

where R_1 and R_2 refer to the inner and outer radii of the bubble, respectively, and the subscript 0 refers to the initial state. Also, ρ is the liquid density and μ_l is the liquid viscosity. Note that the term for the time derivative of the liquid pressure, p_L , is neglected in the above equation, as it was derived assuming an

incompressible liquid. Note that in the case of the BEM model, the shell is assumed to be infinitesimally thin, thus, $R = R_1 = R_2$.

3. RESULTS & DISCUSSION

To validate the BEM and FEM models, a series of test cases were simulated and the results of each model compared. The parameters of each test case were chosen to correspond to typical UCA applications and also to verify various aspects of the bubble behaviour. The tests were divided into uncoated and coated cases and the bubble was always assumed to be spherical and in equilibrium with the surrounding fluid at the start of the simulation. In all cases, the agreement between the BEM and FEM models is good, and, for the case of spherical oscillations, agreement with the Rayleigh-Plesset equation is also good.

A. Uncoated Microbubbles

A series of cases were undertaken without a bubble coating to isolate the bubble dynamics due to the fluid inertia and the acoustic forcing from that of the encapsulating shell. The first case is for a spherical bubble with $R_0 = 4.5 \mu\text{m}$ forced with a uniform standing wave of frequency $f = \omega/2\pi = 300 \text{ kHz}$ and $p_a = 1.0$. The bubble remains spherical throughout the oscillation due to the uniformity of the acoustic field. The results of the BEM and FEM models are shown in Figure 1 along with the results of inviscid and viscous versions of the Rayleigh-Plesset equation (without a shell). The agreement is very good among all the curves, although the amplitude predicted by the BEM model is slightly higher due to the absence of viscosity, as expected.

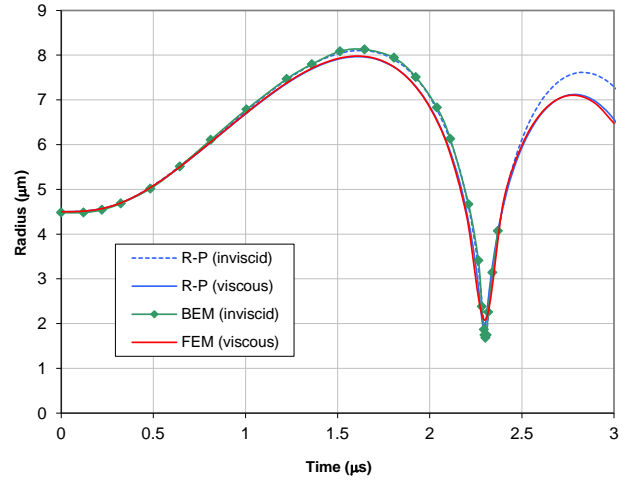


Figure 1: Radius vs. time of a spherical uncoated bubble due to uniform acoustic forcing ($R_0 = 4.5 \mu\text{m}$, $f = 300 \text{ kHz}$, $p_a = 1.0$).

The second case examined was that of a spherical cavitation bubble with surface tension. Here, the acoustic forcing is absent and an initially quiescent bubble is set in motion due to an initial overpressure of the interior gas. One purpose of this case is to test the accuracy of the surface curvature calculation algorithms presented in Section 2. The results of these simulations are shown in Figure 2 for the case of $R_0 = 4.5 \mu\text{m}$, $p_{g0} = 20 p_0$, and σ

$= 0.073 \text{ N/m}$. As with Figure 1, the agreement between the BEM and FEM models with the respective inviscid and viscous versions of the Rayleigh-Plesset equation is good. The lower amplitude of the FEM solution becomes more evident in the second oscillation, due to the cumulative damping effect of viscosity. Some deviation between the BEM solution and the inviscid Rayleigh-Plesset solution is seen during the second collapse due to the accumulation of numerical errors. For the BEM solution, the values of the computed curvature were compared to the expected value of $\kappa = 1/R$, and some discrepancies developed during this part of the solution.

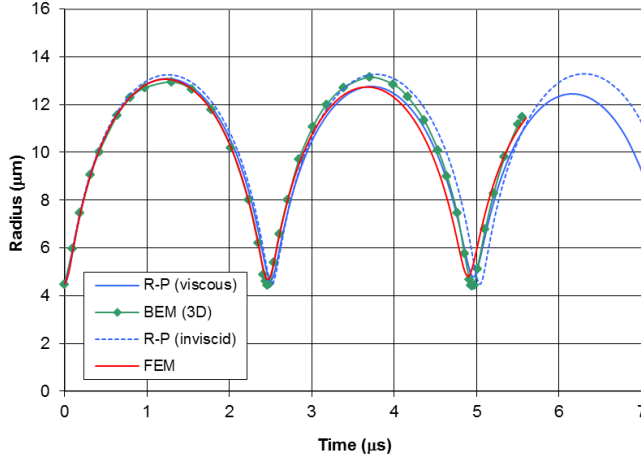


Figure 2: Radius vs. time of a spherical uncoated cavitation bubble ($R_0 = 4.5 \text{ } \mu\text{m}$, $p_a = 0.0$, $p_{g0} = 20p_0$, $\sigma = 0.073 \text{ N/m}$).

The last uncoated case presented here is for a nonspherical bubble that is driven by an acoustic wave near a rigid boundary. The specific parameters were chosen here to emulate a particular simulation shown in Sato et al. [21] who also used the BEM to simulate the nonspherical behaviour of bubbles. The acoustic wave is uniform but the presence of the nearby rigid boundary causes the initially spherical bubble to deform nonspherically. The results of the BEM and FEM simulations are shown in Figure 3 and plotted against those of Sato et al. [21] for the case of $R_0 = 3.0 \text{ } \mu\text{m}$, $f = 547.2 \text{ kHz}$ (half the bubble natural frequency), $p_a = 0.8$, $\alpha = 1.4$, $\sigma = 0$, and an initial standoff distance of the bubble center from the rigid surface of $2R_0$. Note that as the bubble is nonspherical, the “effective” radius R_{eff} is plotted on the vertical axis, which can be determined from the volume by $R_{\text{eff}} = (3V/4\pi)^{1/3}$. (Note that the curves in Figure 3 are made dimensionless by the radius scale, $R_0 = 3.0 \text{ } \mu\text{m}$ and the time scale, $R_0(\rho/p_0)^{1/2} = 0.298 \text{ } \mu\text{s}$.)

Plots of the FEM solution for two different liquid viscosities are shown ($\mu_l = 0.001 \text{ Pa-s}$ and $\mu_l = 0.0001 \text{ Pa-s}$). There is very close agreement between the BEM results and those of Sato et al. [21]. The FEM solution also agrees well with both the BEM and the Sato et al. solutions except that the amplitude of the oscillation is slightly reduced. As the viscosity is reduced from $\mu_l = 0.001 \text{ Pa-s}$ and $\mu_l = 0.0001 \text{ Pa-s}$, the FEM solution approaches that of the BEM, indicating that the discrepancy between the two solutions is due, at least in part, to the presence

of viscosity in the FEM model. Furthermore, the nonspherical shapes predicted by both the BEM and FEM models match closely those of Sato et al. [21].

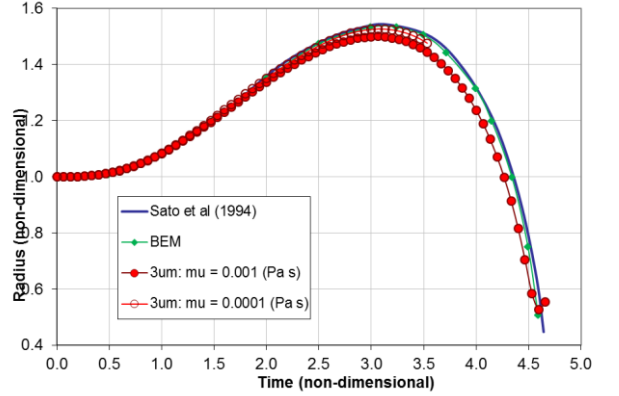


Figure 3: Dimensionless effective radius vs. time of an uncoated, forced nonspherical bubble near a rigid wall ($R_0 = 3.0 \text{ } \mu\text{m}$, $f = 547.2 \text{ kHz}$, $p_a = 0.8$, $\alpha = 1.4$, $\sigma = 0$). The initial standoff distance between the bubble center and the rigid boundary is $2R_0$.

B. Coated Microbubbles

After having gained confidence in the capabilities of the BEM and FEM models through the previous series of tests, the influence of the encapsulating shell was incorporated into the respective models using the techniques described in Section 2.

In Figure 4 is shown the dimensionless volume vs. time predicted by the BEM model for a spherical coated bubble ($R_0 = 4.5 \text{ } \mu\text{m}$) forced at frequency $f = 300 \text{ kHz}$ and $p_a = 1.0$. The results are compared to that of the modified Rayleigh-Plesset equation assuming an infinitesimally thin shell. The top pair of lines are for a bubble without a shell, whereas the bottom pair of lines are for a shelled bubble with $d_s = 15 \text{ nm}$, $G_s = 10 \text{ MPa}$, and $\mu_s = 0$. (Note that in Figure 4 the volume scale is $(R_0)^3 = (4.5 \text{ } \mu\text{m})^3$ and the time scale is $R_0(\rho/p_0)^{1/2} = 0.447 \text{ } \mu\text{s}$.) The stiffening effect of the shell is evident and reduces both the amplitude and period of the bubble oscillation. Furthermore, the agreement between the BEM model and the Rayleigh-Plesset equation is very good, suggesting the BEM model is adequately modelling the influence of the shell.

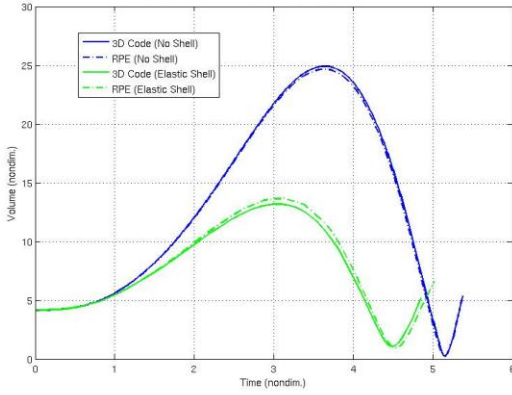


Figure 4: Dimensionless volume vs. time for a spherical coated bubble oscillation comparing BEM model (“3D”) and modified Rayleigh-Plesset (“RPE”) solutions ($R_0 = 4.5 \mu\text{m}$, $f = 300 \text{ kHz}$, $p_a = 1.0$, $d_s = 15 \text{ nm}$, and $G_s = 10 \text{ MPa}$).

The last results presented here are from the FEM model for a coated spherical bubble. These results are shown in Figure 5 for the following set of parameters: $R_0 = 3.0 \mu\text{m}$, $f = 4.6 \text{ MHz}$, $p_a = 0.1$, $d_s = 50 \text{ nm}$, $G_s = 8 \text{ MPa}$, and $\alpha = 1.0$. Note that a relatively small value of the acoustic forcing is used, as the shell is sensitive to buckling at higher values. The agreement of the FEM and modified Rayleigh-Plesset equation is very good, although some disagreement is evident after multiple oscillations, probably due to accumulation of numerical errors.

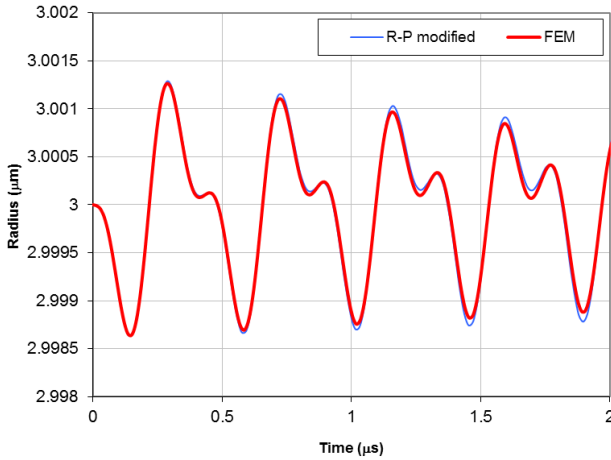


Figure 5: Radius vs. time of a spherical coated bubble predicted by the FEM model and the modified Rayleigh-Plesset equation ($R_0 = 3.0 \mu\text{m}$, $f = 4.6 \text{ MHz}$, $p_a = 0.1$, $d_s = 50 \text{ nm}$, $G_s = 8 \text{ MPa}$, and $\alpha = 1.0$).

C. BEM vs. FEM Comparison

As discussed previously, the BEM and FEM are very different numerical techniques that require different assumptions about the surrounding liquid and model the shell in different

ways. Furthermore, each method has its own particular set of advantages and disadvantages. Generally speaking, the BEM is better able to resolve highly deformed geometries such as thin jets, and is computationally less intensive than the FEM. However, the BEM model presented here is based on potential flow, which restricts its use to cases where the viscosity of the surrounding fluid is negligible. For rapid collapses in water, this assumption holds well, but in blood in clinical applications, this assumption is less certain. The present study confirms that the BEM, as an inviscid model, generally overpredicts the amplitude of oscillation of the UCA bubble.

The FEM model has the distinct advantages of being able to account for the viscosity of the surrounding fluid as well as the finite thickness of the shell encapsulating the UCA. However, its practical application is not straightforward when the shell, as an elastic structure, is prone to buckle. In this case, the shell deformations can induce rapid fluid motion, the accurate modelling of which requires high mesh resolution. The BEM is not prone to buckling due to the assumption of an infinitesimal shell, but numerical errors can accumulate over multiple oscillations as seen in Figure 2. Such errors tend to manifest as spurious roughness of the mesh surface and, while smoothing methods can be applied to minimise this effect, the overuse of such methods can incur errors themselves. Thus, smoothing should only be applied as often as necessary, and no more.

The present comparative study of BEM and FEM models is performed for conditions when the bubble keeps its integrity, i.e. does not undergo breakup as a result of development of any kind of instability. The latter phenomenon, although of a great practical importance, is very difficult to model, as it requires significant remeshing during the computations that can introduce large error in the solution.

A useful advantage of the present BEM model over the FEM model is the ability to simulate fully three-dimensional bubble deformations as well as the interaction of two nearby bubbles. While this is possible to build into the FEM model, it is more computationally expensive. Three-dimensional effects can become manifest, for example, if the incident ultrasound wave is at an oblique angle to a nearby surface, causing the bubble to deform in an asymmetric manner. Furthermore, the influence of nearby bubbles due to the secondary Bjerknes force may have a strong effect on the dynamics if the spacing between neighbouring UCAs is relatively small.

4. CONCLUSIONS

This paper describes the development of two numerical models, based on the well-known BEM and FEM, for modelling the nonspherical oscillations of UCAs. Both models incorporate the effect of the encapsulating shell on the dynamics of the microbubble along with the influence of ultrasound. Each model has been extensively validated against the Rayleigh-Plesset equation for the restricted case of spherical oscillations and shows very good agreement, both with and without a shell. In addition, both the BEM and FEM models show good agreement with each other for the case of nonspherical oscillations without a shell. The absence of viscosity in the BEM model, however, causes it to overpredict the amplitude of bubble oscillation. This set of multiple validations provides confidence in using the BEM and FEM models described here for further studies,

currently in progress, to model the nonspherical dynamics of UCAs.

ACKNOWLEDGMENTS

MLC would like to acknowledge Professor John R. Blake and the School of Mathematics at the University of Birmingham for generously supporting this research during his post-doctoral appointment. SM and ES would like to acknowledge support from the EPSRC (grant EP/E029310/1) and collaboration with Prof. Gail ter Haar at the Inst. Cancer Research on related experimental work.

REFERENCES

- [1] E. Stride and N. Saffari, "Microbubble ultrasound contrast agents: A review," *Proc. Inst. Mech. Eng., Part H: J. Eng. Med.* **217**, 429-447 (2003).
- [2] N. de Jong, M. Emmer, A. van Wamel and M. Versluis, "Ultrasonic characterization of ultrasound contrast agents," *Med. Biol. Eng. Comput.* **47**, 861-873 (2009).
- [3] C. C. Coussios and R. A. Roy, "Applications of acoustics and cavitation to noninvasive therapy and drug delivery," *Ann. Rev. Fluid Mech.* **40**, 395-420 (2008).
- [4] J. E. Kennedy, F. Wu, G. R. ter Haar, F. V. Gleeson, R. R. Phillips, M. R. Middleton and D. Cranston, "High-intensity focused ultrasound for the treatment of liver tumours," *Ultrasonics* **42**, 931-935 (2004).
- [5] V. Zderic, A. A. Brayman, S. R. Sharar, L. A. Crum and S. Vaezy, "Microbubble-enhanced hemorrhage control using high intensity focused ultrasound," *Ultrasonics* **45**, 113-120 (2006).
- [6] C. C. Church, "The effects of an elastic solid surface layer on the radial pulsations of gas bubbles," *J. Acoust. Soc. Am.* **97**(3), 1510-1521 (1995).
- [7] L. Hoff, P. C. Sontum, and J. M. Hovern "Oscillations of polymeric microbubbles: Effect of the encapsulating shell," *J. Acoust. Soc. Am.* **107**(4), 2272-2280 (2000).
- [8] L. Hoff, *Acoustic Characterization of Contrast Agents for Medical Ultrasound Imaging* (Kluwer, Dordrecht, 2001).
- [9] B. Dollet, S. M. van der Meer, V. Garbin, N. de Jong, D. Lohse and M. Versluis, "Nonspherical oscillations of ultrasound contrast agent microbubbles," *Ultrasound in Med. and Biol.*, **34**(9), 1465-1473 (2008).
- [10] H. Miao, S. M., Gracewski and D. Dalecki, "Ultrasonic excitation of a bubble inside a deformable tube: Implications for ultrasonically induced hemorrhage," *J. Acoust. Soc. Am.* **124**, 2374-2384 (2008).
- [11] S. Qin and K. W. Ferrara, "Acoustic response of compliant microvessels containing ultrasound contrast agents," *Phys. Med. Biol.* **51**, 5065-5088 (2006).
- [12] S. Qin and K. W. Ferrara, "The natural frequency of nonlinear oscillation of ultrasound contrast agents in microvessels," *Ultrasound Med. Biol.* **33**, 1140-1148 (2007).
- [13] S. Martynov, E. Stride and N. Saffari, "The natural frequencies of microbubble oscillation in elastic vessels," *J. Acoust. Soc. Am.* **126**(6), 2963-2972 (2009).
- [14] J. R. Blake, B. B. Taib and G. Doherty, "Transient cavities near boundaries. 1. Rigid boundary," *J. fluid Mech.* **170**, 479-497 (1986).
- [15] J. R. Blake, B. B. Taib and G. Doherty, "Transient cavities near boundaries. 2. Free-surface," *J. fluid Mech.* **181**, 197-212 (1987).
- [16] C. T. Hsiao, X. Lu and G. L. Chahine, "Three-dimensional modelling of the dynamics of therapeutic ultrasound contrast agents," *WIMRC Cavitation Forum*, July 7-9 (2008).
- [17] Q. X. Wang, "The evolution of a gas bubble near an inclined wall," *Theor. Comput. Fluid Dynamics* **12**, 29-51 (1998).
- [18] Q. X. Wang, "Numerical simulation of violent bubble motion," *Phys. Fluids* **16**(5), 1610-1619 (2004).
- [19] M. L. Calvisi, O. Lindau, J. R. Blake and A. J. Szeri, "Shape stability and violent collapse of microbubbles in acoustic traveling waves," *Phys. Fluids* **19**, 047101 (2007).
- [20] A. Z. Zinchenko, M. A. Rother and R. H. Davis, "A novel boundary-integral algorithm for viscous interaction of deformable drops," *Phys. Fluids* **9**(6), 1493-1511 (1997).
- [21] K. Sato, Y. Tomita and A. Shima, "Numerical analysis of a gas bubble near a rigid boundary in an oscillatory pressure field," *J. Acoust. Soc. Am.* **95**(5), 2416-2424 (1994).

Implicit Large Eddy Simulation of Cavitation in Micro Channel Flows

S. Hickel *, M. Mihatsch , S.J. Schmidt

Institute of Aerodynamics and Fluid Mechanics, Technische Universität München
85747 Garching, Germany.

* email: sh@tum.de

ABSTRACT

We present a numerical method for Large Eddy Simulations (LES) of compressible two-phase flows. The method is validated for the flow in a micro channel with a step-like restriction. This setup is representative for typical cavitating multi-phase flows in fuel injectors and follows an experimental study of Iben et al. [1]. While a diesel-like test fuel was used in the experiment, we solve the compressible Navier-Stokes equations with a barotropic equation of state for water and vapor and a simple phase-change model based on equilibrium assumptions. Our LES resolve all wave dynamics in the compressible fluid and the turbulence production in shear layers.

1. INTRODUCTION

Turbulence modeling and the numerical discretization of the Navier-Stokes equations are strongly coupled in Large Eddy Simulations (LES). Since subgrid-scale (SGS) models generally operate on scales that are only marginally resolved by the underlying numerical method, the truncation error of common approximations for the convective terms can out-weigh the effect of even physically sound models. This interference is especially severe in LES of cavitating flows, as numerical errors of robust discretizations increase notably at discontinuities such as phase boundaries and shock waves that are generated by vapor-bubble collapses.

A different approach is to exploit this link by developing discretization methods from subgrid-scale models, or vice versa. Approaches where SGS models and numerical discretizations are fully merged are called implicit LES (ILES). SGS effects are modeled explicitly if the underlying conservation law is modified and subsequently discretized. The filtering concept of Leonard [2] is commonly employed for deriving explicit SGS models without reference to a computational grid and without taking into account a discretization scheme. As implicit modeling we denote the situation when the unmodified conservation law is discretized and the numerical truncation error acts as an SGS model. Since this SGS model is implicitly contained within the discretization scheme, an explicit computation of model terms becomes unnecessary.

Most previous approaches to implicit SGS modeling have relied on the application of pre-existing discretization schemes

to fluid-flow turbulence. Consequently, methods with suitable implicit SGS models have usually been found by trial and error, which has led to the common belief that an implicit subgrid-scale model is merely inferred by the choice of discretization. Comparative studies have shown that stabilizing under-resolved simulations by upwind or non-oscillatory schemes is insufficient for accurately representing SGS turbulence. For example, Honein and Moin [3] found that traditional ILES required differently tuned parameters to predict the correct decay rates of different quantities. Employing implicit LES for prediction requires numerical methods that are specially designed, optimized and validated for the particular differential equation to be solved. A full coupling of the SGS model and the discretization scheme cannot be achieved without incorporating physical reasoning into the design of the implicit SGS model.

Implicit SGS modeling requires procedures for design, analysis, and optimization of nonlinear discretization schemes. We have proposed such a systematic framework that resulted in the adaptive local deconvolution method (ALDM), see Refs. [4,5]. ALDM is a nonlinear finite volume scheme based on a solution adaptive deconvolution operator and a numerical flux function. Free parameters inherent to the discretization allow to control the truncation error and have been calibrated in such a way that the truncation error acts as a physically motivated SGS model. The compressible version of ALDM, see Ref. [5], is asymptotically consistent with incompressible turbulence theory, which is essential for cavitating low Mach number flows. Yet, the numerical discretization is robust enough to survive strong shock waves [6].

In this paper, we present the first implicit LES of a compressible cavitating two-phase flow. The thermodynamic model and the numerical method are derived in Sections 2 and 3, respectively. A validation of the novel method is presented in Section 4. As the test case we chose a micro channel with a step-like restriction, which is representative for typical cavitating-flow situations in fuel injectors. This setup follows closely an experimental study of Iben et al. [1]. While a diesel-like fuel with confidential properties was used in the experiment, we solve the compressible Navier-Stokes equations with a barotropic equation of state for vapor and water and a simple phase-change model.

2. MATHEMATICAL AND PHYSICAL MODEL

2.1 Governing equations

The governing equations in our simulations are the fully compressible three-dimensional Navier-Stokes equations written in integral form

$$\partial_t \bar{U} = \frac{1}{V} \oint_{\partial V} (C(U) + S(U)) \cdot dA \quad (1)$$

with appropriate initial and boundary conditions. The solution vector containing the volume-averaged conserved variables is

$$\bar{U} = \frac{1}{V} \int_V U dV, \quad (2)$$

where the vector $U = [\rho, \rho u_1, \rho u_2, \rho u_3, \rho E]$ represents density, momentum and total energy. The overbar denotes the volume average for an arbitrary control volume V with surface ∂V . Note that we distinguish between the convective flux

$$C_i(U) = [u_i \rho, u_i \rho u_1, u_i \rho u_2, u_i \rho u_3, u_i \rho E] \quad (3)$$

and the flux due to surface stresses

$$S(U) = [0, \delta_{i1} p - \tau_{i1}, \delta_{i2} p - \tau_{i2}, \delta_{i3} p - \tau_{i3}, u_k (\delta_{ik} p - \tau_{ik}) + q_i], \quad (4)$$

where u_i is the velocity vector, τ_{ij} denotes the viscous stress tensor

$$\tau_{ij} = \mu \left(\partial_j u_i + \partial_i u_j - \frac{2}{3} \delta_{ij} \partial_k u_k \right), \quad (5)$$

and the heat flux is

$$q_i = -\kappa \partial_i T. \quad (6)$$

The numerical reconstruction of $C(U)$ and $S(U)$ at the surface ∂V will be discussed in Section 3.

As we consider cavitating flows with phase change, the fluid within the volume V can be in liquid or gaseous state. For later convenience we define the vapor volume fraction

$$\alpha = \frac{V_{vap}}{V}, \quad (7)$$

where V_{vap} denotes the part of the volume V that is occupied by vapor. Analogously, $V_{liq} = V - V_{vap}$ is volume of fluid in liquid state. The Navier-Stokes equations (1) are closed by constitutive relations for the pressure \bar{p} and viscosity $\bar{\mu}$ of the volume-averaged, i.e. homogenized, fluid.

2.2 Thermodynamic model

Our cavitation model is based on a barotropic equation of state for water and water-vapor mixtures, i.e., the pressure and vapor volume fraction are pure functions of the mean density

$$\bar{p} = \alpha \rho_{vap} + (1 - \alpha) \rho_{liq}. \quad (8)$$

Phase change is supposed to be infinitely fast, isentropic and in mechanical equilibrium. The shape of the liquid-vapor interface

is not reconstructed and the effect of surface tension on the vapor pressure is neglected. With these assumptions, the densities of liquid and vapor are $\rho_{liq} = \rho_{sat,liq}$ and $\rho_{vap} = \rho_{sat,vap}$, i.e., we can compute the vapor volume fraction from

$$\alpha = \frac{V_{vap}}{V} = \begin{cases} 0 & , \bar{p} \geq \rho_{sat,liq} \\ \frac{\rho_{sat,liq} - \bar{p}}{\rho_{sat,liq} - \rho_{sat,vap}} & , \bar{p} < \rho_{sat,liq} \end{cases}, \quad (9)$$

where $\rho_{sat,liq}$ and $\rho_{sat,vap}$ are saturation densities of pure water and pure vapor, respectively. Liquid water ($\alpha=0$) is modeled with high accuracy by a modified Tait equation of state

$$\bar{p} = (p_{sat} + B) \cdot \left(\frac{\bar{\rho}}{\rho_{sat,liq}} \right)^N - B, \quad \alpha = 0 \quad (10)$$

where $N = 7.1$ and $B = 3.06 \cdot 10^8$ Pa are fitted constants. Water starts to evaporate if the pressure drops below the saturation pressure p_{sat} . Assuming phase change along an isentropic equilibrium path, we obtain the following equation for the equilibrium speed of sound

$$\frac{1}{\bar{\rho} c_{eq}^2} = \left(\frac{\alpha}{\rho_{vap} c_{p,vap}^2} + \frac{1-\alpha}{\rho_{liq} c_{p,liq}^2} \right) + \left(\frac{1}{\rho_{vap}} + \frac{1}{\rho_{liq}} \right)^2 \frac{T}{L} \left(\alpha \rho_{vap} c_{p,vap} + (1-\alpha) \rho_{liq} c_{p,liq} \right). \quad (11)$$

L is the latent heat at the temperature T and $c_{p,liq}$ and $c_{p,vap}$ are the specific heats at constant pressure of the liquid and of the vapor. As $\rho_{liq} \gg \rho_{vap}$, the equilibrium speed of sound in the two-phase regime, i.e. for $0 < \alpha < 1$, is

$$c_{eq} = \frac{L \rho_{vap}}{\sqrt{c_{p,liq} T}} \frac{1}{\bar{\rho}} + HOT. \quad (12)$$

By integration of the square of Eq. (12) we obtain the equilibrium pressure

$$\bar{p} = p_{sat} + C \left(\frac{1}{\rho_{sat,liq}} - \frac{1}{\bar{\rho}} \right), \quad 0 < \alpha < 1. \quad (13)$$

The parameter C , as well as the pressure and density at the saturation point generally depend on temperature. This temperature dependence is neglected in our isentropic model. For the chosen reference temperature of $T = T_{ref} = 293.15$ K follow $p_{sat} = 2340$ N/m², $\rho_{sat,liq} = 998.1618$ kg/m³, $\rho_{sat,vap} = 0.01731$ kg/m³, and $C = 1468.54$ Pa kg/m³.

The dynamics of wall-bounded flows, such as the flow through micro channels, is strongly influenced by viscous stresses. As the dynamic viscosities of liquid water and vapor differ by several orders of magnitude, the chosen model for the viscosity of the homogenized two-phase fluid is of particular importance. Frequently [7-8, e.g.], a straightforward approach

$$\bar{\mu} = \alpha \mu_{vap} + (1 - \alpha) \mu_{liq} \quad (14)$$

is used, which assumes unlimited deformability. The surface tension at the phase boundaries, however, can increase the

resistance against deformation substantially. Fully immersed small vapor bubbles behave approximately like rigid particles. Einstein [9] found

$$\bar{\mu} = (1 + \frac{5}{2}\alpha)\mu_{liq} \quad (15)$$

for the effective viscosity of a suspension of a large number of small particles in a liquid. We follow Ref. [10] and combine Eq. (14) and Eq. (15) to obtain the final form of the volume averaged viscosity of the cavitating fluid

$$\bar{\mu} = (1 - \alpha)(1 + \frac{5}{2}\alpha)\mu_{liq} + \alpha\mu_{vap} \quad (16)$$

with $\mu_{liq} = 1.002 \cdot 10^{-3} \text{ Pa s}$ and $\mu_{vap} = 9.727 \cdot 10^{-6} \text{ Pa s}$.

3. NUMERICAL METHOD

3.1 Implicit LES

Our flow solver INCA is a finite volume method for LES. Deriving suitable numerical models for LES of compressible flows is particularly challenging because the unresolved subgrid scales in LES represent very different flow phenomena. On one hand, SGS can originate from turbulence. On the other hand, there are unique (resolution invariant) discontinuities, such as shock waves and material interfaces, which are very distinct from the smooth variations produced by turbulence and require different modeling approaches.

For phenomena involving mechanisms that may invalidate underlying assumptions of classical turbulence models, it is necessary to rely on more elaborate approaches such as implicit LES. Implicit LES modeling involves a direct coupling between the numerical scheme and the SGS model. For brevity of notation, the following summary of this concept is given for the 1-D case and a generic non-linear transport equation

$$\partial_t u + \partial_x F(u) = 0 \quad (17)$$

Following Leonard [2] the discretized equation is obtained by convolution with a homogeneous filter kernel G and subsequent discretization

$$\partial_t \bar{u}_N + G * \partial_x F_N(u_N) = -G * \partial_x \tau_{SGS} \quad (18)$$

where the overbar denotes the filtering

$$\bar{u} = G * u \quad (19)$$

and the subscript N indicates grid functions obtained by projecting continuous functions onto the grid $x_N = \{x_j\}$. The subgrid-stress tensor

$$\tau_{SGS} = F(u) - F_N(u_N) \quad (20)$$

originates from the grid projection of non-linear terms and has to be modeled in order to close Eq. (18). With Leonard's approach the filtering of the continuous system is considered as predominant approximation where the numerical error in solving this continuous system is supposed to be negligibly small. Consequently, explicit SGS models are usually derived without

reference to a computational grid and without taking into account any discretization scheme.

The unfiltered, i.e., continuous, solution u is unknown in LES. However, accurate approximations \tilde{u}_N of the discrete grid function u_N can be reconstructed from \bar{u}_N by regularized deconvolution. Hence, the solution obtained with the discrete operators does not satisfy Eq. (18), but rather a modified differential equation

$$\partial_t \bar{u}_N + G * \partial_x F_N(u_N) = \varepsilon_N - \tilde{G} * \tilde{\partial}_x \tilde{\tau}_{SGS} \quad (21)$$

Solved numerically, the discrete approximation of the SGS model interferes with the truncation error of the underlying discretization scheme

$$\varepsilon_N = G * \partial_x F_N(u_N) - \tilde{G} * \tilde{\partial}_x \tilde{F}_N(\tilde{u}_N), \quad (22)$$

where a tilde indicates the respective numerical approximation. This interference of model and discretization is exploited in implicit LES. Particularly, an explicit SGS model is resembled if the filtered divergence of the model SGS tensor is approximated by

$$\varepsilon_N \approx -G * \partial_x \tau_{SGS} \quad (23)$$

so that no model terms have to be computed explicitly during time advancement.

3.2 Adaptive Local Deconvolution Method (ALDM)

With ALDM numerical discretization and SGS modeling are merged entirely. The discrete system for evolving a grid-function approximation is considered directly as a truncated representation of the unmodified continuous system, Eqs. (1) and (17). A suitable environment for the discretization design is provided by a finite-volume method that works directly on the integral form of the Navier-Stokes equations (1). Although filtering is not performed explicitly, we can use the filter formulation of Leonard as an analytical tool when designing and analyzing the discrete operators. A finite-volume discretization corresponds to the evaluation of Eq. (18) with a top-hat filter

$$G(x, V_j) = \begin{cases} 1/V_j & , x \in V_j \\ 0 & , \text{else} \end{cases}, \quad (24)$$

where V_j denotes the cell volume (3-D) or the grid spacing (1-D) of the cell j of the computational grid. Note the equivalence of Eqs. (19) with (24) and Eq. (2).

The numerical building blocks of finite-volume methods are a reconstruction of the unfiltered solution at cell faces, a numerical flux function that works on the reconstructed solution, and a numerical integration scheme to compute the face-averaged flux. The averaging and reconstruction steps involved in finite-volume discretizations are related to the filtering and deconvolution that are well known in explicit SGS modeling. Following the concept of Schumann [11], the subgrid-stress tensor has to account for the limited numerical accuracy of the flux reconstruction. With respect to implicit LES, an advantageous aspect is the fact that the numerical truncation error of the reconstruction readily appears as a divergence of a tensor, as required for physically motivated implicit modeling by Eq. (23).

With ALDM, a local reconstruction of the unfiltered solution is obtained from a solution-adaptive combination

$$\tilde{u}^\mp(x_{j\pm 1/2}) = \sum_{k=1}^K \sum_{r=0}^{k-1} \omega_{kr}^\mp(\gamma_{kr}, \bar{u}_N) \tilde{g}_{kr}^\mp(x_{j\pm 1/2}) \quad (25)$$

of Harten-type deconvolution polynomials

$$\tilde{g}_{kr}^\mp(x_{j\pm 1/2}) = \sum_{l=0}^{k-1} c_{krl}^\mp(x_N) \bar{u}_{j-r+l}, \quad (26)$$

where half-integer indices denote reconstructions at the cell faces. The grid-dependent coefficients c_{krl}^\mp are chosen such that

$$\tilde{g}_{kr}^\mp(x_{j\pm 1/2}) = u(x_{j\pm 1/2}) + O(h^k) \quad (27)$$

on a grid with spacing h . Adaptivity of the deconvolution operator is achieved by dynamically weighing the respective contributions by $\omega_{kr}^\mp(\gamma_{kr}, \bar{u}_N)$, where γ_{kr} are free model parameters. Instead of maximizing the order of accuracy, deconvolution is regularized by limiting the degree k of local approximation polynomials to $k \leq K$ and by permitting all polynomials of degree $l \leq k \leq K=3$ to contribute to the approximately deconvolved solution. The computational cost of a multi-dimensional finite-volume scheme strongly depends on the implementation of the reconstruction step. An efficient method for the 3-D reconstruction scheme of ALDM is given in Ref. [12]. This simplified adaptive local deconvolution (SALD) method reduces the amount of computational operations without affecting the quality of the LES results. The SALD implementation is used for all computations in this paper.

3.3 Mimetic flux function for barotropic fluids

A flux function suitable for implicit LES of cavitating flows has to meet the following requirements:

1. As simple and efficient as possible to facilitate computations.
2. Preservation of symmetries of the Navier-Stokes equations and asymptotic consistency with incompressible turbulence theory for low-Mach-number flows.
3. Robust and able to capture discontinuities, such as phase boundaries and shock waves.

Standard flux functions for inviscid flows, such as the HLL method of Harten, Lax and van Leer [17], e.g., satisfy point 3 by an approximate solution of the Riemann problem $(\tilde{u}^-, \tilde{u}^+)$. Representing a discontinuity, this solution is however inconsistent with low-Mach-number turbulence, c.f. point 2, in which SGS originate from smooth variations. Thus it is not surprising that shock-capturing Euler schemes strongly overestimate the SGS dissipation of shock-free turbulence [18]. In the sense of Kovasznay [19], compressible LES must correctly model vorticity, entropy and acoustic modes, while the first mode alone is sufficient in incompressible LES. It would stand to reason to use a flux function that works on the reconstructed characteristic variables. The required local decomposition in

vorticity, entropy and acoustic modes, however, increases the computational costs by an order of magnitude, c.f. point 1, and can lead to stability problems if the material properties, such as the speed of sound, are discontinuous functions of the conserved variables. Simple flux upwinding is computationally efficient and can provide sufficient dissipation at discontinuities; however, implicit LES requires a Galilean invariant and more elaborate approach with the possibility of controlling the numerical dissipation dynamically.

In the ALDM framework, secondary regularization is provided by a suitable consistent numerical flux function with the general form

$$\tilde{F}_{j\pm 1/2} = F\left(\frac{\tilde{u}_{j\pm 1/2}^+ + \tilde{u}_{j\pm 1/2}^-}{2}\right) - R(\sigma, \tilde{u}_N^\pm, \bar{u}_N). \quad (28)$$

This numerical flux consists of two parts. The first term corresponds to the physical Navier-Stokes flux. For maximum order of consistency it is computed from the mean of both reconstructions of the unfiltered solution at the considered cell face. Note that this results in a skew-symmetric like discretization with favorable aliasing behavior. The difference between both interpolants is exploited in the regularization term

$$R_{j\pm 1/2} = D(\sigma, \tilde{u}_N^\pm, \bar{u}_N) \left(\tilde{u}_{j\pm 1/2}^+ - \tilde{u}_{j\pm 1/2}^- \right) \quad (29)$$

working on the reconstruction error $\tilde{u}_{j\pm 1/2}^+ - \tilde{u}_{j\pm 1/2}^-$. The dissipation matrix D can be any non-negative, shift-invariant functional of \bar{u}_N and \tilde{u}_N , which needs to be defined specifically for the particular differential equation.

The thermodynamic equilibrium model derived in Sec. 2.2 is based on a barotropic equation of state for the homogenized single- and two-phase fluid. In the following, we therefore only consider the mass and momentum flux. The local adaptive reconstruction scheme of ALDM is applied to the primitive variables density, velocity and pressure. Gradients in the stress tensor S are approximated by linear second order schemes.

We observe that the convective flux for a barotropic fluid can be written as

$$C_i(U) = u_i \rho [1, u_1, u_2, u_3] \quad (30)$$

and propose that also the numerical flux should satisfy this property. The numerical approximation of the mass density flux at an arbitrary cell face is

$$\tilde{C}^\rho = \tilde{u}^C \frac{\tilde{\rho}^+ + \tilde{\rho}^-}{2} - D^\rho (\tilde{\rho}^+ - \tilde{\rho}^-). \quad (31)$$

The dissipation matrix D and the transport velocity \tilde{u}^C will be defined later. The mimetic numerical flux for the momentum equations fulfilling property (30) is

$$\tilde{C}^{\rho u} = \tilde{C}^\rho \frac{\tilde{u}^+ + \tilde{u}^-}{2} - D^{\rho u} \frac{\tilde{\rho}^+ + \tilde{\rho}^-}{2} (\tilde{u}^+ - \tilde{u}^-). \quad (32)$$

For defining the transport velocity \tilde{u}^C , we follow the geometric argument of Harten, Lax and van Leer [17] and propose the

following modification of the contact wave speed of the HLL approximate Riemann solver

$$\tilde{u}^C = \frac{\tilde{u}^+ + \tilde{u}^-}{2} - \frac{\tilde{p}^+ - \tilde{p}^-}{\tilde{\rho}^+(S_R - \tilde{u}^+) - \tilde{\rho}^-(S_L - \tilde{u}^-)}, \quad (33)$$

where SR and SL denote conservative estimates of the fastest right and left going wave speeds, which we compute from

$$\begin{aligned} S_R &= \max(\tilde{u}^+, \tilde{u}^-) + c_{liq} \\ S_L &= \min(\tilde{u}^+, \tilde{u}^-) - c_{liq} \end{aligned} \quad (34)$$

In order to ensure asymptotic consistency of the flux with ALDM for incompressible turbulence and passive scalar mixing, Ref. [4,13], in the limit of small Mach numbers $Ma = u/c \rightarrow 0$, we define the dissipation matrix as

$$D_i = \begin{bmatrix} \sigma^\rho |\delta \bar{u}_i| \\ \sigma^{\rho u} |\delta \bar{u}_1| \\ \sigma^{\rho u} |\delta \bar{u}_2| \\ \sigma^{\rho u} |\delta \bar{u}_3| \end{bmatrix}. \quad (35)$$

where σ^ρ and $\sigma^{\rho u}$ are free model parameter and $\delta \bar{u}$ denotes the difference of volume-averaged velocity of the two adjacent cells.

The free parameters $\{\gamma, \sigma\}$ in the solution-adaptive stencil-selection scheme and the numerical flux function can be used to adjust the spatial truncation error of the discretization. For implicit SGS modeling, the values of these free parameters are chosen in such a way that the truncation error ε_N of the discretization method acts as a physically motivated SGS model. We use optimized parameter values that were determined in Refs. [4,13] by minimizing a cost function that measures the difference between the effective spectral numerical viscosity of ALDM and the eddy viscosity from Eddy-Damped Quasi-Normal Markovian (EDQNM) theory for isotropic turbulence. The resulting method represents a full merger of numerical discretization and SGS model. Incorporating the essential elements of LES, filtering and deconvolution, the implicit model of ALDM combines a tensor-dissipation regularization with a generalized scale-similarity approach. Explicit deconvolution-type SGS models have so far been limited to linear deconvolution. ALDM extends, by employing methods that are well established for essentially non-oscillatory finite-volume discretizations, the concept of approximate deconvolution to the solution-adaptive non-linear case. Finally, we note that the solution-adaptive stencil selection and the conservative flux formulation at the core of the present method allow for the capturing of shock waves.

The spectral energy transfer at shock waves differs considerably from the mechanisms in unresolved turbulence. These differences have to be taken into account in the SGS modeling strategy. Unresolved turbulence can be modeled with a numerical viscosity proportional to a velocity gradient and the square of a characteristic length scale. Propagating discontinuities, which represent unique SGS, are usually modeled with a numerical viscosity that is proportional to the

wave propagation speed. In order to capture shock waves with ALDM, we detect discontinuities by the sensor functional

$$f_S = \begin{cases} 1 & , \frac{\text{div}(u)}{\text{div}(u) + \text{rot}(u)} > 0.95 \\ 0 & , \text{else} \end{cases} \quad (36)$$

and locally add a second term to the dissipation matrix

$$D_i = \begin{bmatrix} \sigma^\rho |\delta \bar{u}_i| \\ \sigma^{\rho u} |\delta \bar{u}_1| \\ \sigma^{\rho u} |\delta \bar{u}_2| \\ \sigma^{\rho u} |\delta \bar{u}_3| \end{bmatrix} + f_S \frac{1}{2} \left(|\tilde{u}^C| + |\delta \bar{u}_i| \right) \begin{bmatrix} 1 \\ 1 \\ 1 \\ 1 \end{bmatrix}. \quad (37)$$

Note that consistent behavior in the limit of low Mach numbers is maintained by using $|\tilde{u}^C| + |\delta \bar{u}_i|$ rather than $|\tilde{u}^C| + c$.

3.4 Conservative immersed boundary method

The generation of suitable grids for LES of complex flows can be time-consuming and difficult. Contradictory requirements, such as adequate local resolution and minimum number of grid points, can deteriorate the grid quality and adversely affect accuracy and numerical convergence properties. Cartesian grids facilitate automatic grid generation and adaptive local grid refinement by dyadic sub-partitioning, which can be easily accounted for in implicit SGS modeling. Cartesian grids also imply fewer computational operations per grid point than body-fitted or unstructured grids. On the other hand, geometric boundaries do not necessarily coincide with grid lines, so that boundary conditions have to be applied at the subcell level.

We use a conservative immersed boundary method for representing sharp interfaces between a fluid and a rigid body on Cartesian grids, see Refs. [14,15]. A level-set technique is used for describing the interface geometry. The level-set function is the signed distance between each point in the computational domain and the immersed interface, which is positive within and negative outside of the fluid domain. The zero contour is the interface between the fluid and the obstacle.

The intersection of the obstacle with the Cartesian grid produces a set of cells that are cut by the interface. The underlying finite-volume discretization is modified locally in these cut cells in such a way that it accounts only for the fluidic part of a cell. The viscous stresses at the fluid-solid interface are approximated by linear differencing schemes. The interface pressure can be obtained by solving the one-sided (symmetric) Riemann problem in the interface-normal direction, e.g.

$$p^* = p_L + \rho_L (u_L - S_C)(u_L - S_C), \quad (38)$$

where the contact wave velocity is $S_C = 0$ and the left going characteristic is $S_L = \min(u_L, S_C) - c_{eq}$ for non-moving walls.

Because Eq. (38) is inconsistent in the limit $Ma = u/c \rightarrow 0$, a Neumann boundary condition

$$p^* = p_L \quad (39)$$

is imposed in the well resolved boundary layers of the present LES, where the local Mach number is low in cut cells.

As we operate on fluxes only, this cut-cell finite-volume method maintains accuracy and ensures mass and momentum conservation. Required interface normals, face apertures and fluid-volume fractions of cut cells can be computed efficiently from the level-set function. Discrete conservation and a sharp representation of the fluid-solid interface render our method particularly suitable for LES of turbulent flows.

3.5 Time integration

For time integration, the conditionally stable 3rd order Runge-Kutta method of Gottlieb and Shu [16] is used. This time-discretization scheme is total-variation diminishing (TVD) for $CFL \leq 1$, provided the underlying spatial discretization is TVD, whereas the linear stability bound is larger. We found for ALDM stable time advancement up to the linear bound $CFL=1.7$. As cut cell methods can generate cells with a very small fluid volume fraction, a special treatment of such cells is necessary when excessively small time steps according to the CFL stability criterion are to be avoided. For increasing the computational efficiency, we use a conservative mixing procedure, where the conservatives of small cells are mixed with larger neighbors [14,15]. During our simulations, the time step size is adjusted dynamically according to $CFL=0.5$ based on the full cell size.

4. COMPUTATIONAL SETUP AND RESULTS

4.1 Setup

The new ILES methodology is applied to the compressible turbulent flow in a micro channel with a step-like restriction. This forward-facing step geometry, as shown in Fig. 1, was investigated experimentally by Iben *et al.* [1] and is representative for typical cavitating-flow situations in fuel injectors.

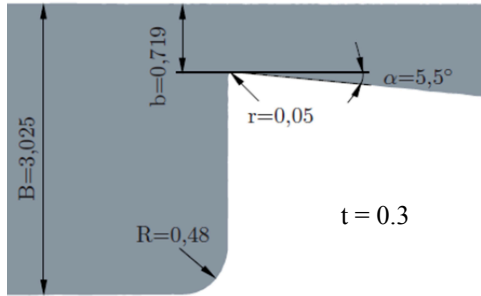


Fig. 1: Geometry of forward facing step flow.

The inlet is located 6 mm upstream of the restriction and has a cross section of $3.0 \times 0.3 \text{ mm}^2$. A laminar channel-flow profile with a bulk velocity of 12 m/s and a mass flow of 10.8 g/s is imposed at the inflow. A static pressure of 50 - 60 bar is imposed at the outlet. The flow is accelerated at the restriction ($0.7 \times 0.3 \text{ mm}^2$) and the pressure drops close to saturation pressure. A shear layer, which is subject to Kelvin-Helmholtz instability, is formed on top of the forward facing step. Cavitation is first observed in the vortex cores of this shear

layer. Fig. 2 shows a snapshot of the instantaneous cavitation distribution in the experiment [1].

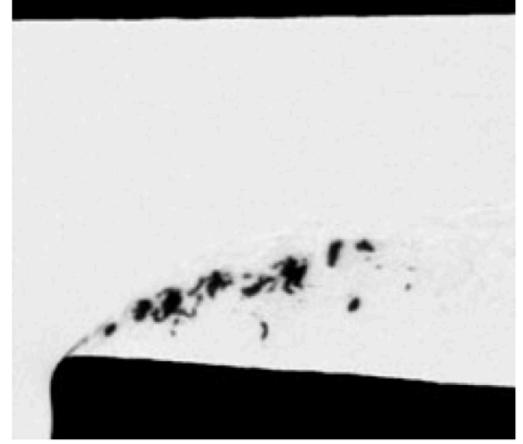


Fig. 2: Instantaneous cavitation distribution in the experiment of Iben *et al.* [1].

The flow geometry is represented by our flow solver INCA through a conservative cut-cell method on an adaptive Cartesian grid. A suitable initial solution for our LES is generated through a grid sequencing technique. That is, we start the simulation on an initially very coarse grid that is gradually refined during the simulation as the solution approaches a developed turbulent state. The final grid is shown in Fig. 3. It consists of 11×10^6 cells and has a resolution of $2 \times 10^{-6} \text{ m}$ in the region of interest. The fine grid resolution and the conditionally stable time integration method imply a time step size of $2.3 \times 10^{-10} \text{ s}$. Several million time steps were required to resolve the integral time scales of the flow. The present LES was only feasible because the grid is rapidly coarsened towards the inflow and outflow. Fig. 3 shows also a large reservoir that is attached at the right side in order to reduce reflections of acoustic waves at the fixed-pressure outflow boundary condition.

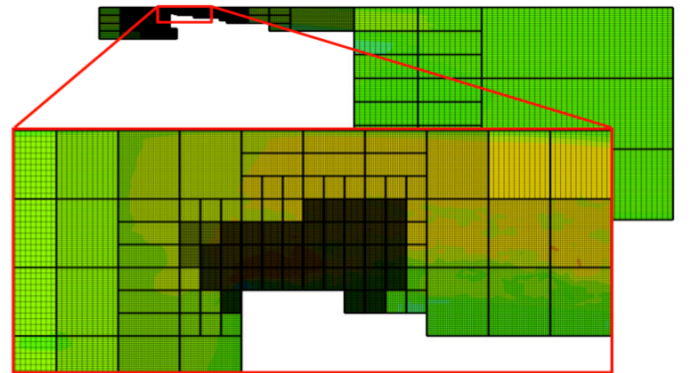


Fig. 3: Adaptive Cartesian computational grid. The channel geometry, which is represented by a conservative cut-cell method with sub-cell accuracy, is not shown.

4.2 Results

The initial data for a developed turbulent flow was generated with an outlet pressure of $p_{out}=60$ bar. The backpressure is then gradually reduced to 57, 54, and 50 bar. Fig 4 shows the evolution of the mean vapor volume fraction (based on the volume of the entire computational domain). Cavitation is first observed in the vortex cores of the shear layer for $p_{out}=57$ bar. Reduced outlet pressures of $p_{out}=54$ bar and eventually $p_{out}=50$ bar lead to a higher cavitation probability, as can be seen in the insert of Fig. 4.

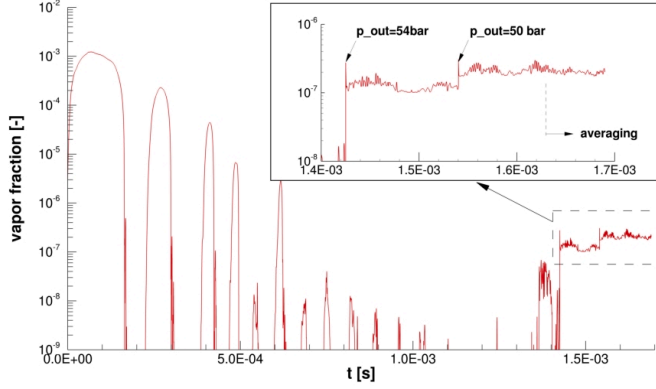


Fig. 4: Evolution of the mean vapor volume fraction.

We visualize the vapor regions and corresponding coherent turbulence structures at the onset of cavitation ($p_{out}=57$ bar) in Fig. 5. We observe large incoming corner vortices, which lead to flow separation in the corners between the channel sidewalls and the restriction. The displacement by these separation bubbles results in further acceleration of the bulk flow. The flow separation renders the flow 3-D. 2-D Kelvin-Helmholtz rollers are not visible in contour plots of the λ_2 vortex-identification criterion; rather hairpin vortices are observed in the unstable shear layer. Vapor regions are clearly correlated with the cores of these vortices. This finding is consistent with the experimental observations, c.f. Fig. 2.

Figures 6 and 7 show instantaneous velocity, density and pressure fields in the center plane above the restriction for $p_{out}=50$ bar. We clearly see the shear layer and corresponding turbulent structures. A statistical analysis has been conducted for the final backpressure level of 50 bar. 70.000 statistical samples (gathered every 10 time steps) are averaged in time and in the spanwise direction. The spanwise averaging improves convergence and comparability with the experiment, where possible observations through side windows represent spanwise optical averages. The mean velocity and mean void fraction is shown in Fig. 8, Reynolds stresses are shown in Fig. 9.

The mean vapor fraction, lower part of Fig. 8, is in reasonable agreement with experimental data in Fig. 5 of Ref. [1]. We cannot expect perfect agreement, because our LES were performed with the material properties of water, whereas a diesel-like fuel with confidential properties was used in the experiment. The values of our inlet mass flux and outlet pressure therefore constitute an educated guess rather than exact data. We

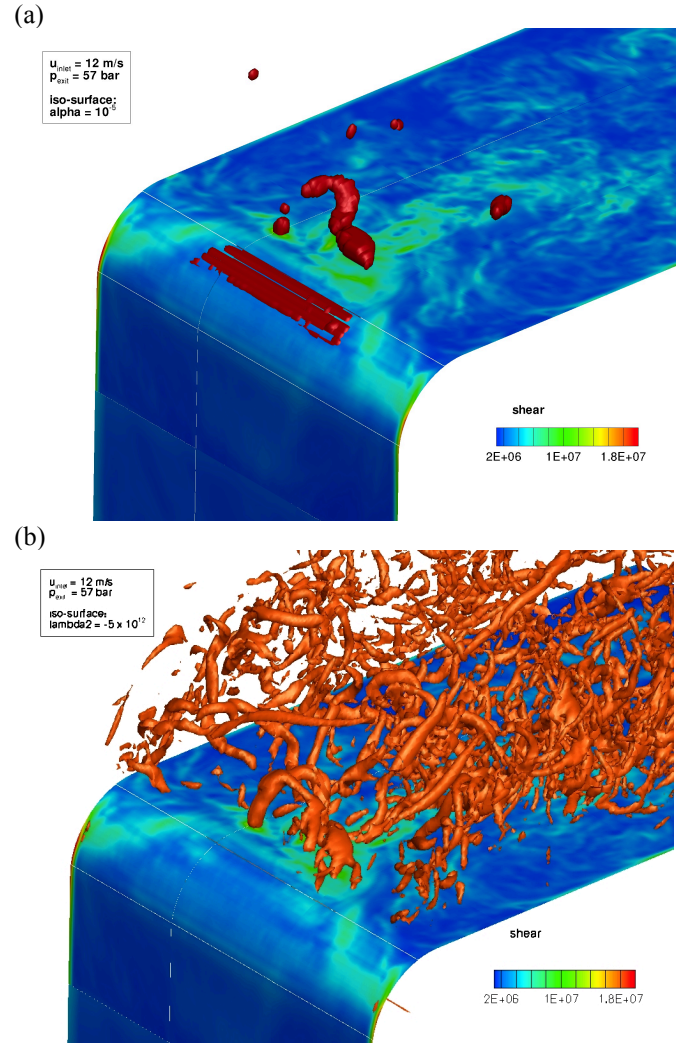


Fig. 5: LES of cavitating forward-facing step flow in a micro channel. (a) Shear stress at the wall and iso-surface of the vapor volume fraction visualizing cavitation. (b) Coherent turbulence structures visualized by the λ_2 criterion.

should notice, however, that the onset of cavitation appears to happen slightly too early, which can be attributed to the thermodynamic equilibrium model. We also notice that the grid coarsening in our LES imposes a fixed bound for the location of the rear end of the cavitating two-phase region, see e.g. the lower part of Fig. 7. A simulation with an extended fine-grid zone is therefore planned for the future.

5. CONCLUSIONS

We have presented a numerical method for implicit LES of compressible two-phase flows. The novel method is applied and validated for the flow in a micro channel with a step-like restriction. Our LES resolve all wave dynamics in the compressible fluid and the turbulence production in shear layers. The numerical results are in good agreement with available experimental data. This work represents, to our knowledge, the first successful LES of a cavitating two-phase flow with a compressible fluid model.

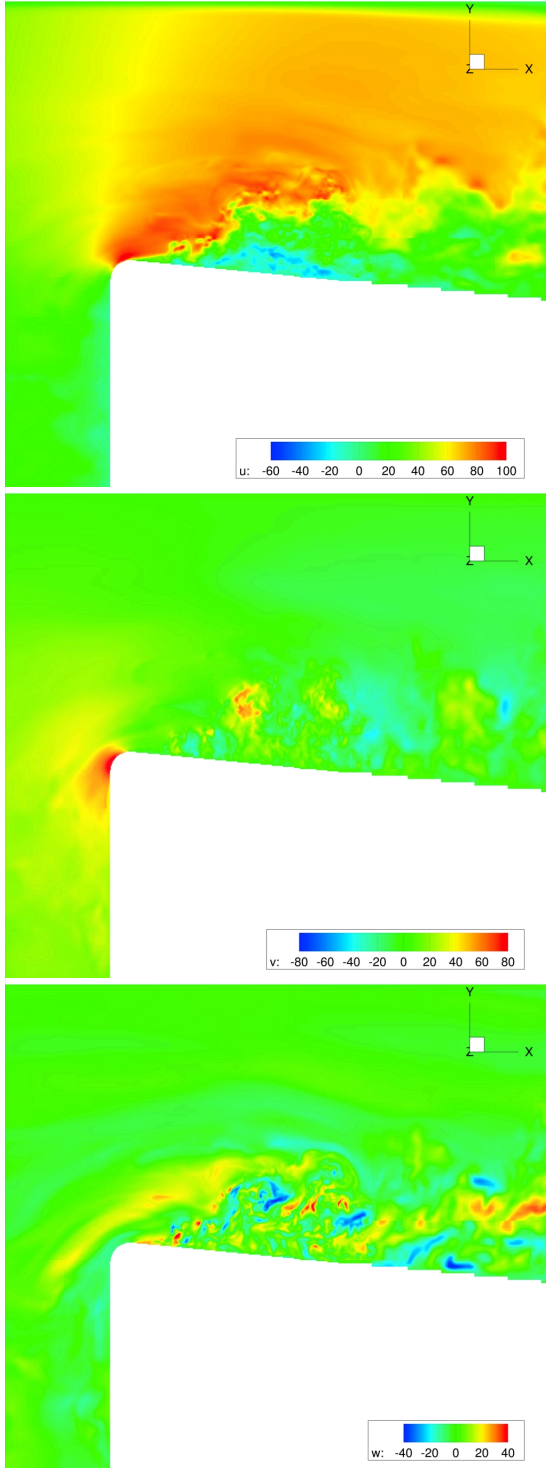


Fig. 6: Instantaneous velocity field in the center plane for LES of cavitating forward-facing step flow in a micro channel.

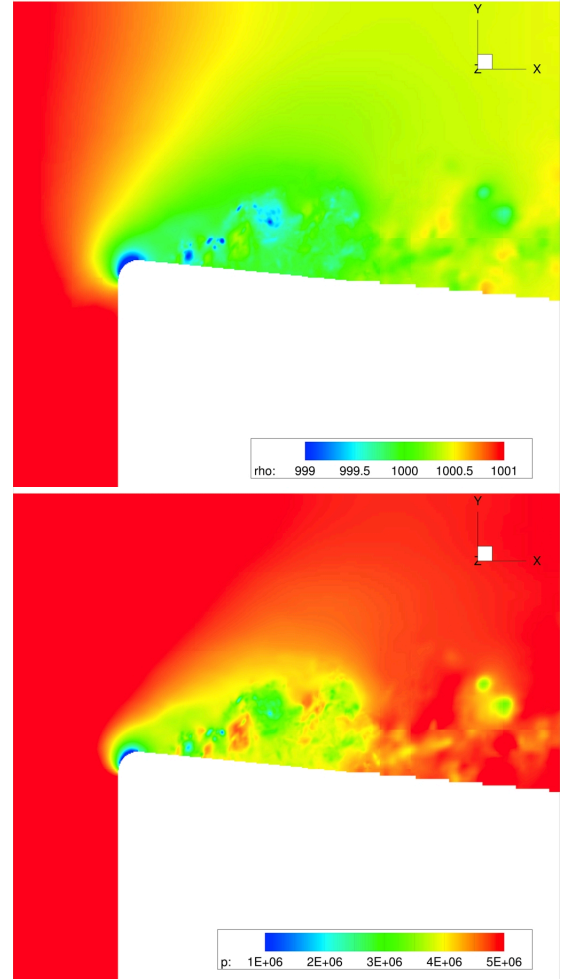


Fig. 7: Instantaneous density and pressure field in the center plane for LES of cavitating forward-facing step flow in a micro channel.

ACKNOWLEDGMENTS

We would like to thank Christian Egerer for visualizing the computational results. Simulations were performed at the Leibniz-Rechenzentrum München (LRZ).

REFERENCES

- [1] U. Iben, A. Morozov, E. Winklhofer, F. Wolf (2010) Laser-pulse interferometry applied to high-pressure fluid flow in micro channels. *Exp. Fluids*, DOI 10.1007/s00348-010-0950-9.
- [2] A. Leonard (1974) Energy cascade in large eddy simulations of turbulent fluid flows. *Adv. Geophys.* 18A, 237–248.

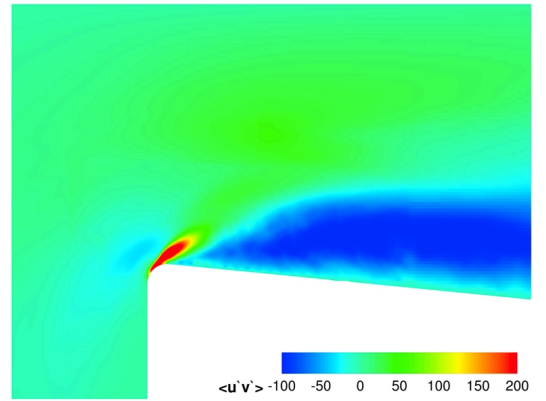
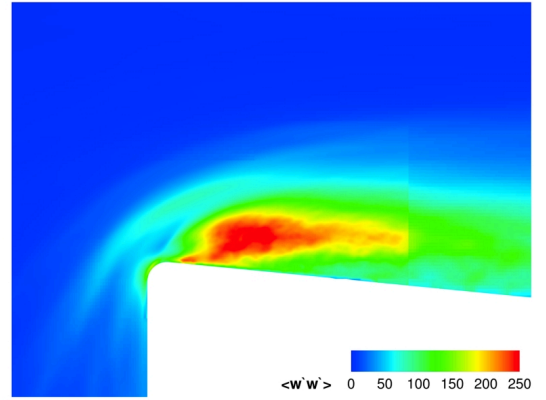
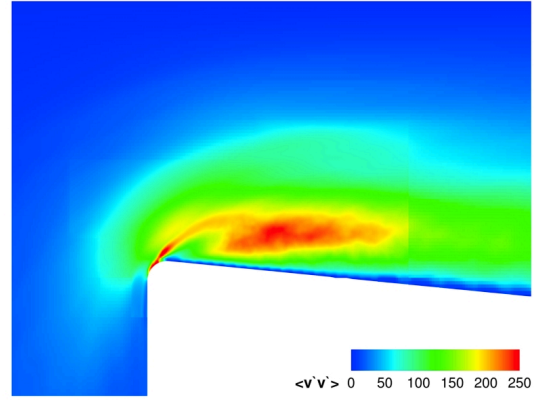
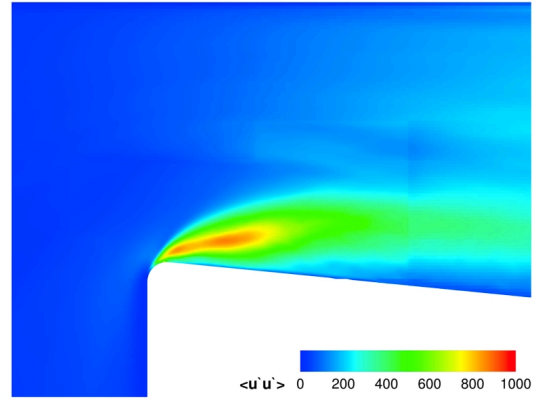
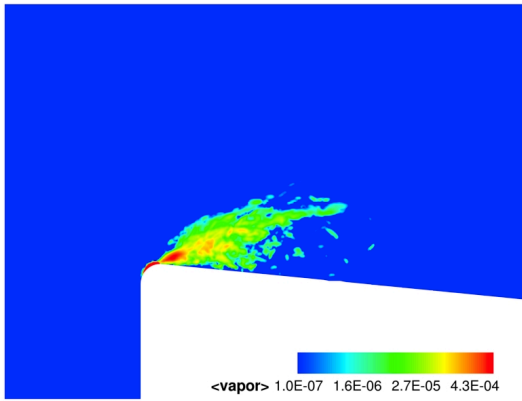
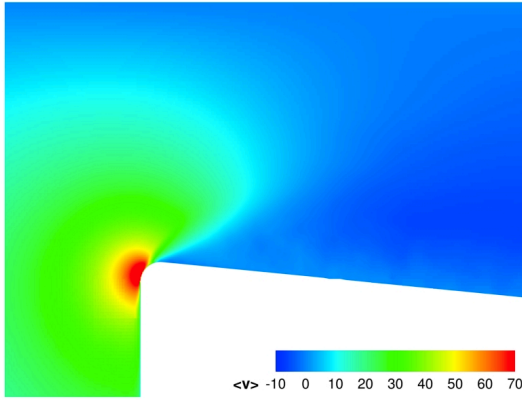
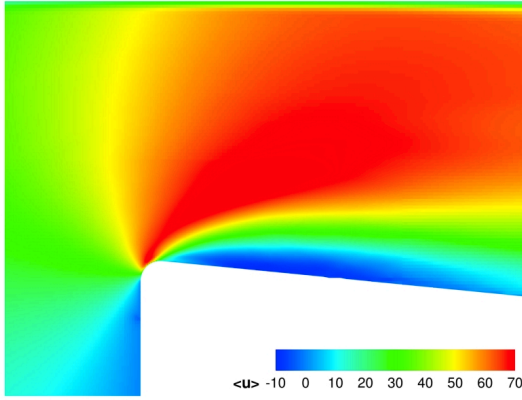
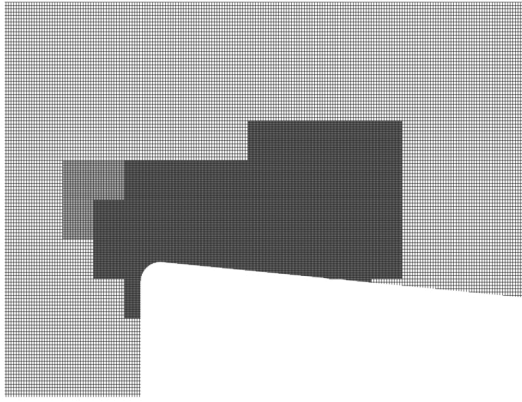


Fig. 8: Adaptive Cartesian computational grid in the interrogation region, mean velocity field and mean vapor volume fraction.

Fig. 9: Reynolds stresses.

- [3] A.E. Honein and P. Moin (2005) Numerical aspects of compressible turbulence simulations. Report TF-92, Department of Mechanical Engineering, Stanford University.
- [4] S. Hickel, N. A. Adams, and J. A. Domaradzki (2006) An adaptive local deconvolution method for implicit LES. *J. Comp. Phys.*, 213:413–436.
- [5] S. Hickel and J. Larsson (2008) An adaptive local deconvolution model for compressible turbulence. In *Proceedings of the 2008 Summer Program*, pages 85–96. Center for Turbulence Research, Stanford University.
- [6] O.C. Pettrache, S. Hickel, N.A. Adams (2011) Large Eddy Simulation of turbulence enhancement due to forced shock motion in shock boundary layer interaction. *AIAA paper 2011-2216*; 17th AIAA International Space Planes and Hypersonic Systems and Technology Conference; San Francisco, California, USA.
- [7] R.E. Bensow, G. Bark (2010) Implicit les predictions of the cavitating flow on a propeller. *Journal of Fluids Engineering*, 132.
- [8] W. Yuan, J. Sauer, G.H. Schnerr (2001) Modeling and computation of unsteady cavitation flows in injection nozzles. *Editions scientifiques et medicales Elsevier SAS.*, 2:383 – 394.
- [9] A. Einstein (1906) Eine neue Bestimmung der Molekül-dimensionen. Section 2: Berechnung des Reibungskoeffizienten einer Flüssigkeit, in welcher sehr viele kleine Kugeln in regelloser Verteilung suspendiert sind. *Ann. d. Phys.* IV, 297-306.
- [10] D. Beattie, P. Whalley (1962) A simple two-phase frictional pressure drop calculation method. *Int. Journal of Multiphase Flow*, 8:83–87.
- [11] U. Schumann (1975) Subgrid scale model for finite-difference simulations of turbulence in plane channels and annuli. *J. Comp. Phys.* 18, 376–404.
- [12] S. Hickel and N.A. Adams (2006). Efficient implementation of nonlinear deconvolution methods for implicit large-eddy simulation. In W. Nagel, W. Jäger, and M. Resch (Eds.), *High Performance Computing in Science and Engineering. Transactions of the High Performance Computing Center, Stuttgart (HLRS)*, pp. 293–306. Springer.
- [13] S. Hickel, N.A. Adams, and N.N. Mansour (2007) Implicit subgrid-scale modeling for large-eddy simulation of passive- scalar mixing. *Phys. Fluids* 19, 095102.
- [14] M. Meyer, A. Devesa, S. Hickel, X.Y. Hu, N.A. Adams (2010) A conservative immersed interface method for large-eddy simulation of incompressible flows. *Journal of Computational Physics* 229: 6300-6317.
- [15] M. Grilli, S. Hickel, X.Y. Hu, N.A. Adams (2009) Conservative immersed boundary method for compressible flows. *Academy Colloquium on Immersed boundary methods: current status and future research directions*, Amsterdam, The Netherlands.
- [16] S. Gottlieb, C.-W. Shu (1998) Total variation diminishing Runge-Kutta schemes. *Math. Comput.* 67, 73–85.
- [17] A. Harten, P.D. Lax, and B. van Leer (1983) On Upstream Differencing and Godunov-type Schemes for Hyperbolic Conservation Laws. *SIAM Review* 25 (1):35–61.
- [18] E. Garnier, M. Mossi, P. Sagaut, P. Comte, M. Deville (1999) On the use of shock-capturing schemes for large-eddy simulation. *J. Comput. Phys.* 153, 273–311.
- [19] L.S.G. Kovaszny (1953). Turbulence in supersonic flow. *J. Aero. Sci.* 20(10), 657–674. Reprinted in *AIAA J.* 41 (7), 2003.